Schriftenreihe des
Instituts für Mikrowellentechnik



23

David Werbunat

Coherent Networks of Uncoupled Digital Radars

Institut für Mikrowellentechnik
Universität Ulm

Coherent Networks of Uncoupled Digital Radars



universität ulm

Coherent Networks of Uncoupled Digital Radars

DISSERTATION

zur Erlangung des akademischen Grades eines

DOKTOR-INGENIEURS (Dr.-Ing.)

der Fakultät für Ingenieurwissenschaften,
Informatik und Psychologie der Universität Ulm

von

David Werbunat

aus Aachen

Gutachter:	Prof. Dr.-Ing. Christian Waldschmidt
	Prof. Dr.-Ing. Martin Vossiek
Amtierende Dekanin:	Prof. Dr. Anke Huckauf

Ulm, 16. Dezember 2024

Bibliografische Information der Deutschen Nationalbibliothek
Die Deutsche Nationalbibliothek verzeichnet diese Publikation in der Deutschen Nationalbibliografie; detaillierte bibliografische Daten sind im Internet über http://dnb.dnb.de abrufbar.

Dissertation, Universität Ulm,
Fakultät für Ingenieurwissenschaften, Informatik und Psychologie, 2024

Impressum
Universität Ulm
Institut für Mikrowellentechnik
Prof. Dr.-Ing. Christian Waldschmidt
Albert-Einstein-Allee 41
89081 Ulm
https://www.uni-ulm.de/mwt

Eine Übersicht über alle Bände der Schriftenreihe finden Sie unter
https://www.uni-ulm.de/mwtschriften

Diese Veröffentlichung ist im Internet auf dem institutionellen Repositorium der Universität Ulm (https://oparu.uni-ulm.de) verfügbar und dort unter der Lizenz CC BY-NC-ND 4.0 publiziert.



Details zur Lizenz finden Sie unter
https://creativecommons.org/licenses/by-nc-nd/4.0/

ISBN 978-3-948303-52-5 ISBN 978-3-948303-53-2 (E-Book)

Vorwort

„Es gibt zwei Arten, sein Leben zu leben: entweder so, als wäre nichts ein Wunder, oder so, als wäre alles ein Wunder."

(Albert Einstein)

Das Zitat von Einstein ist für mich aus zwei Gründen bedeutsam: Zum einen, weil die Wissenschaft für mich dem systematischen Entdecken und Begreifen der Wunder dieser Welt dient. Zum anderen, weil im Oktober 2024 mein Sohn Leo geboren wurde, mit dem ich nun all die Wunder dieser Welt neu entdecken darf. Ihm möchte ich diese Dissertation widmen. An dieser Stelle möchte ich mich ganz besonders bei meiner Frau Nora bedanken, die mich während der gesamten Promotionszeit – insbesondere auch in den letzten Monaten des Schreibens, als sie selbst hochschwanger war – unglaublich unterstützt hat. Ihre Unterstützung hat großen Anteil am Gelingen dieser Arbeit. Meiner gesamten Familie, insbesondere meinen Eltern, danke ich von ganzem Herzen für die vielfältige Unterstützung während des Studiums und der Promotion.

Mein ganz besonderer Dank gilt meinem Doktorvater Prof. Dr.-Ing. Christian Waldschmidt für die hervorragende Betreuung, die fachlichen Anregungen und die spannenden Diskussionen. Ebenfalls bedanke ich mich bei Prof. Dr.-Ing. Martin Vossiek für die Übernahme des Zweitgutachtens. Dem gesamten Institut für Mikrowellentechnik danke ich für die tolle Arbeitsatmosphäre, die gegenseitige Unterstützung und den fachlichen Austausch. Es war (und ist) mir eine Freude, mit Euch zusammenzuarbeiten! Besonders hervorheben möchte ich Christina Bonfert, Benedikt Schweizer und Benedikt Woischneck, die mich bereits als Betreuer meiner Abschlussarbeiten unterstützt haben und, zusammen mit den tollen Vorlesungen von Prof. Waldschmidt, meine Begeisterung für die Radartechnik geweckt haben. Ebenso bedanke ich mich bei meinen Projektpartnern für die tolle Zusammenarbeit, sowie bei allen Abschlussarbeitern und HiWis für die hochmotivierte und engagierte Unterstützung meiner Forschung.

Elchingen, im Dezember 2024

Abstract

In a radar network, multiple radars operate cooperatively, enabling simultaneous sensing from multiple perspectives. This collaboration is particularly valuable when the radars are coherent—enabling bistatic signal processing, where one radar evaluates the signal from one or multiple others, without being affected by synchronization errors. Coherent radar networks leverage the bistatic signal not only for the measurement of bistatic target backscatter, but also for applications such as bistatic SAR imaging for remote sensing and network-based DoA estimation, i.e., the estimation of a targets angle. The latter takes advantage of the extended aperture of the radar network and is particularly promising for automotive applications, where single MIMO radars face constraints due to limited space for vehicle integration. The greatest flexibility is provided by uncoupled coherent radar networks, which do not rely on reference signals distributed via cables. Nonetheless, these networks are also the most challenging to synchronize. Digital radars, however, offer promising opportunities for new synchronization and multiplexing techniques by exploiting their highly flexible digital baseband signal generation and processing capabilities, overcoming signal processing limitations of conventional analog radars.

This thesis presents a comprehensive investigation into the potential of digital radars to overcome the key challenges of uncoupled coherent radar networks. Specifically, these are synchronization and multiplexing. To this end, three different radar network concepts are proposed, verified, and evaluated, leveraging different characteristics of the respective signal modulation. These include the use of single-carrier signals as employed by phase-modulated continous wave (PMCW) radars and multi-carrier signals as used by orthogonal frequency-division multiplexing (OFDM) radars.

First, a novel concept for synchronizing uncoupled PMCW radars using only Rx-side digital signal processing is presented, leading to a radar network called CRNW. By incorporating a timing recovery and a carrier recovery, carrier and sample frequency offsets, as well as phase offsets and phase noise

are corrected. Evaluating a bistatic signal, the timing recovery estimates the sample frequency of the transmitting radar to enable correct resampling, while the carrier recovery facilitates coherent intradyne downconversion using the recovered IF carrier. Measurements demonstrate the high performance of the presented synchronization techniques.

In the second radar network concept, called SymNW, coherency is maintained by avoiding downconversion from RF at another sensor node entirely. Instead, a MIMO OFDM radar is accompanied by several repeater elements, each of which receives the radar Tx signal via reflections at the targets. The repeaters shift the frequency of their received signal in the kHz-range, amplify it, and retransmit it. After a second reflection at the target, this bistatic signal is received by all radar Rx channels. The frequency shift integrates seamlessly in the OFDM multicarrier signal, allowing the signal to be shifted to a set of subcarriers unassigned by the radar. In the virtual array of the network, each repeater contributes a subarray corresponding to a repetition of the radar's virtual array, allowing for network-based DoA estimation as verified by measurements.

The third concept called TriNW also uses repeaters, but fed via a line-of-sight (LoS) path, avoiding additional signal attenuation and ghost targets caused by a double reflection at the targets. By using multi-channel repeater (MCR)—repeaters which split up their Rx signal to multiple repeater Tx channels, each applying a distinct frequency shift—this network allows for a highly flexible virtual network-array (VNA). Consequently, it demonstrates outstanding performance in network-based DoA estimation.

All three radar network concepts are thoroughly compared based on the criteria of dynamic performance, ghost targets, flexibility of VNA design, and DoA estimation performance. Since the TriNW, in addition to its outstanding DoA estimation capabilities, provides dynamic performance comparable to that of a monostatic radar, it is found to be the most suitable for automotive radar imaging. The excellent radar imaging capabilities of the TriNW are further demonstrated in measurements of automotive scenarios including multiple road users such as a car, a pedestrian, a motorcycle, and a bicycle. Using the radar network, all are detected with a high number of features, including details such as the bicycle fork and the cyclist's leg. The suitability of the TriNW as an automotive imaging radar is further emphasized by its ability to detect weak targets such as a pedestrian and cyclist next to strongly reflecting vehicles.

Contents

1 Introduction **1**

2 Digital Radars **5**
2.1 Signal Model 5
2.1.1 Transmit Signal 6
2.1.2 Receive Signal 7
2.2 PMCW Radars 9
2.2.1 PMCW Baseband Signal 10
2.2.2 Range & Doppler Evaluation 11
2.3 OFDM Radars 13
2.3.1 OFDM Baseband Signal 14
2.3.2 Range & Doppler Evaluation 15
2.4 Parameterization 17
2.4.1 Resolution & Unambiguous Region 18
2.4.2 Multiplexing Strategies 18
2.5 MIMO Radar Processing 20
2.5.1 Steering Vector 20
2.5.2 Virtual Array 23
2.5.3 DoA estimation 23

3 Radar Networks – Overview and Classification **25**
3.1 Coupled & Uncoupled Radar Networks 26
3.1.1 Radio-Frequency Coupled Radar Networks 27
3.1.2 Low-Frequency Coupled Radar Networks 27
3.1.3 Uncoupled Radar Networks 27
3.2 Coherent & Incoherent Radar Networks 28
3.3 Uncoupled Coherent Radar Networks 30

4 Concept I – Synchronization of Uncoupled PMCW Radars 33
4.1 System and Measurement Setup . . . 34
4.2 Analysis of Incoherency Impacts . . . 37
4.2.1 Impact of Carrier Frequency Offsets . . . 37
4.2.2 Impact of Phase Noise . . . 37
4.2.3 Impact of the Sample Frequency Offset . . . 40
4.3 Timing Recovery . . . 44
4.4 Carrier Recovery . . . 46
4.4.1 Squaring Loop Carrier Recovery for PMCW Radars . . . 46
4.4.2 Carrier Recovery Performance . . . 50
4.5 Measurements . . . 55
4.5.1 Carrier Recovery . . . 55
4.5.2 Full Synchronization . . . 57
4.6 Discussion . . . 60

5 Concept II – OFDM Radar Network Using Symmetrical Path Repeater 61
5.1 System and Measurement Setup . . . 62
5.2 Signal Model . . . 63
5.2.1 Repeater Receive and Transmit Signal . . . 63
5.2.2 Bistatic Receive Signal . . . 65
5.3 Bistatic Signal Processing . . . 66
5.3.1 Demodulation . . . 66
5.3.2 Cyclic Prefix Compensation & Velocity Estimation . . . 68
5.3.3 Range Estimation . . . 68
5.3.4 Interpretation of the Bistatic Range-Doppler Matrix . . . 69
5.4 Multiplexing . . . 72
5.4.1 Performance Comparison . . . 74
5.5 DoA Estimation . . . 76
5.5.1 Modulation Phase Recovery . . . 76
5.5.2 Virtual Network Array . . . 79
5.5.3 Compressed-Sensing-based DoA Estimation . . . 82
5.6 Measurements . . . 82
5.6.1 Radar Network Setup . . . 83
5.6.2 Single-Target Scenario . . . 85
5.6.3 Multi-Target Scenario . . . 86

5.6.4 Multi-Target Propagation in the DoA Estimation 88
5.7 Discussion 90

6 Concept III – OFDM Radar Network Using Triangular Path MCR 91
6.1 System and Measurement Setup 92
6.2 Signal Model 93
6.2.1 Bistatic Receive Signal 95
6.3 Bistatic Signal Processing 96
6.4 Multiplexing 97
6.5 DoA Estimation 98
6.5.1 Modulation Phase Recovery 98
6.5.2 Virtual Network Array 99
6.5.3 Compressed Sensing-based DoA Estimation 101
6.6 Measurements 102
6.6.1 Radar Network Setup 102
6.6.2 Single-Target Scenario 104
6.6.3 Multi-Target Scenario 104
6.6.4 Input Feedthrough 107
6.7 Discussion 108

7 Assessment of Digital Radar Networks as Imaging Radar 109
7.1 Comparison of Digital Radar Networks 109
7.1.1 Dynamic Performance 110
7.1.2 Ghost Targets 114
7.1.3 Array Design 119
7.1.4 DoA Estimation Performance 122
7.1.5 Conclusion 124
7.2 Digital Radar Network as Automotive Imaging Radar 124
7.2.1 Target Feature Detection 125
7.2.2 Differentiation between Road Users 127

8 Conclusion 129

A Notation 133
A.1 Matrices, Vectors, and Signals 133
A.2 Operators and Functions 133

B Algorithms for Single-Target Peak Classification **135**
B.1 Reference Peak 135
B.2 Bistatic Peak Classification 137

C Array Design Influence on Angular Spectrum **139**

List of Symbols and Acronyms **141**
Symbols 141
Acronyms 144

Bibliography **147**

1 Introduction

Automotive sensing applications have driven civil research on radar technology and their associated signal processing for decades. From an expensive sensor used in military, aeronautical, and naval applications, radar evolved into a mass-market product that is utilized in the majority of modern cars [1], [2]. With its arrival in mass production, research on conventional automotive radar using frequency modulated continuous-wave (FMCW) signals in the 77-GHz frequency band has slowed down. This is despite the continued demand for enhanced sensing capabilities driven by the ongoing strive for autonomous driving. In the last decade, research has consequently concentrated on new concepts to overcome the limitations of conventional automotive radars. The focus is on three major research directions: Radar imaging, radar networks, and digital radars.

The commercial availability of 77-GHz radar frontend MMICs led to a significant increase in the number of transmit (Tx) and receive (Rx) channels. Thus, radars with hundreds [3]–[5] or even more than one thousand [6] virtual channels have been proposed. Their aperture size enables a high-resolution direction of arrival (DoA) estimation, facilitating excellent **radar imaging** capabilities. In particular, imaging radars are able to provide image-like measurement results of its surroundings. By resolving the various reflection points of other road users in great detail, they improve target classification [7].

While technological constraints limiting the number of Tx and Rx channels have been mostly overcome, the lack of available space and integration options in vehicles still constrains the size of automotive radars [5]. **Radar networks** aim to circumvent these restrictions by combining multiple dedicated radars working cooperatively. The concept of a basic radar network is shown in Fig. 1.1. This includes the bistatic signals where one radar evaluates the signal transmitted by another. When multiple radar sensors are combined in a way that allows bistatic signal processing, the radar network is able to provide a combined virtual aperture [8]–[10]. This results in a large aperture while still maintaining

relatively small individual radar sensors, eventually facilitating imaging capabilities [11]. Thus, radar networks have the potential to become an alternative to the aforementioned increase in virtual channels of a single radar.

The third major research direction is **digital radar**, characterized by its digital signal generation and signal processing [12], [13]. Typical digital modulation techniques rely on either single-carrier signals or multi-carrier signals. Both are used by digital radars, the former by phase-modulated continous wave (PMCW) radars [14]–[16], the latter by orthogonal frequency-division multiplexing (OFDM) radars [17], [18]. Research on digital radars is further driven by their high degree of flexibility in signal design and processing. In particular, their Tx and Rx signals are sampled with their entire baseband bandwidth, typically equivalent to the radio frequency (RF) bandwidth. Consequently, information present in the signal at RF is still available to digital signal processing. This paves the way for new approaches to interference mitigation [19]–[22], joint communication and sensing [23]–[26], and the correction of hardware impairments [27]. Moreover, digital radars facilitate a variety of multiplexing schemes beyond the conventional time-division multiplexing (TDM), such as frequency-division multiplexing (FDM) [28], code-division multiplexing (CDM) [29]–[31], and combinations thereof [32]. Since digital radars offer a whole new set of signal processing capabilities, the following question arises:

Does the flexible signal design and processing of digital radars offer new ways to achieve coherency and signal separability in an uncoupled radar network?
In the context of radar networks, the greatest benefit is provided by an uncoupled radar network, wherein no clock signal is distributed via cables. This reduces cost

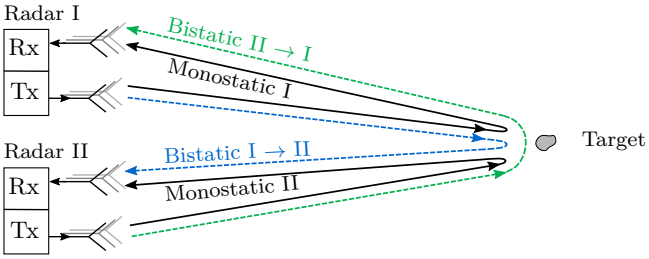

Fig. 1.1: Concept of a radar network, exemplary for two MIMO radars.

and increases flexibility compared to coupled networks. However, it also raises challenges: Bistatic signal evaluation and network-based DoA estimation in an uncoupled radar network requires a coherent signal processing. This implies that incoherency-induced errors, such as frequency offsets, phase offsets, and phase noise, which affect bistatic signal evaluation, must either be accounted for in the radar network design or mitigated by means of signal processing. Furthermore, the separability of the various monostatic and bistatic signals is key for further processing steps like a network based DoA estimation.

Digital radars now provide novel techniques to address these challenges: First, digital radars, especially when using multi-carrier signals, offer far more possibilities for proper multiplexing strategies. Second, digitizing the downconverted baseband signal with its full bandwidth significantly increases the available information. Exploiting this may also lead to new possibilities for radar network synchronization—here, digital radars using single carrier signals are particularly promising, since the information is available without previous demodulation.

This thesis extends the state of the art by proposing novel concepts for the design of digital radar networks and by offering a comprehensive analysis and assessment of their benefits. In particular, it sets out to achieve the following key objectives:

1. Propose new concepts of uncoupled radar networks that exploit the potential of digital radars to achieve signal coherency and signal separability. In order to gain a comprehensive insight, at least one concept using a single-carrier signal, and one concept using a multi-carrier signal are to be proposed.

2. Present a detailed comparison of the proposed network concepts focused on, but not limited to, radar imaging. This way, the digital radar network most suitable for automotive radar imaging has to be selected.

3. Prove the potential of radar networks by presenting automotive imaging measurements. The selected radar network will be put through its paces in a comprehensive measurement campaign. Two key capabilities are to be verified and evaluated in practical scenarios: providing a detailed image of traffic participants and detecting vulnerable road users such as pedestrians next to strongly reflecting vehicles.

Chapter 2 of this thesis provides a more detailed account of digital radars. Initially, it presents a signal model applicable to both PMCW and OFDM radars, followed by a comprehensive introduction to the signal processing techniques applied for each. Then, an overview of the different types of radar networks is presented in **Chapter 3**.

Chapter 4 to 6 propose three different concepts for a digital radar network. In **Chapter 4**, a concept based on PMCW-radars is presented that essentially comprises multiple uncoupled radar sensors. Without hardware-level synchronization, the bistatic signal processing is affected by frequency offsets, phase offsets, and uncorrelated phase noise. To address these errors, a series of signal processing techniques are proposed, including a timing recovery and a carrier recovery. The concept presented in **Chapter 5** takes a different approach: By combining an OFDM radar with multiple repeaters, an uncoupled radar network is designed which inherently retains coherency – without any connection between the radar and the repeaters. To achieve separable monostatic and bistatic signals, each repeater incorporates a distinct frequency shift, which synergizes particularly well with the multicarrier signal of OFDM radars. The concept proposed in **Chapter 6** introduces a novel kind of repeater. It receives the radar signal via a line-of-sight (LoS) path, and then distributes it to four Tx channels, each applying a distinct frequency shift for target separability. This concept thus promises to combine a bistatic signal Rx power comparable to the monostatic one, and a highly flexible placement of the network nodes and their antennas. In **Chapter 7**, a comprehensive assessment of the proposed radar networks is provided, laying the foundation for the selection of a digital radar network for automotive radar imaging. Subsequently, the selected radar network is employed in an extensive measurement campaign that encompasses a variety of measurement scenarios including multiple road users. Finally, the results of this thesis are summarized in **Chapter 8**.

2 Digital Radars

Driven by recent developments in the design of RF-system-on-chip (SoC) [33], [34], the research interest in digital radars has increased significantly in the last years. Digital radars are characterized by their digital signal generation and their digital signal processing, usually for the full RF bandwidth [12]. Typical digital modulation techniques include the use of binary phase shift keying (BPSK) modulated continous wave (CW) signals by PMCW radars [14]–[16], and the orthogonal multi-carrier signal employed by OFDM radars [17], [28], [35]. Digital radars appeal with their high degree of freedom in signal design and signal processing since the signal is digitally available in its full bandwidth. The focus of this thesis is to exploit this advantage in order to employ radar networks.

The following chapter establishes the theoretical foundation of this thesis by at first introducing a signal model applicable to both PMCW and OFDM radars in Section 2.1. Signal generation and processing for the aforementioned radars are then presented in Sections 2.2 and 2.3, respectively. The multiplexing of signals from different Tx channels is not only particularly important for multiple-input multiple-output (MIMO) radars, but also for radar networks. Therefore, Section 2.4 gives an overview over multiplexing techniques and radar parameterization. Finally, the concept of MIMO radars and DoA estimation is explained in Section 2.5, setting the stage for the introduction of network-based DoA estimation in later chapters.

2.1 Signal Model

This section presents a general model for digital radar signals, thereby allowing for an analogous introduction of the signal characteristics and signal evaluation of both OFDM and PMCW radars based on the same signal model. The notation used in this signal model and throughout this thesis is thereby described in Appendix A. The signal model follows the system concept depicted in Fig. 2.1.

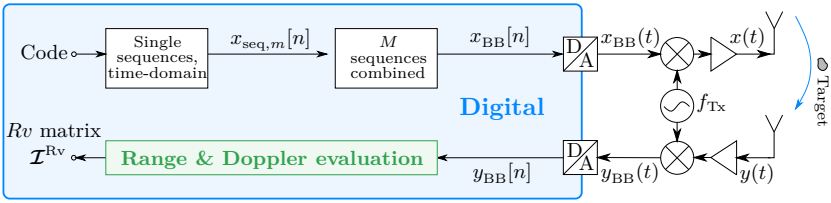

Fig. 2.1: Simplified concept of signal processing and hardware of a digital radar.

2.1.1 Transmit Signal

Digital radars typically transmit a baseband signal $x_{\mathrm{BB}}(t)$ modulated onto a CW carrier. For radars capable of estimating not only a target's range R, but also its radial velocity v, the baseband signal typically consists of M adjacent sequences $x_{\mathrm{seq},m}(t)$, with $m = 0, \ldots, M-1$ [12]. All these sequences have the same length T. They may be identical, or each individual sequence may be different, depending on the modulation type. Hence, in general the baseband signal is defined by the combination of these M sequences as

$$x_{\mathrm{BB}}(t) = \sum_{m=0}^{M-1} x_{\mathrm{seq},m}(t - mT) \tag{2.1}$$

and has a duration of $T_{\mathrm{obs}}{=}MT$ corresponding to the observation time of the radar. The baseband signal $x_{\mathrm{BB}}(t)$ is upconverted using a CW carrier of frequency f_{Tx}

$$s_{\mathrm{Tx}}(t) = \mathrm{e}^{\mathrm{j}2\pi f_{\mathrm{Tx}} t} \mathrm{e}^{\mathrm{j}\phi_{\mathrm{Tx}}(t)}\,. \tag{2.2}$$

The phase term $\phi_{\mathrm{Tx}}(t)$ includes the initial signal phase as static phase offset, as well as phase noise and frequency drifts within a measurement frame.

Depending on the system architecture, either a double-sideband (DSB) mixer or an in-phase & quadrature (IQ) upconverter is used, with the latter requiring two digital-to-analog converters (DACs) per radar Tx channel to sample the I and Q components of $x_{\mathrm{BB}}(t)$. The upconversion leads to the radar's Tx signal

$$x(t) = \sqrt{P_{\mathrm{Tx}}}\, x_{\mathrm{BB}}(t)\, s_{\mathrm{Tx}}(t) \tag{2.3}$$

where P_{Tx} is the transmit power.

2.1.2 Receive Signal

In the channel, the radar's signal is reflected at N_{T} targets and afterward received by a receiver. Depending on the target's distance to the radar R and its radial velocity v, the signal path with a reflection at the kth target introduces a time-of-flight (ToF)

$$\tau_k(t) = \tau_k^{\mathrm{R}} + \tau_k^{\mathrm{v}}(t) = \frac{2R_k}{\mathrm{c}_0} + \frac{2v_k}{\mathrm{c}_0}t, \tag{2.4}$$

assuming constant target velocity for the time-dependent ToF term $\tau^{\mathrm{v}}(t)$. The Rx signal consequently contains a superposition of all signals received via reflections at all targets; hence, it is described as

$$y(t) = \sum_{k=1}^{N_{\mathrm{T}}} \sqrt{P_{\mathrm{Rx},k}}\, x_{\mathrm{BB}}\left(t - \tau_k(t)\right) s_{\mathrm{Tx}}\left(t - \tau_k(t)\right). \tag{2.5}$$

By combining (2.2) and (2.4), the influence of the ToF on the carrier signal is described as

$$\begin{aligned} s_{\mathrm{Tx}}\left(t - \tau_k(t)\right) = {} & \mathrm{e}^{\mathrm{j}2\pi f_{\mathrm{Tx}} t}\, \mathrm{e}^{-\mathrm{j}2\pi f_{\mathrm{Tx}} \frac{2R_k}{\mathrm{c}_0}}\, \mathrm{e}^{-\mathrm{j}2\pi f_{\mathrm{Tx}} \frac{2v_k}{\mathrm{c}_0} t}\, \mathrm{e}^{\mathrm{j}\phi_{\mathrm{Tx}}\left(t-\tau_k(t)\right)} \\ \approx {} & s_{\mathrm{Tx}}\left(t - \tau_k^{\mathrm{R}}\right) \quad \mathrm{e}^{\mathrm{j}2\pi f_{\mathrm{d},k} t} \end{aligned} \tag{2.6}$$

where the Doppler frequency corresponding to the kth target is defined as

$$f_{\mathrm{d},k} = -\frac{2v_k f_{\mathrm{Tx}}}{\mathrm{c}_0}. \tag{2.7}$$

Furthermore, the time-dependency of the ToF can typically be neglected inside the delayed baseband signal $x_{\mathrm{BB}}\left(t - \tau_k(t)\right)$. This assumption is possible if the range migration is less than the size of one range cell ΔR throughout the measurement, hence $2vT_{\mathrm{obs}}/\mathrm{c}_0 < \Delta R$ [12]. Therefore, (2.5) is simplified to

$$y(t) \approx \sum_{k=1}^{N_{\mathrm{T}}} \sqrt{P_{\mathrm{Rx},k}}\, x_{\mathrm{BB}}\left(t - \tau_k^{\mathrm{R}}\right) s_{\mathrm{Tx}}\left(t - \tau_k^{\mathrm{R}}\right) \mathrm{e}^{\mathrm{j}2\pi f_{\mathrm{d},k} t}. \tag{2.8}$$

At the receiver, the signal is downconverted with the Rx carrier

$$s_{\mathrm{Rx}}(t) = \mathrm{e}^{-\mathrm{j}2\pi f_{\mathrm{Rx}} t} \mathrm{e}^{-\mathrm{j}\phi_{\mathrm{Rx}}(t)}. \tag{2.9}$$

This leads to the downconverted Rx signal

$$y_{\mathrm{BB}}(t) = \sum_{k=1}^{N_{\mathrm{T}}} A_k x_{\mathrm{BB}}\left(t - \tau_k^{\mathrm{R}}\right) \mathrm{e}^{\mathrm{j}2\pi f_{\mathrm{d},k}(t)} s_{\mathrm{Tx}}\left(t - \tau_k^{\mathrm{R}}\right) s_{\mathrm{Rx}}(t), \tag{2.10}$$

where $A_k \propto \sqrt{P_{\mathrm{Rx},k}}$ represents the amplitude resulting from each target's reflection.

Coupled Downconversion

Considering a single radar or an RF-coupled radar network (see Section 3.1.1), Tx and Rx are fed by the same carrier signal source, and thus

$$\begin{aligned} f_{\mathrm{Rx}} &= f_{\mathrm{Tx}} \\ \phi_{\mathrm{Rx}}(t) &= \phi_{\mathrm{Tx}}(t) \end{aligned} \tag{2.11}$$

can be assumed.

The range correlation effect [36] states that for small ranges, the phase noise remains largely correlated. Therefore, for small ranges, it is approximated that the phase terms of the Tx and Rx carriers are equivalent since

$$\phi_{\mathrm{Tx}}\left(t - \tau^{\mathrm{R}}\right) \approx \phi_{\mathrm{Tx}}(t) \overset{(2.11)}{=\!=} \phi_{\mathrm{Rx}}(t) \tag{2.12}$$

and cancel each other out during downconversion. Ergo, the downconverted Rx signal from (2.10) simplifies to

$$\begin{aligned} y_{\mathrm{BB}}(t) &= \sum_{k=1}^{N_{\mathrm{T}}} A_k x_{\mathrm{BB}}\left(t - \tau_k^{\mathrm{R}}\right) \mathrm{e}^{\mathrm{j}2\pi f_{\mathrm{d},k} t} \mathrm{e}^{-\mathrm{j}2\pi f_{\mathrm{Tx}} \tau_k^{\mathrm{R}}} \\ &= \sum_{k=1}^{N_{\mathrm{T}}} A_k \underbrace{x_{\mathrm{BB}}\left(t - \frac{2R_k}{c_0}\right)}_{\text{range est.}} \underbrace{\mathrm{e}^{\mathrm{j}2\pi \frac{-2v_k}{c_0} f_{\mathrm{Tx}} t}}_{\text{vel. est.}} \underbrace{\mathrm{e}^{-\mathrm{j}2\pi f_{\mathrm{Tx}} \frac{2R_k}{c_0}}}_{\text{DoA est.}} \end{aligned} \tag{2.13}$$

and only contains the components required for range, velocity, and DoA estimation.

Uncoupled Downconversion

In an uncoupled setup, like an uncoupled radar network, different signal sources are used for the Tx and Rx carrier signals. Hence, (2.11) does not apply, which corresponds to the initial situation in a typical unsynchronized radar network. Consequently, a carrier frequency offset (CFO)

$$f_{\mathrm{CFO}} = f_{\mathrm{Tx}} - f_{\mathrm{Rx}} \tag{2.14}$$

and a phase error

$$\phi_{\mathrm{err}}(t) = \phi_{\mathrm{Tx}}\left(t - \tau_k^{\mathrm{R}}\right) - \phi_{\mathrm{Rx}}(t) \tag{2.15}$$

occur. The phase error $\phi_{\mathrm{err}}(t)$ includes the uncorrelated phase noise of both carrier signal sources, as well as a static phase offset. In addition to the terms from (2.13), here, the baseband receive signal also includes the respective error terms:

$$y_{\mathrm{BB}}(t) = \sum_{k=1}^{N_{\mathrm{T}}} A_k \underbrace{x_{\mathrm{BB}}\left(t - \frac{2R_k}{c_0}\right)}_{\text{range est.}} \underbrace{\mathrm{e}^{\mathrm{j}2\pi \frac{-2v_k}{c_0} f_{\mathrm{Tx}} t}}_{\text{vel. est.}} \underbrace{\mathrm{e}^{\mathrm{j}2\pi f_{\mathrm{CFO}} t}}_{\text{CFO}} \underbrace{\mathrm{e}^{-\mathrm{j}2\pi f_{\mathrm{Tx}} \frac{2R_k}{c_0}}}_{\text{DoA est.}} \underbrace{\mathrm{e}^{\mathrm{j}\phi_{\mathrm{err}}(t)}}_{\text{phase error}} \tag{2.16}$$

These additional errors significantly affect the radar signal evaluation, which is analyzed in detail for PMCW radars in Chapter 4.

2.2 PMCW Radars

PMCW radars, sometimes also called pseudo-noise radars, are digital radars transmitting a phase-modulated CW signal, specifically, a code sequence is modulated onto the RF carrier [14]–[16]. Typically, a BPSK code is used, leading to a real-valued baseband Tx signal. Thus, it is possible to use a code-generator instead of DAC, reducing hardware costs compared to other digital radars. By transmitting multiple consecutive code sequences, the range of a target is determined by means of a correlation, while the Doppler is evaluated via the

phase progression along several sequences.

2.2.1 PMCW Baseband Signal

The baseband signal of a PMCW radar is a code sequence $x_{\mathrm{seq}}(t)$ of duration T, which is repeated M times. Typically, BPSK is used as the phase modulation scheme, which is assumed in the following without loss of generality. Consequently, the baseband signal is characterized by a code sequence $\boldsymbol{d} \in \{-1, 1\}^N$ of length N and the pulse filter $h(t)$. The time interval between adjacent pulses, in the following called chips, is defined by the code rate R_{c} as

$$T_{\mathrm{c}} = \frac{1}{R_{\mathrm{c}}} = \frac{T}{N}\,. \tag{2.17}$$

Mathematically, the baseband signal is therefore described as

$$x_{\mathrm{BB}}(t) = \sum_{m=0}^{M-1} \underbrace{\sum_{n=0}^{N-1} d[n]\,\delta\big(t-(n+mN)\,T_{\mathrm{c}}\big) * h(t)}_{= x_{\mathrm{seq}}(t-mT)}\,. \tag{2.18}$$

This corresponds to N code symbols $d[n]$, each being convoluted with the pulse filter, and together forming a sequence $x_{\mathrm{seq}}(t)$, which is repeated M times. The convolution, denoted as $*$, with the Dirac delta function $\delta(\cdot)$ describes the time at which each pulse is transmitted.

For good PMCW radar operation, it is crucial to choose a code sequence and pulse filter appropriate for the application. Typically, approximate rectangular pulses with a duration of T_{c} are used as pulse filters, e.g., in [15], [20], [37], [38]. The widespread use of rectangular pulses can be attributed to their good correlation properties and their ease of generation. Therefore, they are also used in this work. The high signal bandwidth caused by the rectangular pulse can be reduced using low-pass filters and/or harmonic rejection [16]. Alternatively, as known from communications, the bandwidth can be reduced using a raised cosine pulse function [39], [40], but this affects the correlation properties.

Furthermore, the correlation properties are strongly influenced by the code type used. In this work, the signal is encoded with an Almost Perfect Autocorrelation Sequence (APAS) that allows for theoretically perfect autocorre-

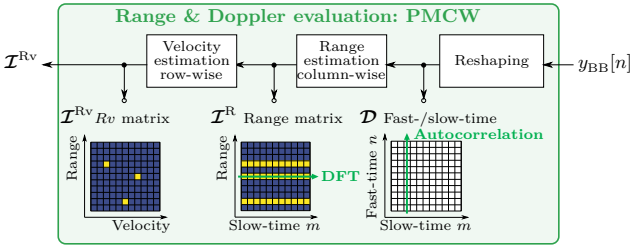

Fig. 2.2: Concept of the range and Doppler evaluation of a PMCW radar. Based on [45].

lation properties at the cost of reducing the unambiguous range by a factor of 2 [41]. Typical alternatives are maximum-length (ML) sequences [42] and Gold codes [43]. The codes differ not only in their autocorrelation performance, which determines the sidelobes occurring in range estimation, but also in the cross-correlation properties of different codes, which determines the interference susceptibility [44]. The latter is important when several radars are transmitting at the same time, or when using CDM for a MIMO radar.

2.2.2 Range & Doppler Evaluation

The range-Doppler (Rv) evaluation of a PMCW radar's Rx signal $y_{\mathrm{BB}}(t)$ as in (2.10) comprises three stages presented in Fig. 2.2. The processing steps have similarities to those of FMCW and OFDM radars, with fast-time processing employed for range estimation and the slow-time processing for velocity estimation. However, the range estimation using PMCW radars is performed through autocorrelation.

The autocorrelation can be performed either directly on the time domain signal vector $y_{\mathrm{BB}}[n]$, or in a matrix notation. While the former is preferable for real-time signal evaluation, the matrix notation is used here for the sake of clarity. Thus, the first step after sampling the Rx signal $y_{\mathrm{BB}}(t)$ is to reshape it to the fast-time/slow-time matrix $\boldsymbol{\mathcal{D}} \in \mathbb{C}^{n_{\mathrm{b}} N \times M}$. Each column of $\boldsymbol{\mathcal{D}}$ contains one code sequence. The factor

$$n_{\mathrm{b}} = f_{\mathrm{s}}/R_{\mathrm{c}} \tag{2.19}$$

is the oversampling factor, corresponding to the number of samples per chip. The signal $y_{\mathrm{BB}}(t)$ is sampled with a sample interval $T_{\mathrm{s}}{=}1/f_{\mathrm{s}}$, and consequently, the duration of one sequence corresponds to

$$T = n_{\mathrm{b}} N T_{\mathrm{s}}. \tag{2.20}$$

$\boldsymbol{\mathcal{D}}$ is described by its elements as

$$\mathcal{D}_{n,m} = y_{\mathrm{BB}}\big(nT_{\mathrm{s}} + m\,T\big) \overset{(2.13)}{=\!=} \sum_{k=1}^{N_{\mathrm{T}}} A_k \underbrace{x_{\mathrm{BB}}\left(nT_{\mathrm{s}}{+}mT{-}\frac{2R_k}{\mathrm{c}_0}\right)}_{\text{range est.}} \underbrace{\mathrm{e}^{\mathrm{j}2\pi\frac{-2v_k}{\mathrm{c}_0}f_{\mathrm{Tx}}nT_{\mathrm{s}}}}_{\text{fast-time Doppler}} \underbrace{\mathrm{e}^{\mathrm{j}2\pi\frac{-2v_k}{\mathrm{c}_0}f_{\mathrm{Tx}}mT}}_{\text{vel. est.}} \underbrace{\mathrm{e}^{-\mathrm{j}2\pi f_{\mathrm{Tx}}\frac{2R_k}{\mathrm{c}_0}}}_{\text{DoA est.}}, \tag{2.21}$$

where $n \in \{0,\dots,n_{\mathrm{b}}N{-}1\}$ corresponds to the sample within a sequence, i.e., the row of $\boldsymbol{\mathcal{D}}$, and $m \in \{0,\dots,M{-}1\}$ to the sequence, i.e., the column of $\boldsymbol{\mathcal{D}}$.

Range Estimation

The slow-time/fast-time matrix $\boldsymbol{\mathcal{D}}$ from (2.21) yields the superposition of all signals reflected from N_{T} different targets. The ranges of the targets yield different ToFs $\tau_k^{\mathrm{R}}{=}2R_k/\mathrm{c}_0$, thereby shifting the code differently in time. Consequently, the range is estimated by means of a fast-time autocorrelation. Specifically, the range matrix $\boldsymbol{\mathcal{I}}^{\mathrm{R}} \in \mathbb{C}^{n_{\mathrm{b}}N\times M}$ is computed by correlating each column of $\boldsymbol{\mathcal{D}}$ with the transmitted time domain code sequence $x_{\mathrm{seq}}(t)$. By further inserting τ_k^{R} and $f_{\mathrm{d},k}{=}{-}2v_k f_{\mathrm{Tx}}/\mathrm{c}_0$ from (2.4) and (2.7), respectively, the elements of $\boldsymbol{\mathcal{I}}^{\mathrm{R}}$ yield

$$\begin{aligned}\mathcal{I}^{\mathrm{R}}_{n,m} = \sum_{k=1}^{N_{\mathrm{T}}} \underbrace{\mathrm{e}^{\mathrm{j}2\pi f_{\mathrm{d},k}mT}}_{\text{vel. est.}} \underbrace{\mathrm{e}^{-\mathrm{j}2\pi f_{\mathrm{Tx}}\tau_k^{\mathrm{R}}}}_{\text{DoA est.}} \\ \times \underbrace{\sum_{l=0}^{n_{\mathrm{b}}N-1} \mathrm{e}^{\mathrm{j}2\pi f_{\mathrm{d},k}lT_{\mathrm{s}}} x_{\mathrm{BB}}\left(lT_{\mathrm{s}}{+}mT{-}\tau_k^{\mathrm{R}}\right) x^*_{\mathrm{seq}}\big((l{+}n)\,T_{\mathrm{s}}\big)}_{\text{autocorrelation for range estimation, including fast-time Doppler}},\end{aligned} \tag{2.22}$$

where $(\cdot)^*$ denotes the complex conjugate (not necessary for real-valued code sequences). In each column of $\boldsymbol{\mathcal{I}}^{\mathrm{R}}$, the range estimation term leads to a maximum

corresponding to a range where at least one target is shown, as depicted in Fig. 2.1. The fast-time Doppler term $e^{j2\pi f_{d,k} n T_s}$ affects $\boldsymbol{\mathcal{I}}^{Rv}$ by reducing the peak-to-noise ratio (PNR) and increasing sidelobes, as explained in detail in [46]. Its severity depends on the velocities of the targets. While the fast-time Doppler is typically disregarded, a mitigation method exists that essentially performs velocity estimation as the initial step in the signal processing chain and then compensates for the phase shifts due to fast-time Doppler [47].

Velocity Estimation

The slow-time Doppler $e^{j2\pi f_{d,k} m T}$ leads to a phase progression via the columns of $\boldsymbol{\mathcal{D}}$ and $\boldsymbol{\mathcal{I}}^{R}$. This is evaluated by means of a row-wise discrete Fourier transform (DFT)[1] denoted as $\overrightarrow{\mathrm{DFT}}[\cdot]$ in the next step. Consequently, the *Rv* matrix is computed as

$$\boldsymbol{\mathcal{I}}^{Rv} = \overrightarrow{\mathrm{DFT}}\left[\boldsymbol{\mathcal{I}}^{R}\right], \qquad \boldsymbol{\mathcal{I}}^{Rv} \in \mathbb{C}^{n_b N \times M}. \tag{2.23}$$

It contains a peak at each range and radial velocity where a target is located, as schematically shown in Fig. 2.1.

2.3 OFDM Radars

Although both OFDM and PMCW radars employ modulation schemes originating from digital communications, they significantly differ in their waveforms. In contrast to the BPSK-modulated single-carrier signal of PMCW radars, OFDM signals consists of multiple simultaneously transmitted orthogonal subcarriers. Their orthogonality is ensured by the relation of the duration T_{sym} of a single signal sequence, called OFDM symbol, and the subcarrier spacing Δf, which equals

$$\Delta f = \frac{1}{T_{sym}}. \tag{2.24}$$

OFDM is widely used in communications [48]–[51] due to advantages like its robustness against multipath propagation and the resulting intersymbol interference (ISI). In addition, OFDM allows multiplexing for multiple user access, and a straightforward consideration of frequency-selective channels and narrowband interference by their effect on the different subcarriers [51]–[53].

[1] typically implemented as fast Fourier transform (FFT)

These advantages persist in the use of OFDM as a radar waveform, a concept which first has been proposed in [17], [18], [35], [54]. Most importantly, subcarrier orthogonality inherently allows multiplexing for MIMO radars. By assigning different subcarriers to different Tx channels, a strategy called subcarrier interleaving, FDM is achieved which inherently is orthogonal, apart from Doppler-shift or CFO induced non-orthogonalities [28], [55], [56]. This is also advantageous for radar networks, where the signals of several network nodes have to be multiplexed [28], [57]. Accordingly, this section introduces the signal model of OFDM radars and the corresponding signal processing.

2.3.1 OFDM Baseband Signal

The OFDM baseband signal has a subdivided structure in both time and frequency domain. In frequency domain, it consists of N orthogonal subcarriers with a spacing of Δf. Each subcarrier is phase-modulated with an individual modulation symbol. Together, the subcarriers form a single time domain signal of duration T_{sym} called OFDM symbol. In time domain, M OFDM symbols are combined sequentially to form the OFDM signal. Unless repeat OFDM (RP-OFDM) is used and the same OFDM symbol is repeated M times, a guard interval, the so-called cyclic prefix, is inserted before every OFDM symbol. It has the duration T_{CP} and consists of the end of the following OFDM symbol. This way, ISI is avoided and delay-induced time shifts of the signal are cyclic for $\tau^{\mathrm{R}} \leq T_{\mathrm{CP}}$. The total time per OFDM symbol hence is

$$T = T_{\mathrm{sym}} + T_{\mathrm{CP}} \,. \tag{2.25}$$

Each subcarrier in each OFDM symbol is modulated by a dedicated modulation symbol, typically using quadrature phase-shift keying (QPSK). These modulation symbols are denoted in a matrix $\boldsymbol{\mathcal{D}}^{\mathrm{Tx}} \in \mathbb{C}^{N \times M}$. The baseband signal is described as

$$x_{\mathrm{BB}}(t) = \sum_{m=0}^{M-1} \sum_{n=0}^{N-1} \mathcal{D}_{n,m}^{\mathrm{Tx}} \mathrm{e}^{\mathrm{j}2\pi f_n (t - mT - T_{\mathrm{CP}})} \mathrm{rect}\left(\frac{t - \left(m + \frac{1}{2}\right) T}{T} \right) \,, \tag{2.26}$$

where

$$f_n = n\Delta f \tag{2.27}$$

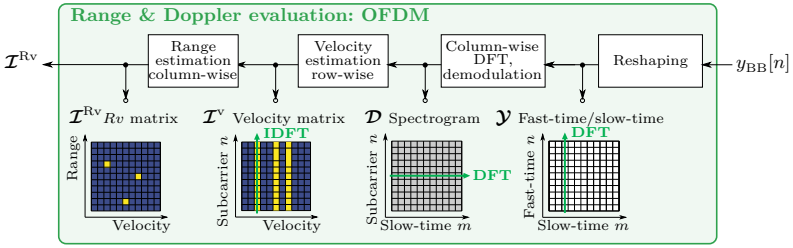

Fig. 2.3: Concept of the signal evaluation of an OFDM radar.

corresponds to the frequency of the nth subcarrier.

To generate $x_{\mathrm{BB}}(t)$, a column-wise inverse discrete Fourier transform (IDFT) denoted as $\mathrm{IDFT}\restriction[\cdot]$ is performed on $\boldsymbol{\mathcal{D}}^{\mathrm{Tx}}$. This leads to the time domain matrix $\boldsymbol{\mathcal{X}} = \mathrm{IDFT}\restriction\left[\boldsymbol{\mathcal{D}}^{\mathrm{Tx}}\right]$ with a single OFDM symbol in each column[2]. By generating the time domain signal this way, it is inherently sampled with the frequency of the highest subcarrier, thus $f_{\mathrm{s}} = f_{N-1}$. Next, the cyclic prefix (CP) is added by duplicating the last $T_{\mathrm{CP}}/f_{\mathrm{s}}$ samples of each column to its beginning. The discrete time domain signal $x_{\mathrm{BB}}[n]$ is then calculated by concatenating the columns of the matrix into a vector. Afterward, the signal is converted by a DAC, upconverted, and transmitted, which is explained in detail in Section 2.1.

2.3.2 Range & Doppler Evaluation

For the evaluation of the Rx signal, several signal processing steps are performed, as schematized in Fig. 2.3. The first step is to transform the sampled Rx signal $y_{\mathrm{BB}}[n]$ described in (2.13) into symbol domain. For this, the signal is reshaped back into a matrix and the CP is removed, leading to a time domain matrix $\boldsymbol{\mathcal{Y}} \in \mathbb{C}^{N \times M}$. Each column corresponds to the time domain Rx signal of one OFDM symbol. Then, $\boldsymbol{\mathcal{Y}}$ is transformed to symbol domain by means of a column-wise DFT, leading to $\boldsymbol{\mathcal{D}}^{\mathrm{Rx}} = \mathrm{DFT}\restriction[\boldsymbol{\mathcal{Y}}]$.

The range-dependent ToF results in a different phase shift for each subcarrier, dependent on its subcarrier frequency f_n defined in (2.27). This results in a

[2] It should be noted that all DFTs and IDFTs mentioned in this section are typically implemented as FFTs and inverse fast Fourier transforms (IFFTs), respectively.

phase progression via the subcarriers defined as

$$\theta_k[n] = -2\pi f_n \tau_k^{\mathrm{R}} = -2\pi f_n \frac{2R_k}{\mathrm{c}_0}. \tag{2.28}$$

Combining (2.13) and (2.26), the elements of $\boldsymbol{\mathcal{D}}^{\mathrm{Rx}}$ are

$$\mathcal{D}_{n,m}^{\mathrm{Rx}} = \mathcal{D}_{n,m}^{\mathrm{Tx}} \underbrace{\sum_{k=1}^{N_{\mathrm{T}}} A_k \underbrace{\mathrm{e}^{\mathrm{j}\theta_k[n]}}_{\text{range est.}} \underbrace{\mathrm{e}^{\mathrm{j}2\pi f_{\mathrm{d},k} mT}}_{\text{vel. est.}} \underbrace{\mathrm{e}^{-\mathrm{j}2\pi f_{\mathrm{Tx}} \tau_k^{\mathrm{R}}}}_{\text{DoA est.}}}_{=\mathcal{D}_{n,m}}, \tag{2.29}$$

Note that, for the sake of simplicity, the fast-time Doppler is neglected in (2.29). Nevertheless, by shifting the frequency of the subcarriers, the fast-time Doppler introduces intercarrier interference (ICI), which significantly affects $\boldsymbol{\mathcal{I}}^{\mathrm{Rv}}$ for high Doppler shifts. Therefore, the radar parameters should be chosen in a way that $f_{\mathrm{d}} \leq 0.1\Delta f$ is met [58]. Alternatively, the Doppler-induced ICI can be mitigated by using RP-OFDM and performing Doppler evaluation first, even before the complex division, as suggested in [59]. This way, the frequency shifts of the subcarriers are corrected prior to further signal processing.

For further evaluation, the Tx symbols $\boldsymbol{\mathcal{D}}^{\mathrm{Tx}}$ have to be removed. This is done by an element-wise multiplication, denoted as $\odot$, with the complex conjugate, equaling a complex division. Furthermore, the separation of the different Tx channels is done in this step. Regardless of the multiplexing strategy, each Tx channel p of the MIMO OFDM radar has its specific Tx matrix $\boldsymbol{\mathcal{D}}_p^{\mathrm{Tx}}$. Considering the Rx matrix measured at the qth Rx channel $\boldsymbol{\mathcal{D}}_q^{\mathrm{Rx}}$, the division matrix of these channels is calculated by

$$\boldsymbol{\mathcal{D}}_{pq} = \boldsymbol{\mathcal{D}}_q^{\mathrm{Rx}} \odot \left(\boldsymbol{\mathcal{D}}_p^{\mathrm{Tx}}\right)^*. \tag{2.30}$$

$\boldsymbol{\mathcal{D}}_{pq}$ contains all the information from the respective channel as stated in (2.29), but without the modulation symbols $\mathcal{D}_{n,m}^{\mathrm{Tx}}$. The division matrix $\boldsymbol{\mathcal{D}}$, from here on without loss of generality (w.l.o.g.) denoted without the channel indices pq, essentially corresponds to a spectrogram (subcarriers = frequency vs. OFDM symbols = time) containing the time- and frequency-dependent channel influences.

Velocity Estimation

The velocity estimation is performed via a slow-time DFT in accordance with PMCW velocity estimation. The velocity-matrix $\boldsymbol{\mathcal{I}}^{\mathrm{v}}$ is thus calculated by a row-wise DFT as

$$\boldsymbol{\mathcal{I}}^{\mathrm{v}} = \overrightarrow{\mathrm{DFT}}\left[\boldsymbol{\mathcal{D}}\right], \qquad \boldsymbol{\mathcal{I}}^{\mathrm{v}} \in \mathbb{C}^{N \times M}, \tag{2.31}$$

evaluating the Doppler-induced phase progression via the OFDM symbols. Note that the order of the velocity and range estimation is interchangeable.

Range Estimation

As the subcarriers have different frequencies f_n, the ToF τ^{R} causes a different phase shift on each subcarrier. This is reflected in the range-and-subcarrier-dependent phase $\theta_k[n]$ defined in (2.28), resulting in a phase progression via the subcarriers. The evaluation of this phase progression is performed utilizing an IDFT [18], as accordingly, the complex-valued *Rv* matrix is computed by

$$\boldsymbol{\mathcal{I}}^{\mathrm{Rv}} = \mathrm{IDFT}\restriction\left[\boldsymbol{\mathcal{I}}^{\mathrm{v}}\right], \qquad \boldsymbol{\mathcal{I}}^{\mathrm{Rv}} \in \mathbb{C}^{N \times M}. \tag{2.32}$$

2.4 Parameterization

Notwithstanding the dissimilarity in their waveforms, the parameterization of PMCW and OFDM radars, specifically, the relationship between signal parameters and radar performance, is essentially independent of the signal modulation scheme. The velocity is estimated in slow-time, hence, the slow-time sampling rate, i.e., the sequence length T, and the observation time $T_{\mathrm{obs}} = MT$ determine the estimation performance. For range estimation, processed in fast-time for PMCW or via the subcarriers for OFDM, length and sampling or subcarrier spacing, respectively, determine performance. However, due to the relation between subcarrier and sampling frequency of OFDM radars, both result in comparable parameter dependencies.

2.4.1 Resolution & Unambiguous Region

The resolution of the range estimation is bandwidth dependent and equals [16], [18]

$$\Delta R = \frac{\mathrm{c}_0}{2B}\,. \tag{2.33}$$

The bandwidth thereby equals $B = N\Delta f$ for OFDM radars, and $B = R_\mathrm{c}$ for PMCW radars. The unambiguous range depends on the fast-time/subcarrier sampling and equals

$$R^\mathrm{ua} = \begin{cases} \frac{\mathrm{c}_0 N}{2B} = \frac{\mathrm{c}_0}{2\Delta f}, & \text{for OFDM} \\ \frac{\mathrm{c}_0 N}{2R_\mathrm{c}}, & \text{for PMCW.} \end{cases} \tag{2.34}$$

In both cases R^ua is to be attributed to the ratio of samples per sequence to bandwidth, yet does not change by oversampling. For OFDM, this is due to the fixed relationship between the number of subcarriers and the number of fast-time samples.

For both PMCW and OFDM the velocity resolution is related to the total observation time T_obs as

$$\Delta v = \frac{\mathrm{c}_0}{2f_\mathrm{Tx}T_\mathrm{obs}}\,, \tag{2.35}$$

and the unambiguous velocity is calculated as

$$v^\mathrm{ua} = \pm\frac{\mathrm{c}_0}{4f_\mathrm{Tx}T}\,, \tag{2.36}$$

depending on the sequence time T including a potential CP in the OFDM case.

Based on these relations, the radar signal has to be parameterized according to the measurement scenario and the hardware limitations. In general, the *Rv* performance of a digital radar is largely limited by the DAC/analog-to-digital converter (ADC) sampling frequency as well as the observation time, and thus is typically constrained by hardware and data handling capabilities [13].

2.4.2 Multiplexing Strategies

When implementing MIMO radars, the parameterization also includes the number of Tx channels and the multiplexing strategy. The latter must guarantee that the N_Tx different Tx signals are separable at Rx. This is particularly

Tab. 2.1: Multiplexing strategies for digital radars.

	PMCW	OFDM
Fast-time/subcarrier separation (affects R^{ua})	Range shift [30]	FDM [28]
Fast-time/subcarrier coding (affects range est. perf.)	CDM [29]	CDM [31]
Slow-time separation (affects v^{ua}, untypical)	TDM	TDM
Slow-time coding (affects vel. est. performance)	Outer coding [30]	–
Combinations	–	Random with CS [32]

significant in the context of radar networks, where the multiplexing strategy not only includes the Tx channels of one radar, but of all sensors within the network. A brief overview of the most relevant multiplexing strategies and the corresponding literature is given in this subsection, accompanied by Tab. 2.1.

Essentially, multiplexing strategies can be classified as multiplexing in the fast-time/subcarrier domain and in the slow-time domain. Regarding the former, the most common multiplexing strategy for OFDM is FDM [28], i.e., assigning different subcarriers exclusively to certain Tx channels. For PMCW radars, orthogonality is achieved by using the same sequence but shifted in fast-time, consequently, different Tx are shifted to different ranges [30]. Both approaches typically reduce R^{ua} by N_{Tx}.

Alternatively, the sequences transmitted by different Tx can be coded differently, which is termed CDM. This is a typical multiplexing strategy for PMCW [29], though it can also be used for OFDM [31]. Since all Tx transmit simultaneously, the performance depends largely on the crosscorrelation properties of the different code sequences. In particular, artifacts or ambiguities may be introduced in the range direction, or the PNR may be affected by self-interference.

Multiplexing in the slow-time domain involves TDM, which affects v^{ua}, but is typically not used with digital radars due to disadvantages such as reduced average Tx power. For PMCW, additionally outer coding is proposed [30], which works by implementing a code over slow-time, where each chip corresponds to several consecutive sequences.

A third strategy that does not fit into the aforementioned categories is random multiplexing [32] for OFDM. Here, TDM and FDM are randomly combined. This is inherently well suited for a compressed sensing (CS) algorithm to reconstruct the gaps in $\boldsymbol{\mathcal{D}}$ while performing the Fourier transforms for range and velocity

estimation. A loss in R^{ua} or v^{ua} is avoided, at the cost of higher computational effort and decreased dynamic performance.

2.5 MIMO Radar Processing

The signal processing steps presented in Sections 2.2 and 2.3 allow for an estimation of the range and radial velocity of multiple targets. In order to create a full image of the radar's surroundings, though, an estimation of the targets angle, in the following called DoA estimation, is crucial. The most common concepts include phased arrays, where the Tx beam is electrically steered by applying phase shifts to the different antennas [60], and MIMO radars [61], [62]. Since MIMO radars appeal with high DoA performance due to the virtually increased number of array elements, specifically by combining the Tx and Rx arrays to a so-called virtual array, they are widely used in civil radar applications, e.g., for automotive [1], [5]. This kind of radars provide multiple Tx and Rx channels with their individual signal generation and evaluation, combined with a multiplexing scheme making the signals from different Tx distinguishable at Rx. Both lead to a phase progression via the respective Tx and Rx arrays, together forming a virtual array generating a so-called steering vector. This section offers a comprehensive introduction to the steering vector and virtual array, approximately following the model presented in [62]. It then continues with a brief introduction to DoA estimation algorithms.

2.5.1 Steering Vector

In the following, the steering vector is derived in three steps, accompanied by an overview given in Fig. 2.4. First, the Tx steering vector $\boldsymbol{a}_{\mathrm{Tx}} \in \mathbb{C}^{N_{\mathrm{Tx}}}$ is introduced, corresponding to the phase progression via the N_{Tx} Tx antennas and derived by analyzing the ToF from the Tx antennas to a target at azimuth angle θ. Second, the Rx steering vector $\boldsymbol{a}_{\mathrm{Rx}} \in \mathbb{C}^{N_{\mathrm{Rx}}}$ is derived analogously, based on the ToFs from the target to the N_{Rx} Rx antennas. Third, both are combined to the steering vector $\boldsymbol{a} \in \mathbb{C}^{N_{\mathrm{Tx}} N_{\mathrm{Rx}}}$, which then leads to the radar's virtual array. This way, a signal model is introduced which is easily extendable to the specific signal paths occurring in radar networks.

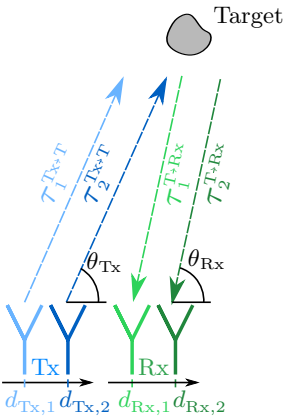

Fig. 2.4: Signal path model employed in the description of the steering vector.

Tx Steering Vector

First, the paths between each Tx antenna and a target at azimuth angle θ are considered. The ToFs $\tau_n^{\mathrm{Tx}\to\mathrm{T}}$ between the nth antenna and the target, schematized in Fig. 2.4, lead to phase offsets described by $\tilde{\boldsymbol{a}}_{\mathrm{Tx}} \in \mathbb{C}^{N_{\mathrm{Tx}}}$ as

$$\tilde{\boldsymbol{a}}_{\mathrm{Tx}} = \begin{pmatrix} \mathrm{e}^{-\mathrm{j}2\pi f_{\mathrm{Tx}} \tau_1^{\mathrm{Tx}\to\mathrm{T}}} & \mathrm{e}^{-\mathrm{j}2\pi f_{\mathrm{Tx}} \tau_2^{\mathrm{Tx}\to\mathrm{T}}} & \cdots & \mathrm{e}^{-\mathrm{j}2\pi f_{\mathrm{Tx}} \tau_{N_{\mathrm{Tx}}}^{\mathrm{Tx}\to\mathrm{T}}} \end{pmatrix} = \mathrm{e}^{-\mathrm{j}2\pi f_{\mathrm{Tx}} \tau_1^{\mathrm{Tx}\to\mathrm{T}}} \boldsymbol{a}_{\mathrm{Tx}} \,. \tag{2.37}$$

The Tx steering vector $\boldsymbol{a}_{\mathrm{Tx}}$ denotes the relative phase differences of the signals from different Tx channels at the target:

$$\boldsymbol{a}_{\mathrm{Tx}} = \begin{pmatrix} 1 & \mathrm{e}^{-\mathrm{j}2\pi f_{\mathrm{Tx}} \overline{\tau}_2^{\mathrm{Tx}}} & \mathrm{e}^{-\mathrm{j}2\pi f_{\mathrm{Tx}} \overline{\tau}_3^{\mathrm{Tx}}} & \cdots & \mathrm{e}^{-\mathrm{j}2\pi f_{\mathrm{Tx}} \overline{\tau}_{N_{\mathrm{Tx}}}^{\mathrm{Tx}}} \end{pmatrix} \tag{2.38}$$

In the following, two assumptions are made when calculating the normalized ToF $\overline{\tau}_n^{\mathrm{Tx}} = \tau_n^{\mathrm{Tx}\to\mathrm{T}} - \tau_1^{\mathrm{Tx}\to\mathrm{T}}$: First, a linear array is used, where all antennas are placed on one axis. Second, the target is in the far-field of the array, which is determined based on the Frauenhofer far-field condition as [63]

$$R > \frac{2D^2}{\lambda}. \tag{2.39}$$

This condition defines the target range, from which the outgoing signal paths are assumed to be parallel, in dependence on the size of the array D and the carrier signal's wavelength $\lambda{=}f_{\mathrm{Tx}}/\mathrm{c}_0$. Fulfilling this condition for the Tx array, the normalized ToF is calculated as

$$\overline{\tau}_n^{\mathrm{Tx}}(\theta) = \frac{d_{\mathrm{Tx},n}}{\mathrm{c}_0}\sin\theta_{\mathrm{Tx}}\,, \qquad n = \{1,\ldots,N_{\mathrm{T}}\} \tag{2.40}$$

and depends on the angle of the target relatively to the array-axis, as well as the distance from each antenna to the first antenna. Hence, $d_{\mathrm{Tx},1}{=}0$ and $\overline{\tau}_1^{\mathrm{Tx}}{=}0$ holds. As consequence, (2.38) simplifies to

$$\boldsymbol{a}_{\mathrm{Tx}} = \begin{pmatrix} 1 & \mathrm{e}^{-\mathrm{j}2\frac{2\pi}{\lambda}d_{\mathrm{Tx},2}\sin\theta_{\mathrm{Tx}}} & \mathrm{e}^{-\mathrm{j}2\frac{2\pi}{\lambda}d_{\mathrm{Tx},3}\sin\theta_{\mathrm{Tx}}} & \cdots & \mathrm{e}^{-\mathrm{j}2\frac{2\pi}{\lambda}d_{\mathrm{Tx},N_{\mathrm{Rx}}}\sin\theta_{\mathrm{Tx}}} \end{pmatrix}\,. \tag{2.41}$$

Rx Steering Vector

After a reflection at the target, the signals are received by the N_{Rx} receive channels of the radar. The Rx steering vector $\boldsymbol{a}_{\mathrm{Rx}}$, i.e. the phase differences of one signal received at different Rx channels, can thus be calculated analogously to $\boldsymbol{a}_{\mathrm{Tx}}$. Assuming a linear array and a plane wavefront, which is given by satisfying (2.39) for the Rx array, the normalized ToF at Rx, defined analogously to (2.40), can be inserted directly. The Rx steering vector thus equals

$$\boldsymbol{a}_{\mathrm{Rx}} = \begin{pmatrix} 1 & \mathrm{e}^{-\mathrm{j}2\frac{2\pi}{\lambda}d_{\mathrm{Rx},2}\sin\theta_{\mathrm{Rx}}} & \mathrm{e}^{-\mathrm{j}2\frac{2\pi}{\lambda}d_{\mathrm{Rx},3}\sin\theta_{\mathrm{Rx}}} & \cdots & \mathrm{e}^{-\mathrm{j}2\frac{2\pi}{\lambda}d_{\mathrm{Rx},N_{\mathrm{Rx}}}\sin\theta_{\mathrm{Rx}}} \end{pmatrix}\,. \tag{2.42}$$

MIMO Radar Steering Vector

Using a MIMO radar, all N_{Tx} Tx signals are received by all N_{Rx} Rx channels. Therefore, the resulting combined phase progression, the so-called steering vector $\boldsymbol{a}$, can be calculated as a combination of the Tx and Rx steering vectors from (2.41) and from (2.42), respectively. Using the Kronecker product denoted as $\otimes$, $\boldsymbol{a}$ is defined as

$$\boldsymbol{a} = \boldsymbol{a}_{\mathrm{Tx}} \otimes \boldsymbol{a}_{\mathrm{Rx}}\,. \tag{2.43}$$

This steering vector is based on an advantageous combination of the Tx and Rx array, also known as the virtual array.

2.5.2 Virtual Array

Fulfilling the far-field condition (2.39) for the whole MIMO array, the paths from Tx to the target and from the target to Rx shown in Fig. 2.4 can be assumed to be parallel, hence $\theta_{\mathrm{Tx}} \approx \theta_{\mathrm{Rx}} \approx \theta$. Considering the Tx and Rx arrays, defined by the positions of the Tx and Rx elements, respectively, as

$$\boldsymbol{d}_{\mathrm{Tx}} = \begin{pmatrix} d_{\mathrm{Tx},1} & d_{\mathrm{Tx},2} & \cdots & d_{\mathrm{Tx},N_{\mathrm{Tx}}} \end{pmatrix} \tag{2.44}$$

$$\boldsymbol{d}_{\mathrm{Rx}} = \begin{pmatrix} d_{\mathrm{Rx},1} & d_{\mathrm{Rx},2} & \cdots & d_{\mathrm{Rx},N_{\mathrm{Rx}}} \end{pmatrix} \tag{2.45}$$

and defining $\exp(\cdot)$ as the element-wise exponential function, the steering vector can consequently be calculated as

$$\boldsymbol{a} = \exp\left(-\mathrm{j}2\frac{2\pi}{\lambda}\,\boldsymbol{d}_{\mathrm{Tx}}\sin\theta\right) \otimes \exp\left(-\mathrm{j}2\frac{2\pi}{\lambda}\,\boldsymbol{d}_{\mathrm{Rx}}\sin\theta\right) = \exp\left(-\mathrm{j}2\frac{2\pi}{\lambda}\,\boldsymbol{d}\sin\theta\right) . \tag{2.46}$$

The virtual array $\boldsymbol{d} \in \mathbb{R}^{N_{\mathrm{Tx}}N_{\mathrm{Rx}}}$ of the radar is therefore defined as

$$\boldsymbol{d} = \boldsymbol{d}_{\mathrm{Tx}} \oplus \boldsymbol{d}_{\mathrm{Rx}} , \tag{2.47}$$

where $\oplus$ corresponds to the additive version of the Kronecker product as defined in Appendix A.2. This results in an additive combination of all elements of $\boldsymbol{d}_{\mathrm{Tx}}$ and $\boldsymbol{d}_{\mathrm{Rx}}$, corresponding to a spatial convolution of the Tx and Rx arrays.

By an appropriate choice of $\boldsymbol{d}_{\mathrm{Tx}}$ and $\boldsymbol{d}_{\mathrm{Rx}}$, a satisfactory virtual array can be designed, which facilitates a good DoA estimation. Specifically, the virtual array should lead to a DoA estimation with a high resolution, but without or with low ambiguities. In the simplest case, the virtual array $\boldsymbol{d}$ equals a uniform linear array (ULA) with a $\lambda/2$ spacing, leading to an 180° unambiguous region.

2.5.3 DoA estimation

The goal of the DoA estimation is to calculate one or multiple target angles θ based on a measured steering vector $\boldsymbol{a}$. In principle, this corresponds to different spatially sampled frequencies, where the virtual antennas are the sample points. Thus, the DoA estimation is performed by frequency-estimation algorithms, from a straightforward Fourier transform [64], over correlation-based maximum likelihood (ML) methods using calibration data [65], to sophisticated algorithms

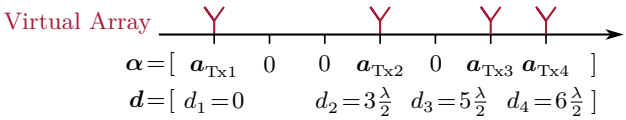

Fig. 2.5: Extended steering vector $\boldsymbol{\alpha}$ for a four-element virtual array.

like multiple signal classification (MUSIC) [66]. Prerequisite is a mitigation of all additional phase terms occurring, e.g., due to the path lengths on the radar frontend, by means of a calibration [65].

For a DFT-based DoA estimation, the virtual array must fit into a grid, which typically is a $\lambda/2$ grid. By assigning the elements of the steering vector to the respective grid positions in accordance to the virtual array, and filling empty positions in between with zeros, the extended steering vector $\boldsymbol{\alpha}$ is formed. This is shown in Fig. 2.5. Each target is introducing a phase progression along the virtual array, in the following called angular frequency Ψ defined as

$$\Psi = \frac{2\pi}{\lambda} \sin\theta \,. \tag{2.48}$$

Consequently, the angle spectrum containing the targets' angles as frequency components are calculated by a DFT as

$$\mathbf{A}\left[\Psi\right] = \mathrm{DFT}\left[\boldsymbol{\alpha}\right] \tag{2.49}$$

containing maxima for each Ψ_θ corresponding to a target angle.

For sparse virtual arrays, this DFT-based DoA estimation can be combined with a CS algorithm for the reconstruction of the empty positions in $\boldsymbol{\alpha}$ [67]. This may also be well-applicable to radar networks, which inherently tend to have gaps in their virtual array due to the gaps between the sensor nodes.

3 Radar Networks – Overview and Classification

The concept of synchronizing and cooperatively combining multiple radar sensors has its origins in multistatic sensing with widely distributed radars, e.g., for air surveillance [68], [69], and multistatic synthetic aperture radar (SAR) [70], [71].

In recent years, however, there has been a notable surge in interest in radar networks operating at higher frequencies, driven by the increasing demands of autonomous driving and driver assistance systems [1], [72]. The necessity for high-resolution DoA estimation, which in turn requires the use of very large apertures, has led to the development of increasingly larger radar sensors [6]. However, this is constrained by the available space and costs involved [5]. In this context, radar networks are a promising solution, allowing to span a wide aperture via multiple sensor nodes by means of network-based DoA estimation [11], [73], [74].

A **radar network** thereby is defined as a system composed of multiple radar sensors cooperatively working together; a **sensor node** represents one single radar sensor within such a network. The latter may be a full radar sensor, including one or multiple Tx channels and one or multiple Rx channels, and the respective backend, or a more simple device such as a repeater [11], [73]. The definition of a node, though, is often vague, since multiple nodes may be connected to the same backend [75], i.e., the part of the system which contains DACs and ADCs as well as the raw-data signal processing unit. Thus, in the following, a node is defined by having its RF monolithic microwave integrated circuits (MMICs) and antennas on the same hardware unit, e.g., printed ciruit board (PCB). An exchangeable antenna PCB, for example, connected via waveguide transition as used later in this work, is defined as one hardware unit with the respective frontend PCB containing the MMICs.

Combining several sensor nodes in a network leads to multiple radar signals and signal paths, which in the following are characterized as monostatic and bistatic. **Monostatic** refers to a signal using a Tx–Rx channel pair from the same sensor node, thus corresponding to conventional radar operation. The term thereby is defined in a radar network point-of-view, not in an antenna

point-of-view. **Bistatic** in contrast refers to a signal using a Tx–Rx channel pair from different sensor nodes. The paths of both monostatic and bistatic signals are exemplarily shown in Fig. 1.1.

Exploiting both, the monostatic and bistatic signals, is advantageous in multiple applications. One of them is the aforementioned network-based DoA estimation, making use of a radar network's extended aperture. Moreover, in distributed radar networks, where the aspect angles of the sensor nodes significantly differ, the bistatic backscatter characteristics may diverge from the monostatic ones depending on the target geometry. This allows to extract additional target information and for some target geometries features a bistatic radar cross section (RCS) higher than the monostatic one [76]–[78]. In remote sensing, bistatic radar measurements allow for single-pass SAR interferometry to generate elevation models [79], [80], for soil moisture estimation [81], [82], and for displacement and vegetation monitoring [83], [84]. However, precondition for an error-free bistatic signal evaluation is coherency, requiring a synchronization of the sensor nodes.

Several different radar network architectures follow distinct paths toward coherency, as presented in a concise overview within this chapter. They are classified by the terms *coupled* and *uncoupled* as well as *coherent* and *incoherent*, which are introduced in Section 3.1 and Section 3.2, respectively. The most sophisticated radar networks thereby are uncoupled coherent radar networks, on which a brief literature overview is given in Section 3.3.

3.1 Coupled & Uncoupled Radar Networks

One key characteristic of radar networks is the coupling of the sensor nodes, defined on hardware level. Specifically, in a *coupled* radar network, multiple sensor nodes share a clock signal via cables to which they are synchronized. An *uncoupled* radar network in contrast has no cable-based clock distribution. Consequently, as derived in (2.16), this induces errors such as CFO, phase offsets, and phase noise. Further, the DACs/ADCs of a digital radar in this case are uncoupled as well, leading to sample frequency offset (SFO).

3.1.1 Radio-Frequency Coupled Radar Networks

In RF coupled radar networks, the RF clock itself, i.e., a carrier signal or a radar RF signal (e.g., frequency ramps for FMCW radars) are distributed among the sensor nodes via cables. This signal may be at a lower fraction of the Tx frequency, e.g., when using subharmonic mixers. Still, for 77-GHz radars, it is in the double-digit GHz-region, making expensive and susceptible RF cables necessary. The downconversion therefore is described by equations (2.11)–(2.13), leading to f_{CFO}=0 and ϕ_{err}=0. If further the DACs/ADCs are synchronized and thus no SFO occurs, those radar networks are fully coherent. They show no incoherency-induced performance reduction compared to a monostatic signal evaluation. Examples of RF coupled radar synchronization include [85]–[87]. A possibility to partly overcome the drawbacks of RF cables is an RF clock distribution via fiber-optic cables [88], [89].

3.1.2 Low-Frequency Coupled Radar Networks

In low frequency (LF) coupled radar networks, a reference clock signal in the MHz-range or below is distributed among various sensor nodes. In contrast to RF-coupled networks, where the distributed signal is used directly or just frequency-multiplied, here, the distributed signal is used as a reference for a synthesizer stage, typically a phase-locked loop (PLL). Thus, while the frequencies are synchronized and no CFO or SFO occurs, the phase noise is only partially correlated [90]. Furthermore, phase errors may occur due to phase-ambiguities in fractional-N PLLs [91]. Still, they appeal due to the low-costs and simplicity, since neither RF-cables, nor complex signal processing for synchronization is necessary. In [8], [74], [92], it is successfully shown that LF coupled radar networks can be used for network-based DoA estimation. Nonetheless, the sensor nodes have to be connected by MHz-capable cables, limiting flexibility in their placement.

3.1.3 Uncoupled Radar Networks

The most flexible radar networks in terms of system design and sensor node placement are uncoupled networks. These radar networks do not rely on a cable-based clock signal distribution among the sensor nodes. However, this

introduces various error sources: First, the carrier signals at the Tx and Rx, used for up- and downconversion to and from RF, are generated by two independent signal sources (local oscillators (LOs)). This causes a CFO (2.14), as well as a phase offset and uncorrelated phase noise (2.15). Hence, the baseband signal includes those errors, as described by (2.16). Second, in an uncoupled digital radar network setup, not only the carrier signal sources are uncoupled, but so are the reference clocks of the DACs and ADCs. For bistatic signals, this results in different sample frequencies at Tx and Rx, $f_{\mathrm{s,Tx}}$ and $f_{\mathrm{s,Rx}}$, respectively. This leads to the SFO defined as

$$f_{\mathrm{SFO}} = f_{\mathrm{s,Tx}} - f_{\mathrm{s,Rx}} \,. \tag{3.1}$$

The SFO results in a temporal stretching or compression of the bistatic signal, making it barely useful if no countermeasures are taken, as shown later.

3.2 Coherent & Incoherent Radar Networks

While the aforementioned coupling of the network nodes is defined from a hardware point-of-view, coherency is defined from a signal-processing point of view. Coherency refers to the phase- and frequency consistency between two network nodes at the point of digital signal processing. Thus, an uncoupled radar network, which is incoherent at downconversion due to different carrier signal sources, may become coherent if coherency is retrieved within signal processing steps, as shown later.

Achieving coherency allows to exploit the full potential of a radar network by mitigating synchronization errors in the bistatic signal evaluation. This allows the use of the bistatic signal, like in the aforementioned applications, either by directly exploiting the bistatic signal [77], [83], [84] or by using it for network based DoA estimation [11], [73], [74], or multistatic SAR [70], [78], [93]. Without coherency, the occurring CFO, SFO, phase offsets, and phase noise make a bistatic signal processing barely useful. Thus, incoherent radar networks are rather used in a sensor-fusion approach, combining several monostatic measurements [94], [95], allowing to exploit the different aspect angles of different sensor nodes, e.g., for the instantaneous estimation of a target's velocity vector [96].

For a fully coherent radar network, three properties regarding frequency offsets, static phase errors, and phase noise, respectively, must be fulfilled:

frequency coherency, phase coherency, and correlated phase noise.

Condition I – Frequency Coherency

Frequency offsets significantly affect the bistatic signal evaluation: The CFO creates a frequency shift of the whole baseband signal, typically resulting in a velocity offset. The SFO results in a temporal stretching or compression of the signal at the receiver. In details, these effects of frequency offset on the radar signal are described in Chapter 4 for PMCW radars, and in [10] and by the author in [56] for FMCW and OFDM radars, respectively. To establish frequency coherency, both CFO and SFO must either be avoided beforehand or mitigated by means of signal processing. A straight-forward way to avoid CFO and SFO is to distribute a clock signal using a coupled radar network. This leads to a joint reference for both the carrier signal sources as well as DACs/ADCs, inherently resulting in frequency coherency. In contrast, in uncoupled radar networks, dedicated synchronization techniques are necessary to achieve frequency coherency.

Condition II – Phase Coherency

Phase coherency refers to static phase offsets, usually occurring due to different phases of the RF carriers at Tx and Rx. These phase offsets typically affect both, uncoupled as well as low-frequency coupled setups. If these phase offsets are not compensated for, network-based DoA estimation is hardly feasible. A common countermeasure is to use double-elements in the virtual network-array (VNA) for correction [10], [74]. By having virtual antenna elements from two bistatic subarrays at the same virtual position, the target-induced phase can be assumed to be identical, and the remaining phase error can be estimated. However, this reduces array design flexibility. Consequently, the radar networks presented in this thesis aim for signal processing-based correction methods independent of the VNA.

Condition III – Correlated Phase Noise

Third, the measurement must not be affected by uncorrelated phase noise. In contrast to frequency offsets, which lead to a linear phase-rotation over time, phase noise is a stochastic process [97]. For monostatic radars and RF-coupled

radar network, the phase noise of the carrier signals at Tx and Rx is correlated, leading to correlated and thus mitigated phase noise in the Rx signal due to range correlation [36]. This does not apply to uncoupled radar networks, thus, signal evaluation typically is impacted by phase noise. An exception are radar-repeater networks [11], [73], [98], in which all signals are up- and down-converted at the radar node, whereas the additional repeater nodes receive the radar signal and only apply a frequency shift in the kHz-region. Hence, the repeaters are not introducing significant phase noise and the phase noise of their bistatic signals remains correlated.

Practical Coherency

Theoretically fully meeting all three conditions in a radar network is very difficult to achieve. Even monostatic radars do not achieve completely correlated phase noise due to signal ToF [36]. However, the evaluated signal of a radar or radar network may not be significantly affected by incoherency-induced effects, even though theoretical violations of the three conditions occur. Still, those violations must not exceed certain limitations for the network to be practically coherent. The limit until which radar signal evaluation is not affected depends on the radar parameters, and is mathematically described by the author in [56] for digital radar networks, and in [10] for analog FMCW radars. In this thesis, a radar network is considered as coherent if it achieves practical coherency.

3.3 Uncoupled Coherent Radar Networks

Combining the flexibility of uncoupled sensor nodes with the capabilities of a coherent radar network, uncoupled coherent radar networks are the most sophisticated type of networks. Different strategies have been proposed to achieve coherency without coupling, which are briefly introduced in the following, accompanied by an overview given in Tab. 3.1.

Over-the-air (OTA) synchronization has similarities with coupled radar networks, but instead of a cable, a dedicated wireless connection is used in addition to the radar signal, e.g., using a different Tx frequency [99]. Multiple proposed radar networks try to avoid dedicated synchronization signals at all: In [10], [91], [100], networks are proposed which retrieve phase- and frequency coherency by estimating phase- and frequency errors. For example, they exploit

Tab. 3.1: Selected work of partly or fully coherent uncoupled radar networks.

	Mod.	f_{Tx} (GHz)	Sync.	Freq. Coh.	Phase Coh.	Phase Noise Correlated	Application
[99]	FMCW	5.8	OTA	Yes	No	No	Bistatic Radar Meas.
[100]	FMCW	122	SP[a]	Yes	Yes	(No)[b]	Proof-of-Concept
[9], [91]	FMCW	160	SP, RT[c]	Yes	Yes	(No)[b]	NW-based DoA-est.
[10]	FMCW	77	SP	Yes	VA[d]	(No)[b]	NW-based DoA-est.
[101]	FMCW	24	SP, RL[e]	Yes	Yes	Yes	Proof-of-Concept
[102]	FMCW	77	SP, RL[e]	Yes	Yes	Yes	Back-Projection
[56]	OFDM	77	SP	Yes	No	No	Proof-of-Concept
[98]	FMCW	77	RP[f]	Inherent	(No)[g]	Inherent	NW-based DoA-est.
This, [73]	OFDM	77	RP	Inherent	Yes	Inherent	NW-based DoA-est.
This, [11]	OFDM	77	RP[h]	Inherent	Yes	Inherent	NW-based DoA-est.
This, [45]	PMCW	77	SP, RL[e]	Yes	Yes[i]	Yes	Proof-of-Concept

[a] SP: Signal processing; [b] No phase noise compensation, but uses references with very low phase noise, thus, no significant phase noise; [c] RT: Using a reference target, e.g., lense; [d] VA: Using double element in the VNA; [e] RL: Reference link, e.g., LoS, path; [f] RP: Repeater; [g] Phase offset considered by CS-based DoA algorithm; [h] Repeater fed by LoS path; [i] 180° unambiguous region.

a reference target [91] or the symmetry of the errors of the bistatic signals between two network nodes [10]. In [101] and [102], phase noise is mitigated by exploiting the symmetry of the bistatic phase errors. In contrast, radar-repeater networks allow for uncoupled sensor nodes, however, up- and downconversion are performed at one main radar sensor only. This preserves frequency coherency and correlated phase noise [11], [73], [98].

The radar networks presented in this thesis are included at the bottom of Tab. 3.1. To the best knowledge of the author, they are the first uncoupled radar networks using digitally modulated waveforms, and are, upon today, the only digital-radar-based networks achieving full coherency. They differ in network design and signal processing, and are introduced and compared in the following chapters.

4 Network Concept I – Synchronization of Uncoupled PMCW Radars

Synchronizing a radar network solely based on Rx side signal processing aims towards an appealing type of radar network—where no, or just minimal hardware adaptations have to be made to achieve coherency. This idea is facilitated by the information availability using digital radars. By digitizing the baseband signal with its full bandwidth, typically resembling the RF bandwidth, all information are preserved. This includes frequency offsets, phase offsets, and phase noise. The key challenges for Rx-side synchronization techniques are the extraction and compensation of these errors. Thus, a waveform should be chosen where this information is well accessible. This makes single-carrier waveforms a good candidate to be used with Rx-side synchronization.

A radar type using single-carrier waveforms are PMCW radars. They use BPSK-modulated single-carrier signals, a waveform well-known in communications [103], [104]. For the synchronization of BPSK communication systems PLL-based Costas loops [105], [106] and squaring loops [107] have been proposed. However, synchronization techniques from communications aim to extract the information encoded in the signal—not the channel information. Consequently, when synchronizing radars, these methods must be thoroughly adapted.

This chapter introduces an uncoupled coherent radar network based on PMCW radars. It is referred to as PMCW-based radar network with carrier recovery (CRNW) and uses Rx-side synchronization. This concept has first been presented in [45] by the author, and employs a timing recovery to correct SFO as well as a carrier recovery. The latter allows for a coherent intradyne downconversion from an intermediate frequency (IF)-carrier, mitigating carrier-induced phase offsets and phase noise. The chapter starts with an overview of the radar network architecture and the 77-GHz measurement system in Section 4.1. This is followed by a thorough investigation of the effects on PMCW radar signal processing caused by CFO, SFO, and phase noise in Section 4.2. Then,

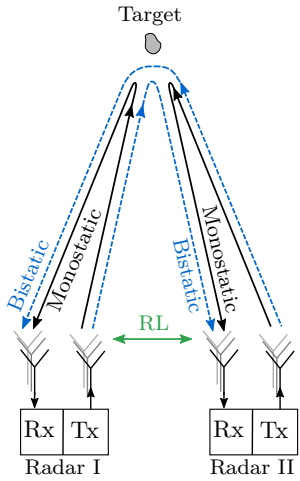

Fig. 4.1: Exemplary concept of a CRNW with two sensor nodes, including the signal paths.

the aforementioned synchronization techniques are introduced. In particular, Section 4.3 introduces the timing recovery, and Section 4.4 presents the carrier recovery. Both are verified by measurements presented in Section 4.5.

4.1 System and Measurement Setup

The fundamental concept of a typical radar network cosisting of two or more sensors with complete signal generation and evaluation is depicted in Fig. 4.1. Besides their independent monostatic signals, each radar also receives the bistatic response transmitted by the respective other. Moreover, a direct path referred to as reference link (RL) is shown, which is a prerequisite for a well-functioning carrier recovery, as detailed in Section 4.4. This path either corresponds to a LoS path or to mutual coupling between the antennas.

To achieve and analyze synchronization methods for PMCW radars, a measurement setup is chosen that allows for the individual analysis of the effects caused by the lack of coupling. Furthermore, it allows to verify the performance

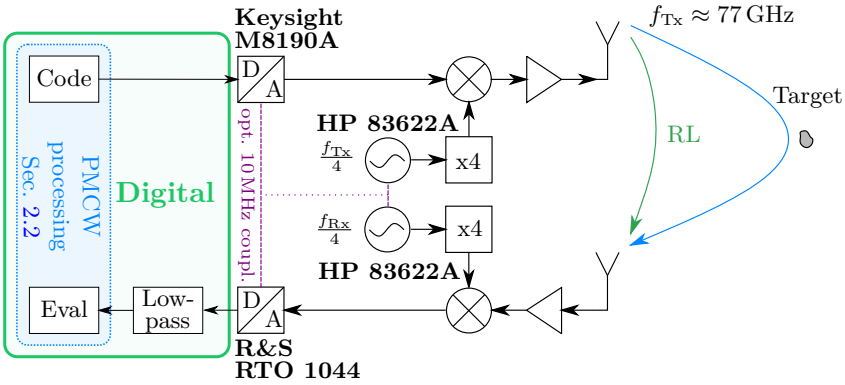

Fig. 4.2: 77-GHz measurement system and digital signal processing for conventional PMCW operation without carrier and timing recovery. Based on [45].

of the proposed algorithms both separately and in combination. In particular, in contrast to the network of two MIMO radars shown in Fig. 4.1, a reduced setup consisting of one transmitter and one receiver is chosen. It enables an individual low-frequency coupling of the DAC/ADC and the LOs, which facilitates the analysis of each coupling-induced error on its own.

An overview of the implemented 77-GHz measurement system is given in Fig. 4.2. The baseband signal is generated using a Keysight M8190A arbitrary waveform generator (AWG) providing the DAC. Afterwards, the signal is upconverted using a DSB mixer and an HP 83622A as LO. Since the subharmonic mixer multiplies the carrier frequency by four, the HP 83622A generates an LO signal at $f_{\mathrm{Tx}}/4$. A photography of the analog frontend is presented in Fig. 4.3. On the Rx side, the signal is downconverted using another HP 83622A and the same type of mixer before being digitized by an R&S RTO 1044. An optional low-frequency coupling can be introduced by connecting all or some of the measurement devices to the same 10 MHz reference.

The PMCW signal parameters used throughout this chapter are summarized in Tab. 4.1. A PMCW code sequence, an APAS code of length N=4008, is

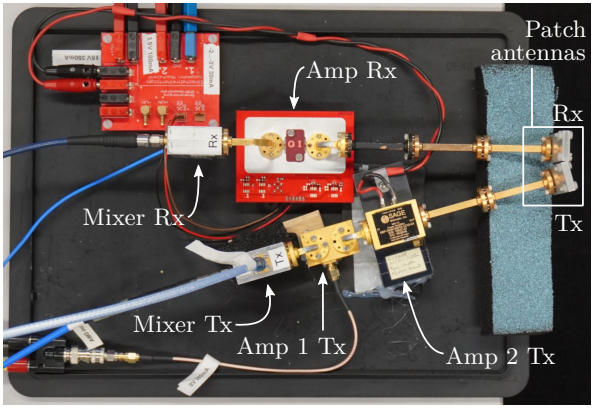

Fig. 4.3: Photography of the analog frontend of the measurement system. From [45], CC BY 4.0 https://creativecommons.org/licenses/by/4.0/.

Tab. 4.1: PMCW radar parameters.

Carrier frequency	f_c	77 GHz
Code rate	R_c	1 GHz
Code length	N	4008
Code type		APAS
Pulse function		rect
Code repetitions	M	256
Range resolution	ΔR	0.15 m
Velocity resolution	Δv	1.89 $\frac{\text{m}}{\text{s}}$
Unambiguous range, considering APAS	R^{ua}	300.4 m
Unambiguous velocity	v^{ua}	$\pm$242.9 $\frac{\text{m}}{\text{s}}$

generated with a code rate of R_c=1 GHz and a rectangular pulse function in order to obtain good auto-correlation properties. The DAC uses a sample frequency of 1 GHz, equaling the code rate. At the ADC, a sample frequency of at least 4.2 GHz is required, as for the carrier recovery the Rx signal is not sampled in baseband but modulated on an 1.1 GHz IF carrier. However, due the lack of a matching anti aliasing lowpass filter (LP), a sample frequency of 10 GHz is used, exploiting the build-in filter of the oscilloscope.

4.2 Analysis of Incoherency Impacts

In Section 2.1.2, the differences between coupled downconversion, typical for single radar sensors, and the downconversion of the bistatic signal in an uncoupled radar network have been discussed. The latter introduces phase noise and CFO, since neither the phase nor the frequency of the LOs match, as derived in (2.16). In addition, the sample frequencies of DAC and ADC are not synchronized in an uncoupled radar network, which introduces an SFO as defined in (3.1), either stretching or compressing the Rx signal in time. All three have significant effects on the *Rv* image, which are thoroughly analyzed and mathematically derived within this section.

4.2.1 Impact of Carrier Frequency Offsets

As shown in (2.16), the CFO f_{CFO}, which is an offset between the LO frequencies at Tx and Rx, results in a frequency offset of the downconverted signal $y_{\mathrm{BB}}(t)$. This frequency offset is comparable to a Doppler shift in the Rx signal as caused by the motion of the targets in the channel. In the *Rv* matrix, the CFO therefore appears as a velocity offset, shifting all targets by

$$v_{\mathrm{err}} = \frac{1}{2}\frac{f_{\mathrm{CFO}}}{f_{\mathrm{Tx}}}\mathrm{c}_0\,. \tag{4.1}$$

In addition, similar to Doppler shifts, a CFO also affects the auto-correlation performed for the range estimation, hence reducing PNR and increasing sidelobes [46].

4.2.2 Impact of Phase Noise

Using an RF-coupled Tx–Rx pair, phase noise is significantly reduced for small R due to the range correlation effect [36]. For uncoupled Tx–Rx pairs, though, this reduction does not occur, because the LO sources are uncoupled resulting in uncorrelated phase noise.

Within the PMCW radar signal evaluation, phase noise affects the *Rv* image in two ways. Both are visible in Fig. 4.4, showing the results of complex-baseband PMCW radar simulations of a single target at R=1 m and v=0 $\frac{\mathrm{m}}{\mathrm{s}}$. The simulation results without phase noise and with the phase noise shown in

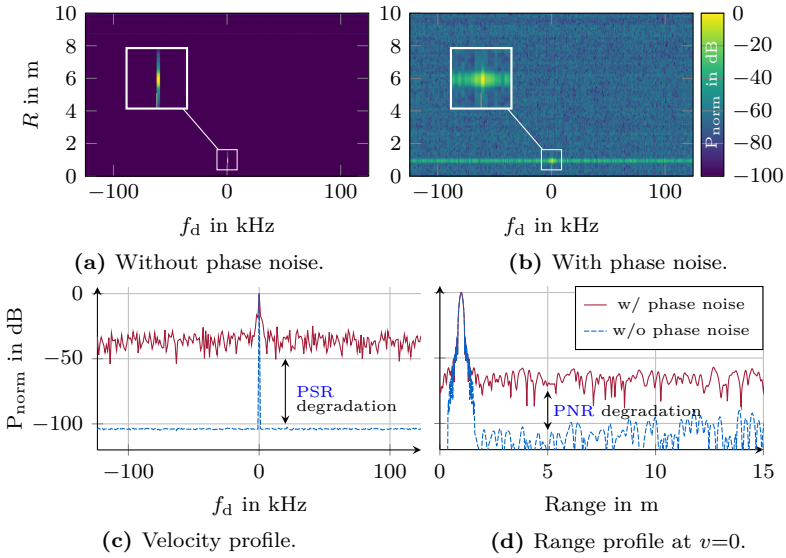

(a) Without phase noise. **(b)** With phase noise.

(c) Velocity profile. **(d)** Range profile at v=0.

Fig. 4.4: Simulation of a single target, with and without phase noise. Adapted from [45], CC BY 4.0 https://creativecommons.org/licenses/by/4.0/.

Fig. 4.5 (left) are juxtaposed. The first effect is the phase noise impact on the received code sequence $x_{\text{seq}}(t)$, resulting in a disturbed sequence

$$\tilde{x}_{\text{seq}}(t) = x_{\text{seq}}(t)\mathrm{e}^{\mathrm{j}\phi_{\text{err}}(t)} \tag{4.2}$$

impacting the autocorrelation from (2.22) and leading to an increased noise floor [108]. This is visible by comparing 4.4 (a) and 4.4 (b)—in the latter, the PNR is decreased by 35 dB due to the induced phase noise.

The second effect results from the presence of phase noise in the Doppler FFT from (2.23). The output of the Doppler FFT corresponds to the spectrum of the downconverted Rx signal. Consequently, phase noise gets visible in the result of the velocity estimation, causing a skirt corresponding to the phase noise of the LOs. It has to be noted that the power of the skirt depends not only on the phase noise PSDs $\mathcal{L}(f_{\text{offset}})$ of the LOs, but also on the resolution

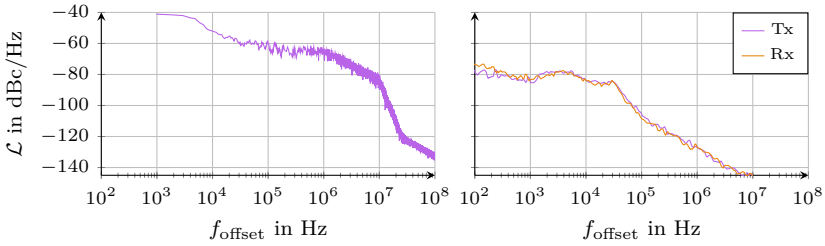

Fig. 4.5: Phase noise power spectral density (PSD) used in simulations (left) and of the HP 83622A signal sources (right). From [45], CC BY 4.0 https://creativecommons.org/licenses/by/4.0/.

Δf_{d} of the Doppler FFT. This resolution determines the sampling of the phase noise, leading to a skirt with power distribution of

$$P_{\text{pn}}(f_{\text{offset}})\big|_{\text{dBc}} = \Delta f_{\text{d}}\ \mathcal{L}(f_{\text{offset}})\big|_{\frac{\text{dBc}}{\text{Hz}}}\,. \tag{4.3}$$

The skirt extends along the velocity cells at the same range, i.e., the corresponding velocity profile, as visible in Fig. 4.4 (b). Thus, the detection of weak targets is affected if also a strong target is present at the same range. This degradation of dynamic range in the velocity profile is exemplarily visible in Fig. 4.4 (c).

For a further verification of the phase noise induced impacts, measurements using the system presented in Section 4.1 are performed. The scenario includes the RL caused by mutual coupling of the antennas. As target, a stationary corner reflector is placed at R=4.3 m. In Fig. 4.6 the results of two measurement are compared: one with uncoupled LOs, and one with low-frequency coupled LOs using a 10 MHz reference. In both cases, the DAC and ADC are coupled by means of a second 10 MHz reference to avoid additional errors caused by SFO. When employing the LO uncoupled, a strong velocity skirt is visible, which is approximately 35 dB higher than in the low-frequency coupled setup. Furthermore, a CFO of f_{CFO}=6.8 kHz occurs, with the peak being mirrored due to the single-sideband (SSB) mixer. In the low-frequency coupled case, no frequency error is observed. However, a smaller velocity skirt is still noticeable. This outcome is expected, since the additional phase noise caused by the LOs' PLLs remains uncorrelated [90]. Furthermore, the PNR is decreased by 4 dB in

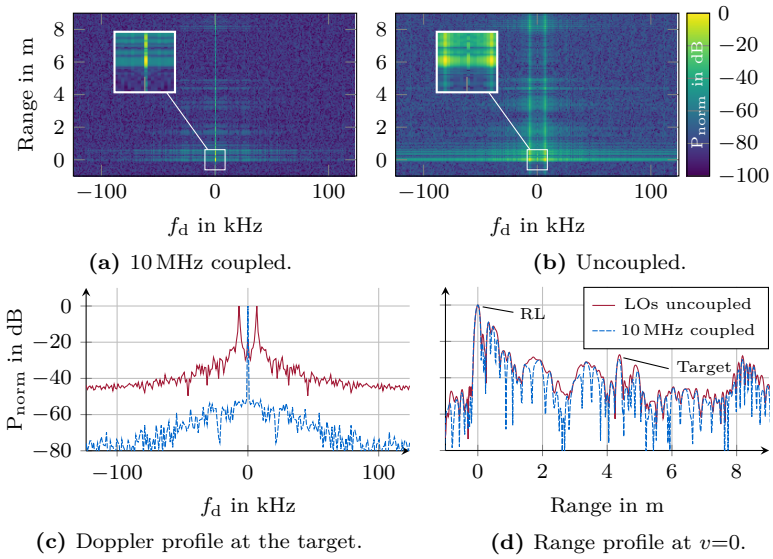

(a) 10 MHz coupled. **(b)** Uncoupled.

(c) Doppler profile at the target. **(d)** Range profile at v=0.

Fig. 4.6: Measurement results of a corner reflector at R=4.3 m, including the mutual coupling of the antennas marked as RL. From [45], CC BY 4.0 https://creativecommons.org/licenses/by/4.0/.

the uncoupled scenario. Since non-idealities in the measurement system cause sidelobes in the range profile, this reduction is yet not discernible in Fig. 4.6 (d).

In conclusion, both measurements and simulations confirm, that phase noise significantly affects the dynamic range of the *Rv* image. The severity of the effects, including the velocity skirt and the loss of PNR, depends on the phase noise PSDs of the LOs.

4.2.3 Impact of the Sample Frequency Offset

In the uncoupled radar network setup, not only the LO sources are uncoupled, but so are the reference clocks of the DAC and ADC. Different sample frequencies f_s at Tx and Rx side are present, which heavily impacts the radar signal evaluation. The signal model introduced here for the mathematical analysis of

the sample frequency errors follows the model in [109]. Both, the DAC and ADC, deviate from their expected sample frequency. However, since not the absolute but only the relative sample frequency offset between Tx and Rx is of interest, in the following the Tx sample frequency is considered as the correct one. The so-called expected sample frequency f_s hence equals the Tx sample frequency, $f_\mathrm{s} = f_{\mathrm{s,Tx}}$, whereas the Rx-side sample frequency considered as erroneous equals

$$\tilde{f}_\mathrm{s} = f_{\mathrm{s,Rx}} = f_\mathrm{s} - f_\mathrm{SFO}. \tag{4.4}$$

The SFO leads to the sample interval T_s being miss-timed by the timing error

$$\Delta T_\mathrm{s} = \delta \cdot T_\mathrm{s} \overset{|\delta| \ll 1}{\approx} \frac{f_\mathrm{SFO}}{f_\mathrm{s}} T_\mathrm{s}\,, \tag{4.5}$$

where δ is the relative sampling clock error. The approximation $\delta \approx f_\mathrm{SFO}/f_\mathrm{s}$ considers the typically very small δ [109].

The erroneous sampled baseband Rx signal alters the fast-time/slow-time matrix from (2.21) to

$$\mathcal{D}_{n,m} = y_\mathrm{BB}\Big((n + mn_\mathrm{b}N)\,(T_\mathrm{s} + \Delta T_\mathrm{s})\Big)\,, \tag{4.6}$$

where n_b is the oversampling factor defined in 2.20. This leads to a stretching or compression of each sequence in time domain, as schematized in Fig. 4.7. Including CFO and the phase error term from (2.16) as well as SFO, the range matrix defined in (2.22) changes to

$$\begin{aligned}\mathcal{I}^\mathrm{R}_{n,m} = &\underbrace{\mathrm{e}^{\mathrm{j}2\pi m n_\mathrm{b} N f_\mathrm{CFO}\left(T_\mathrm{s}+\Delta T_\mathrm{s}\right)}}_{\text{CFO}} \underbrace{\mathrm{e}^{\mathrm{j}\phi_\mathrm{err}\left(\left(n+mn_\mathrm{b}N\right)\left(T_\mathrm{s}+\Delta T_\mathrm{s}\right)\right)}}_{\text{phase noise \& phase offset}} \\ &\times \sum_{k=1}^{N_\mathrm{T}} \underbrace{\mathrm{e}^{\mathrm{j}2\pi f_{\mathrm{d},k} m n_\mathrm{b} N\left(T_\mathrm{s}+\Delta T_\mathrm{s}\right)}}_{\text{vel. est.}} \underbrace{\mathrm{e}^{-\mathrm{j}2\pi f_\mathrm{Tx}\tau^\mathrm{R}_k}}_{\text{DoA est.}} \\ &\underbrace{\times \sum_{l=0}^{n_\mathrm{b}N-1} x_\mathrm{BB}\Big((l + mn_\mathrm{b}N)\,(T_\mathrm{s} + \Delta T_\mathrm{s}) - \tau^\mathrm{R}_k\Big)\, x^*_\mathrm{seq}\left((l+n)\,T_\mathrm{s}\right)}_{\text{autocorrelation for range estimation}}\,.\end{aligned} \tag{4.7}$$

The fast-time Doppler and fast-time CFO are neglected for the sake of simplicity.

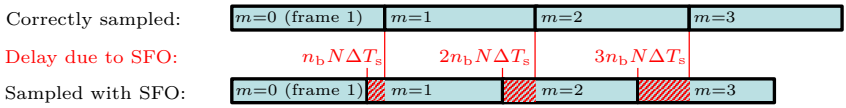

Fig. 4.7: Time shift of the different sequences, exemplarily depicted for $\Delta T_\mathrm{s}<0$.

Nevertheless, both affect the autocorrelation in the same manner by decreasing PNR and increasing sidelobes [46].

The SFO affects the autocorrelation in two ways: First, by manipulating the sample time $l\,(T_\mathrm{s}+\Delta T_\mathrm{s})$ within each sequence frame of $x_\mathrm{BB}(t)$. This results in a stretching or compression of the sequence, causing a smeared range peak within every correlation. Since the overall stretching/compression results in a sequence length error of $\Delta T = n_\mathrm{b} N \Delta T_\mathrm{s}$, the peaks after range correlation are smeared to a width of

$$\Delta \tilde{R}_\mathrm{single} = \left| n_\mathrm{b} N \Delta T_\mathrm{s} \frac{c_0}{2} \right| . \tag{4.8}$$

Executing the entire *Rv*-evaluation, this effect however is negligible as it is by far exceeded by the second effect: The time shift of each correlation frame caused by the wrong assumed duration of each frame due to the SFO. This is due the term $m\, n_\mathrm{b} N\,(T_\mathrm{s}+\Delta T_\mathrm{s})$, which results in a time shift increasing with each sequence, as depicted in Fig. 4.7. In the range matrix $\boldsymbol{\mathcal{I}}^\mathrm{R}[n,m]$, for every column m the range shift increases by

$$\Delta R_m = m\, n_\mathrm{b} N \Delta T_\mathrm{s} \frac{c_0}{2}. \tag{4.9}$$

This effect is visible in the range matrix as shown in Fig. 4.8 (a), presenting a measurement with a SFO of $f_\mathrm{SFO}\approx -78\,\mathrm{kHz}$: the range linearly drifts along the sequences, resulting in a ramp. After the Doppler FFT, the ramp is compressed into one large smeared peak of width

$$\Delta \tilde{R}_\mathrm{total} = \left| m n_\mathrm{b} N \Delta T_\mathrm{s} \frac{c_0}{2} \right| \tag{4.10}$$

as shown in Fig. 4.8 (b). Here, the peak is smeared to a range width of 1.2 m.

Additionally, the peak is smeared in velocity direction, resulting from the same effect. With the range drifting over the sequences, the velocity compression

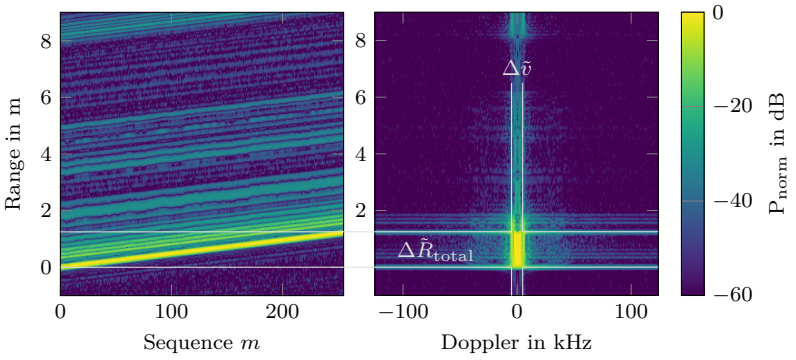

(a) Range matrix $\boldsymbol{\mathcal{I}}^{\mathrm{R}}$. **(b)** *Rv* image.

Fig. 4.8: Measurement result using uncoupled DAC/ADC. The scenario includes a static corner reflector at R=4.3 m in an anechoic chamber; The LOs are low-frequency coupled to guarantee that the errors observed stem from SFO only. Adapted from [45], CC BY 4.0 https://creativecommons.org/licenses/by/4.0/.

via the FFT is not based on a whole row of $\boldsymbol{\mathcal{I}}^{\mathrm{R}}$ with signal power, but only on the cells where the respective row intersects the range ramp. As a consequence, the velocity resolution is reduced to

$$\Delta\tilde{v} = \frac{\Delta\tilde{R}_{\text{total}} + \Delta R}{\Delta R}\Delta v\,, \tag{4.11}$$

as also shown in Fig. 4.8 (b).

While the aforementioned errors are caused within the range correlation, the Doppler FFT is also affected by the SFO. Due to the additional timing error ΔT_{s} from (4.5), the velocity estimation term from (4.7) equals

$$\mathrm{e}^{\mathrm{j}2\pi f_{\mathrm{d},k} m n_{\mathrm{b}} N \left(T_{\mathrm{s}}+\Delta T_{\mathrm{s}}\right)} = \mathrm{e}^{j2\pi f_{\mathrm{d},k} m\, n_{\mathrm{b}} N T_{\mathrm{s}}(1+\delta)} \tag{4.12}$$

leading to an offset in the estimated velocity of $v_{\mathrm{err,SFO}} = \delta \cdot f_{\mathrm{d}}$. However, due to the very small δ, this is negligible, as is the case with the CFO term from (4.7), which is also affected by the timing error.

4.3 Timing Recovery

In order to correct the sampling and thus align the timing of a bistatic signal at the Rx, a two-step procedure is proposed. For the first step, the Rx sample frequency $\tilde{f}_\mathrm{s}$ is estimated, which, in accordance with the employed signal model, includes the SFO. In a second step, the Rx signal is resampled to match the expected Tx sample rate f_s.

To detect $\tilde{f}_\mathrm{s}{=}f_\mathrm{s}{-}f_\mathrm{SFO}$ in the first step, a square timing recovery [110] is used. At first, the signal

$$\tilde{x}_\mathrm{timing}[n] = \left|\tilde{x}_\mathrm{Rx}[n] * h[n]\right|^2 \tag{4.13}$$

is computed by means of squaring the absolute value of the miss-sampled baseband Rx signal $\tilde{x}_\mathrm{Rx}[n]$ after applying a matched filter. The latter is implemented as a convolution $(*)$ with the pulse filter $h[n]$. The actual Rx code rate

$$\tilde{R}_\mathrm{c} \approx R_\mathrm{c} + \frac{f_\mathrm{SFO}}{n_\mathrm{b}} \tag{4.14}$$

then is a spectral component of $\tilde{x}_\mathrm{timing}[n]$. It can be calculated based on its spectrum $\tilde{X}_\mathrm{timing}[n]{=}\mathrm{FFT}\left(\tilde{x}_\mathrm{timing}[n]\right)$ by extracting the frequency with maximum power in a defined region around the expected coderate R_c. Based on $\tilde{R}_\mathrm{c}$, the actual Rx sample rate $\tilde{f}_\mathrm{s}$ is then calculated as

$$\tilde{f}_\mathrm{s} = f_\mathrm{s}\frac{R_\mathrm{c}}{\tilde{R}_\mathrm{c}}. \tag{4.15}$$

Since typical $|\Delta T_\mathrm{s}|{\ll}T_\mathrm{s}$ holds, a resampling algorithm is chosen that can handle resample factors $f_\mathrm{s}/\tilde{f}_\mathrm{s}$ close to one. This is the Farrow-filter-based resample algorithm presented in [111].

To verify the proposed timing recovery, it is applied to the same measurement which already had been shown in Fig. 4.8. Fig. 4.9 shows the spectrum $\tilde{X}_\mathrm{timing}[n]$ in the region of $R_\mathrm{c}{\pm}300\,\mathrm{kHz}$. A clear peak is visible, indicating $\tilde{R}_\mathrm{c}{=}R_\mathrm{c}{-}7.8\,\mathrm{kHz}$. According to (4.14), the SFO equals $f_\mathrm{SFO}{\approx}{-}78\,\mathrm{kHz}$ since $n_\mathrm{b}{=}10$. After detecting $\tilde{f}_\mathrm{s}$, it is corrected by means of a resampling by factor $f_\mathrm{s}/\tilde{f}_\mathrm{s}$. The result is shown in Fig. 4.10. Compared to Fig. 4.8 (a), the range slope is corrected in 4.10 (a), showing that the error due to the SFO induced range migration is suppressed. Consequently, in Fig. 4.10 (b) sharp peaks are visible for the RL as well as the corner reflector, demonstrating the good performance of the timing recovery.

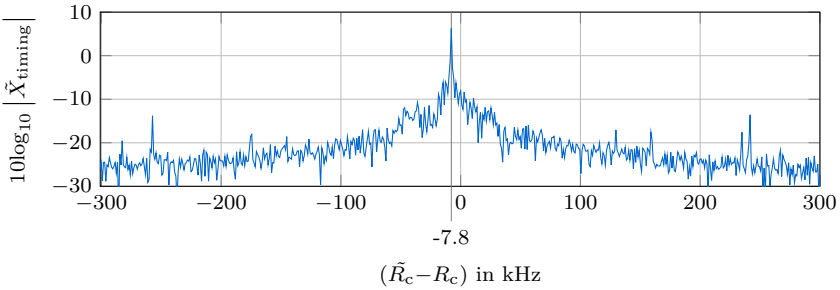

Fig. 4.9: Spectrum of $\tilde{x}_{\text{timing}}[n]$ as used for the estimation of $\tilde{R}_{\text{c}}$. Adapted from [45], CC BY 4.0 https://creativecommons.org/licenses/by/4.0/.

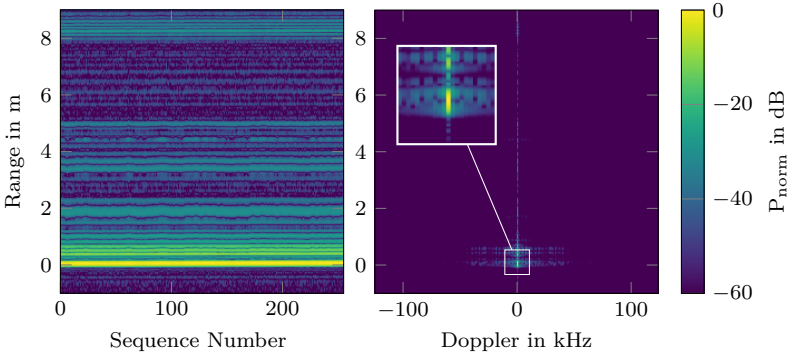

(a) Range matrix $\mathcal{I}^{\text{R}}$.

(b) *Rv* image.

Fig. 4.10: Measurement result using uncoupled DAC/ADC evaluated with timing recovery. The scenario includes a static corner reflector at R=4.3 m in an anechoic chamber; The LOs are low-frequency coupled to guarantee that the remaining error stems from SFO only. Adapted from [45], CC BY 4.0 https://creativecommons.org/licenses/by/4.0/.

4.4 Carrier Recovery

With the timing recovery presented in the previous section, the SFO can be mitigated. Nevertheless, the errors caused by CFO and phase noise remain and affect the *Rv* image as described in Section 4.2. Therefore, a new method for carrier reconstruction in PMCW radar networks is presented. It allows for coherent downconversion by digitally reconstructing an IF carrier. Therefore, the first step at Rx is to downconvert the signal, not to baseband, but onto the IF carrier $s_{\mathrm{IF}}(t)$. The IF carrier consequently equals the product of the delayed Tx carrier and the Rx carrier from (2.2) and (2.9), respectively, as

$$s_{\mathrm{IF}}(t) = s_{\mathrm{Tx}}(t-\tau_0)\, s_{\mathrm{Rx}}(t) = \mathrm{e}^{\mathrm{j}2\pi f_{\mathrm{IF}} t} \mathrm{e}^{\mathrm{j}\phi_{\mathrm{err}}(t)}\,. \tag{4.16}$$

Note that here only the dominant path with index 0 and ToF τ_0 is considered. This IF carrier includes CFO and thus has the frequency

$$f_{\mathrm{IF}} = f_{\mathrm{IF,expected}} + f_{\mathrm{CFO}}\,, \tag{4.17}$$

Its phase term $\phi_{\mathrm{err}}(t)$ from (4.16) includes phase noise, phase offsets, and phase drifts of the LOs. After downconversion to IF, the signal is digitized.

Still, it is not possible to distinguish between the carrier and the baseband signal, i.e., the BPSK sequences. The aim of the carrier recovery proposed in this section is therefore to separate the carrier signal from the modulation. In this way, an intradyne coherent downconversion to baseband in the digital domain becomes available. Considering a BPSK code sequence $x_{\mathrm{seq}}(t) \in \{-1, 1\} \forall t \in [0, T)$, the sequence can be eliminated by squaring as $(x_{\mathrm{seq}}(t))^2 = 1$. Consequently, the IF carrier is recovered by squaring the IF signal:

$$\left(x_{\mathrm{seq}}(t-\tau_0)\, s_{\mathrm{IF}}(t)\right)^2 = \mathrm{e}^{\mathrm{j}4\pi f_{\mathrm{IF}} t} \mathrm{e}^{\mathrm{j}2\phi_{\mathrm{err}}(t)}\,. \tag{4.18}$$

In this way, the IF carrier is recovered, including CFO, phase noise, and phase offset; however, all terms are squared. This strategy is based on the so-called squaring loop [107], which in the following is adapted to the PMCW radar.

4.4.1 Squaring Loop Carrier Recovery for PMCW Radars

The proposed squaring-loop carrier recovery for PMCW radars is schematized in Fig. 4.11. After upsampling and squaring, the non-squared IF carrier is extracted

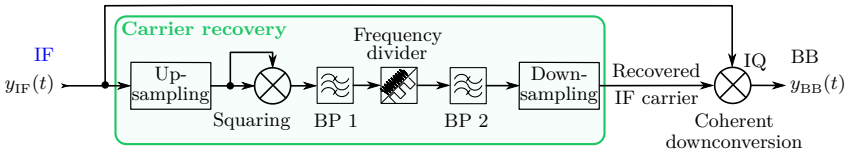

Fig. 4.11: Squaring-loop carrier recovery concept. Adapted from [45], CC BY 4.0 https://creativecommons.org/licenses/by/4.0/.

by means of a frequency divider and bandpass filters. Afterwards, the Rx signal is downconverted from IF to baseband using the recovered carrier, mitigating CFO, phase offsets, and phase noise. This concept assumes a dominant path in the Rx signal. In radar applications, however, typically multiple reflections and thus multiple signal paths are present. Therefore, one path significantly stronger than all the other ones is necessary, which is dominant when recovering the carrier. This strong path is called RL in the following, and is denoted with index 0. Depending on the network setup, it either refers to a LoS path between Tx and Rx, or a mutual coupling between the Tx and Rx antenna. In both scenarios, the RL leads to an IF Rx signal of

$$\begin{aligned} y_{\mathrm{IF}}(t) = & \underbrace{s_{\mathrm{IF}}(t)\, A_0 x_{\mathrm{BB}}(t-\tau_0)\, \mathrm{e}^{\mathrm{j}2\pi f_{\mathrm{d},0} t} \mathrm{e}^{-j2\pi f_{\mathrm{Tx}} \tau_k^{\mathrm{R}}}}_{= y_0(t)} \\ & \underbrace{+ s_{\mathrm{IF}}(t) \sum_{k=1}^{N_{\mathrm{T}}} A_k x_{\mathrm{BB}}\left(t-\tau_k^{\mathrm{R}}\right) \mathrm{e}^{\mathrm{j}2\pi f_{\mathrm{d},k} t} \mathrm{e}^{-j2\pi f_{\mathrm{Tx}} \tau_k^{\mathrm{R}}} + n(t)}_{= n_{\mathrm{cr}}(t)}, \end{aligned} \tag{4.19}$$

which is a superposition of the RL signal $y_0(t)$, the target responses, and additional white Gaussian noise (AWGN) denoted as $n(t)$. From a carrier recovery point of view, both the target responses and the AWGN can be considered as noise or interference. As denoted in (4.19), both are therefore combined to the variable $n_{\mathrm{cr}}(t)$. According to [106, p. 226], for a squaring loop to work a signal-to-noise ratio (SNR) of 6 dB is required. In case of the radar network, this must be satisfied for the relation between $y_0(t)$ and $n_{\mathrm{cr}}(t)$, resulting in the condition

$$y_0(t) > 2n_{\mathrm{cr}}(t)\ , \qquad 0 \leq t < T_{\mathrm{obs}}\,. \tag{4.20}$$

Since $n_{\mathrm{cr}}(t)$ is based on the superposition of all signals reflected from the different targets, condition (4.20) depends on amplitude and phase of each of the reflected signals. As this makes an estimation of the necessary RL power difficult, a worst case condition can be derived by assuming constructive interference of all signals. Based on the RL amplitude A_0 and the target response amplitudes A_k from (4.19) as well as the noise power P_{n} of the AWGN $n\,(t)$, this leads to

$$|A_0| > 2\left(\sum_{k=1}^{N_{\mathrm{T}}} |A_k| + \sqrt{P_{\mathrm{n}}}\right)\,. \tag{4.21}$$

As (4.21) assumes purely constructive summation, violating it does not inevitably affect the carrier recovery. Instead, it can be seen as a matter of reliability, with a higher RL power back-off leading to a more reliable carrier recovery. However, while a strong RL is preferable for carrier recovery, it also affects other parts of the Rx signal chain including radar hardware and signal processing. First, in the range estimation, the dynamic of the autocorrelation, i.e., the level of the sidelobes, is determined by the strongest channel response received, hence by the RL. Second, the hardware of the Rx must be designed to handle the power of the RL without the signal being significantly affected by non-linear behavior. In conclusion, a high RL power affects the dynamic range of the radar. This leads to a trade-off, where the expected target scenarios, the Rx hardware, the required dynamic range, and the required reliability have to be considered.

Assuming a sufficiently strong RL, this signal in the next step is used for the carrier recovery. As shown in Fig. 4.11, after a downconversion of the Rx signal to IF and upsampling, the code is removed by squaring the IF signal. For the sake of simplicity, the signals are notated as time continuous in the following. Initially considering an ideal carrier recovery based only on the RL part $y_0(t)$ of the signal $y_{\mathrm{IF}}\,(t)$, the result of the squaring is

$$\begin{aligned} y_0^2(t) &= s_{\mathrm{IF}}^2(t)\, A_0^2 \underbrace{x_{\mathrm{BB}}^2\,(t-\tau_0)}_{=1} \mathrm{e}^{j4\pi f_{\mathrm{d},0} t} \mathrm{e}^{-j4\pi f_{\mathrm{Tx}}\tau_0} \\ &= \mathrm{e}^{\mathrm{j}4\pi(f_{\mathrm{IF}}+f_{\mathrm{d},0})t} \mathrm{e}^{\mathrm{j}2\phi_{\mathrm{err}}(t)} \mathrm{e}^{-j4\pi f_{\mathrm{Tx}}\tau_0}\,. \end{aligned} \tag{4.22}$$

Ideally, the BPSK code is completely mitigated, while the carrier is squared, including the doubled SFO and phase noise. However, (4.22) also includes Doppler and path-length-dependent phase offset of the RL. While in most network scenarios the Doppler equals zero, the phase term $4\pi f_{\mathrm{Tx}}\tau_0$ shows the influence of the RL on the phase of the recovered carrier.

Considering the full IF signal $y_{\mathrm{IF}}(t)$ from (4.19), including also the influence of the noise and the targets, the resulting non-ideal squaring leads to

$$y_{\mathrm{IF}}^2(t) = \underbrace{y_0^2(t)}_{\text{I.}} + \underbrace{2y_0(t)\,n_{\mathrm{cr}}(t)}_{\text{II.}} + \underbrace{n_{\mathrm{cr}}^2(t)}_{\text{III.}} . \tag{4.23}$$

It consists of three terms with different influence on the carrier recovery performance:

I. is the term from (4.22) used for the carrier recovery.

II. is an unwanted term interfering the carrier recovery. It consists of two parts

$$2y_0(t)\,n_{\mathrm{cr}}(t) = 2y_0(t)\,n(t) + 2y_0(t)\sum_{k=1}^{N_{\mathrm{T}}} A_k x_{\mathrm{BB}}\left(t-\tau_k^{\mathrm{R}}\right) \mathrm{e}^{j2\pi f_{\mathrm{d},k}t}\mathrm{e}^{-j2\pi f_{\mathrm{Tx}}\tau_k^{\mathrm{R}}} , \tag{4.24}$$

where the first summand is the product of thermal noise and the RL signal. It corresponds to an AWGN term, and is dominant compared to the AWGN caused by III in (4.23). The second summand is the product of the target responses and the RL signal. It affects the carrier recovery differently, as in contrast to (4.22), $x_{\mathrm{BB}}(t-\tau_0)\times x_{\mathrm{BB}}\left(t-\tau_k^{\mathrm{R}}\right)\neq 1$. Hence, code residues are created, limiting the carrier recovery performance.

III. corresponds to another squared IF signal, thus, it causes an additional carrier to be recovered based on one of the targets. Being based on a different path length as the RL, the additional carrier can affect the phases of the target peaks after carrier recovery. Furthermore, it can yield ghost targets, since targets with $f_{\mathrm{d},k} \neq 0\,\mathrm{Hz}$ generate additional carrier components shifted by $f_{\mathrm{d},k}$. Both effects are limited by the high attenuation of A_k compared to A_0 (see (4.20) and (4.21)) and are further decreased by both the squaring and the frequency divider.

After squaring, a bandpass filter (BP) is applied to reduce higher harmonics, thermal noise, and code residues. Its passband is centered at $2f_{\mathrm{IF,expected}}$ and must cover the squared carrier at $2f_{\mathrm{IF}}$, including the CFO and the significant phase noise. On the one hand, the code residues are caused by the term II from (4.23). On the other hand, code residues are also caused by bandwidth limitations of the radar system: (4.18) assumes sequences with an ideal rectangular pulse filter $h(t)$ from (2.18), which would result in infinite bandwidth and thus in reality is approximated.

To extract the carrier from the squared IF signal, as shown in Fig. 4.11 a frequency divider is employed. This frequency divider consists of two steps: First, the squared and filtered signal is converted to a square wave using a hysteresis. The phase noise is still included as edge jitter. In the second step, the square wave's frequency is divided by choosing every second edge, creating a square wave at f_{IF}. After the frequency divider, a second BP is implemented, with a passband centered at $f_{\mathrm{IF,expected}}$. However, to successfully implement this frequency divider, a sufficient high sample frequency is necessary to allow for a proper sampling of the square wave at $2f_{\mathrm{IF}}$. This is ensured by the initial upsampling of signal before the carrier recovery, followed by a downsampling after the carrier is recovered, as visible in Fig. 4.11.

4.4.2 Carrier Recovery Performance

In the following, the performance of the carrier recovery is thoroughly analyzed using simulations. First, the influence of the ratio between IF frequency and coderate on the carrier recovery performance is examined. This enables the choice of a proper IF frequency in accordance with hardware restrictions. Second, the carrier recovery is verified in a scenario including multiple targets. Third, the phase offset correction achieved by the carrier recovery is statistically evaluated. If not otherwise stated, the carrier recovery parameters listed in Tab. 4.2 are used.

IF Frequency

The choice of the IF frequency is crucial for a well-performing carrier recovery. To analyze its influence, systematic simulations are performed using IF frequencies ranging from $0.1R_{\mathrm{c}}$=100 MHz to $1.7R_{\mathrm{c}}$=1.7 GHz in steps of 10 MHz. For each IF

Tab. 4.2: Carrier recovery parameters.

	Simulations	Measurements
IF frequency	$1.1R_c = 1.1\,\text{GHz}$	$1.1R_c = 1.1\,\text{GHz}$
Sample rate (upsampled)	20.0 GHz	20.0 GHz
BP1 center frequency	2.2 GHz	2.2 GHz
BP1 passband BW	60.0 MHz	2.0 MHz
BP2 center frequency	1.1 GHz	1.1 GHz
BP2 passband BW	60.0 MHz	2.0 MHz

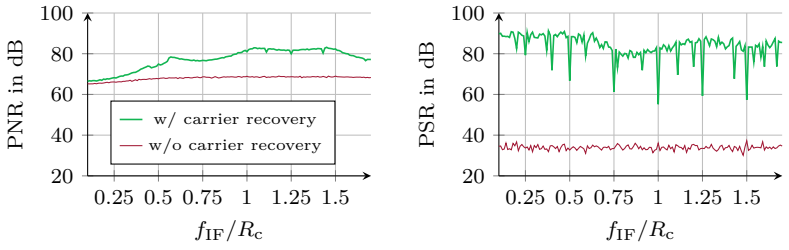

Fig. 4.12: Performance evaluation of the carrier recovery using different IF frequencies. The (a) PNR and (b) peak-to-skirt ratio (PSR) are shown for the evaluation with (—) and without (—) carrier recovery, and every data point equals the mean value of ten simulations. From [45], CC BY 4.0 https://creativecommons.org/licenses/by/4.0/.

frequency, 10 simulations are performed, using a scenario with the RL simulated as target at 1 m as the only target response in the Rx signal. The simulations are evaluated by calculating the PNR and the PSR of the RL peak. The PNR is determined by comparing the peak power with the maximum value in the histogram of all *Rv* cells, which represents the average noise power assuming a normal distribution. Since in both cases, with and without carrier recovery, the noise floor is dominated by the phase-noise-induced autocorrelation errors (see Section 4.2.2), this serves as one measure for the remaining phase noise. The PSR, on the other hand, refers to the available dynamics at the target range. It compares the peak power to the maximum value in the histogram of

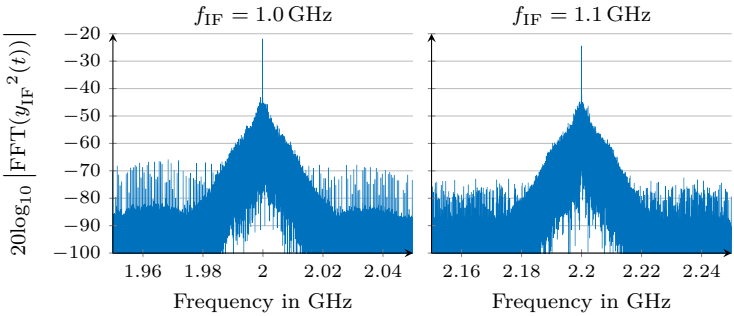

Fig. 4.13: Spectrum of ${y_{IF}}^2(t)$ based on simulations using different IF frequencies f_{IF}. From [45], CC BY 4.0 https://creativecommons.org/licenses/by/4.0/.

all *Rv* cells in the same range as the peak, i.e., in the corresponding velocity profile. Although the PSR does not capture all the characteristics of the velocity skirt, it can serve as a measure of the severity of the skirt, especially in cases where the skirt has a relatively flat profile, such as the phase noise used in the simulations.

The results of these simulations are summarized in Fig. 4.12. Fig. 4.12 (a) and Fig. 4.12 (b) show the obtained average PNR and PSR for different IF frequencies f_{IF}, respectively. Two important conclusions can be drawn from these simulations: First, it is not mandatory to have an $f_{IF} \geq R_c$. While, as shown in Fig. 4.12 (a), this still ensures the best performance, the degradation is small for $0.5R_c < f_{IF} < R_c$. This aspect can be exploited when a lower sample frequency is desired. The second finding can be observed in Fig. 4.12 (b). Notable notches appear if f_{IF} is a multiple of $0.25R_c$. These IF frequencies have in common that the phase of the IF carrier regularly aligns with the edges of the code sequence. These edges correspond to zero crossings and are likely to cause code residues in the recovered carrier. Regularly aligning them with the phase of the IF carrier increases the impact of the code residues and thus degrades carrier recovery performance. The difference in code residues is visible at the example shown in Fig. 4.13, where the spectrum after squaring is depicted for $f_{IF} = R_c = 1$ GHz and $f_{IF} = 1.1$ GHz, with higher code residues in the spectrum for $f_{IF} = 1$ GHz.

Multi-target Scenario

The next step is to verify the applicability of the carrier recovery in scenarios with multiple target responses in the Rx signal. Therefore, a scenario is simulated including an RL and five targets, both stationary as well as with different velocities. An overview over the target parameters is presented in Tab. 4.3. Fig. 4.14 shows a comparison of simulations with phase noise and CFO, evaluated both with and without carrier recovery, and a phase noise-free simulation for reference.

In Fig. 4.14 (a), which shows the Rv-image based on a simulation with phase noise but obtained without carrier recovery, an increased noise floor and a strong velocity skirt are visible. The PNR of the stationary target 2 is reduced to 49 dB compared to the PNR of 85 dB in the phase noise free simulation in Fig. 4.14 (c). Applying the carrier recovery increases this PNR by 16 dB to about 65 dB, as visible in Fig. 4.14 (b). In Fig. 4.14 (d), the velocity profiles at R=5 m extracted from the Rv images 4.14 (a) to 4.14 (c) are shown. Without carrier recovery, both, the velocity skirt as well as the velocity error due to CFO affect the velocity profile, hindering the detection of targets 2–5. In contrast, the performance with carrier recovery is similar to the phase noise-free simulation. The skirt is successfully suppressed and all four targets are distinguishable.

However, some ghost targets are visible in Fig. 4.14 (b). They are assumed to be caused by term III from (4.23) and are hence expected. Since ghost targets are caused by additional frequency components in the carrier, they occur at the same range as strong targets, and their power depends on the peak power of the target. Therefore, the strongest ghost targets are in the same range as the RL. They are suppressed by at least 33 dB compared to the peak from which they originate.

Phase Reconstruction

Using the carrier recovery, not only CFO and phase noise are mitigated. Also, the static phase offset between the LOs is reconstructed and mitigated by the coherent IQ downconversion. This is of special importance when using multiple PMCW radars for a network-based DoA estimation. However, there are several aspects to be noted. Due to the squaring, the unambiguous region of the reconstructed phase is reduced to 180°. Furthermore, as the carrier is

Tab. 4.3: Target parameters for the multi-target scenario simulation.

Target index	0 (RL)	1	2	3	4	5
R in m	1.0	3.0	5.0	5.0	5.0	5.0
v in $\frac{\text{m}}{\text{s}}$	0.0	9.5	0.0	-5.3	-19.0	-26.7
P_{norm} in dB	0.0	-16.9	-16.3	-37.0	-18.3	-27.6

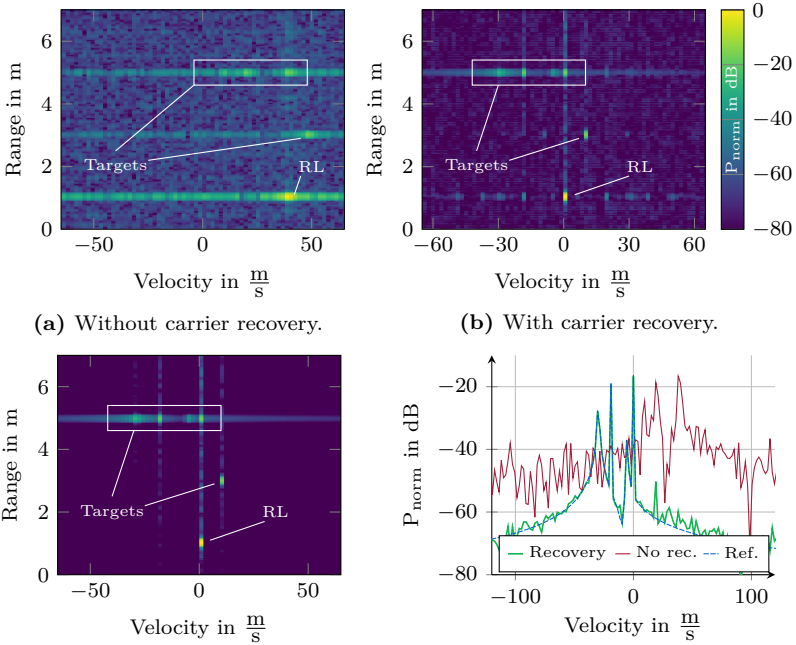

(a) Without carrier recovery.

(b) With carrier recovery.

(c) Phase noise and CFO free reference.

(d) Velocity profile extracted at R=5 m.

Fig. 4.14: Simulation results of the multi-target scenario from Tab. 4.3. In (b), the *Rv* image of a simulation including phase noise is shown, obtained with the proposed carrier recovery. The *Rv* images shown in (a) and (c) are evaluated without carrier recovery, however, the latter is based on a phase noise and CFO free simulation. Adapted from [45], CC BY 4.0 https://creativecommons.org/licenses/by/4.0/.

reconstructed based on the RL, the phase of the recovered carrier depends on the RL phase, which can be seen from (4.22). Therefore, a calibration of the RL as well as an algorithm to deal with the phase ambiguity is necessary.

Based on the multi-target scenario, the carrier recovery's ability to reconstruct phase offsets is evaluated. To do so, a total of 1000 simulations are performed, all using the scenario presented in Tab. 4.3. In each simulation, in addition to phase noise, a random CFO between 0 kHz and 20 kHz and a random static phase offset are applied. Then, the phase of target 2 is evaluated statistically. After correcting the result to the 180° unambiguous region, it is possible to estimate the phase offset within a standard deviation of 0.3°. This shows the independence of target phases from LO phase offsets after applying the carrier recovery.

4.5 Measurements

To verifiy the proposed timing and carrier recovery methods, the PMCW radar demonstrator presented in Section 4.1 is used. Instead of down converting the signal to baseband, as done in Section 4.2, here, different carrier frequencies are used at the LOs. While at Tx, the signal still is upconverted from baseband to RF, using f_{Tx}=76.8 GHz, on Rx side $f_{\mathrm{Rx}}=f_{\mathrm{Tx}}-f_{\mathrm{IF,expected}}$=75.7 GHz is used for downconversion.

Furthermore, the timing recovery and the carrier recovery are combined. An overview of the measurement setup and the signal processing steps is given in Fig. 4.15. First, the timing recovery is performed and the Rx is resampled to the correct sample frequency. Then, the carrier recovery is applied, followed by a digital IQ downconversion from IF to baseband. Finally, standard PMCW signal processing is performed as explained in Section 2.2.

4.5.1 Carrier Recovery

Initially, the carrier recovery itself is verified by measurements conducted within an anechoic chamber. For this, the DAC and ADC are coupled by a 10 MHz reference. The LOs on the other hand are uncoupled, resulting in a measurement affected by CFO and phase noise, but not by SFO. The measurement scenario includes an RL resulting from the mutual coupling of the antennas, which

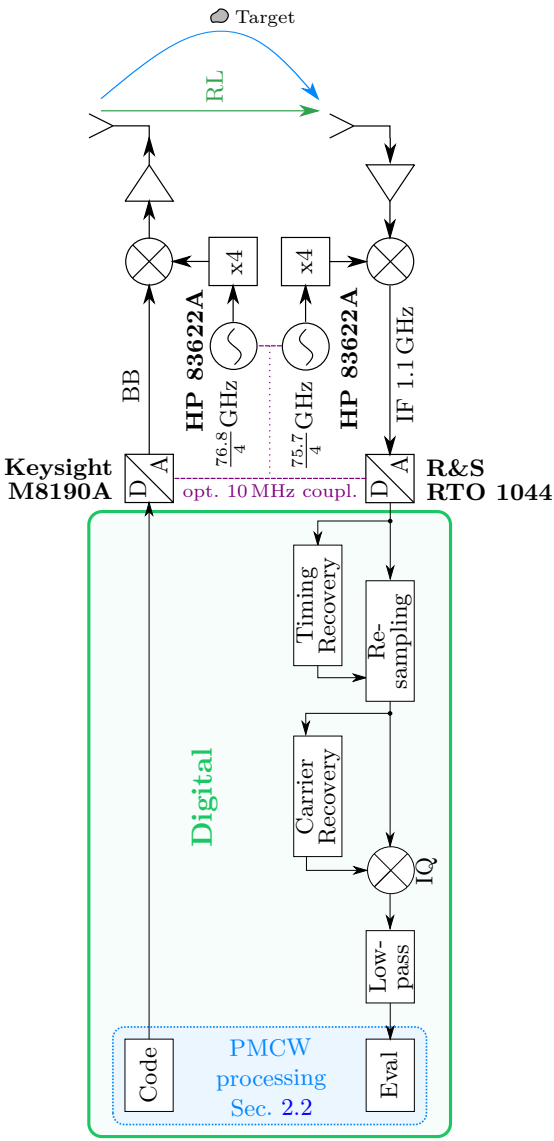

Fig. 4.15: Overview of the hardware system and digital signal processing, including the full synchronization via the proposed timing and carrier recovery. Adapted from [45], CC BY 4.0 https://creativecommons.org/licenses/by/4.0/.

are positioned as shown in Fig. 4.3, and a corner reflector at R=4.3 m. In the evaluation, the RL is used as R=0 m reference. Subsequently, all *Rv* matrices are shifted by the range of the RL.

In Fig. 4.16, a measurement with uncoupled LOs is evaluated with and without carrier recovery, and compared to a measurement with low-frequency coupled LOs. Without carrier recovery, the obtained *Rv* image in Fig. 4.16 (a) is heavily affected by a phase noise induced velocity skirt, and all targets are shifted by v_{err}=13.3 m/s. However, the PNR is only reduced by 2 dB, which may be due to the low bandwidth PSD of the LO phase noise. Furthermore, the range profiles shown in Fig. 4.16 (d) are all on par. The latter includes the range profile of the coupled measurement and is thus expected to be caused by hardware non-idealities of the measurement system. The *Rv* image shown in Fig. 4.16 (b) demonstrates that by performing the evaluation with carrier recovery, both the velocity skirt and the CFO-induced velocity error are well mitigated. This is particularly evident when comparing the velocity profiles of the corner reflector in Fig. 4.16 (c). The velocity skirt is nearly completely mitigated when applying the carrier recovery, achieving a better performance than by low-frequency coupling.

4.5.2 Full Synchronization

To verify the combined timing and carrier recovery, measurements are performed without any coupling of the measurement devices. In addition to the static corner reflector at R=4.3 m, the scenario includes a second corner reflector moved by hand at approximately the same distance.

Without the recovery steps, the *Rv* image is affected by SFO, CFO, and phase noise. The result is shown in Fig. 4.17 (a). Instead of peak-like targets, the SFO creates large rectangular areas in the *Rv* image spread across multiple resolution cells. At the same time, these areas are shifted by the CFO and smeared by a velocity skirt. Consequently, the measurement result, in the absence of the recovery steps, holds minimal practical value.

When applying both the proposed timing and carrier recovery for a synchronization of the uncoupled Tx/Rx pair, these effects are successfully mitigated. As visible in Fig. 4.17 (b), sharp peaks are achieved for each target, making all targets well detectable. This includes the stationary and moving corner

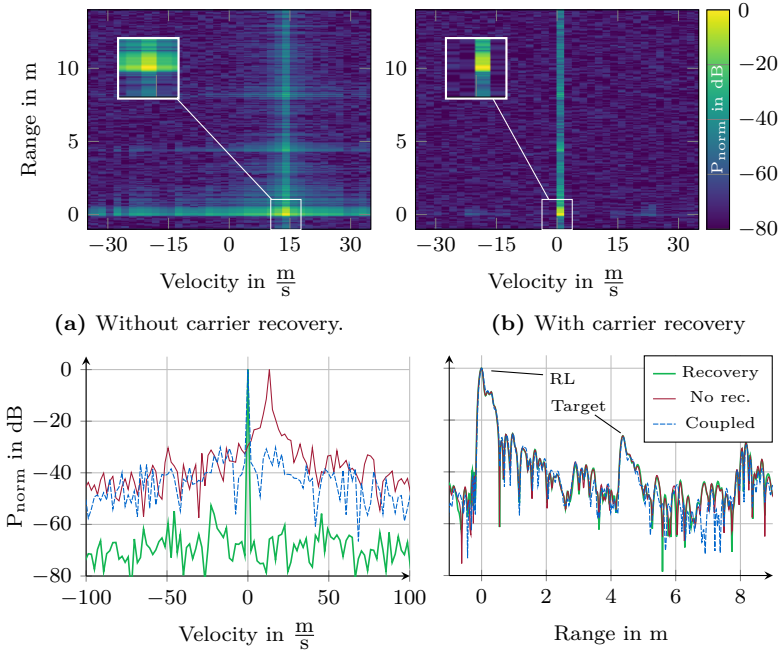

(a) Without carrier recovery.

(b) With carrier recovery

(c) Velocity profile at the RL.

(d) Range profile at v=0 or without recovery at v=v_{err}.

Fig. 4.16: Verification of the carrier recovery by a measurement with uncoupled LOs, but coupled DAC/ADC. The scenario includes the RL via the mutual coupling of the antennas as well as a corner reflector at 4.3 m in an anechoic chamber. Adapted from [45], CC BY 4.0 https://creativecommons.org/licenses/by/4.0/.

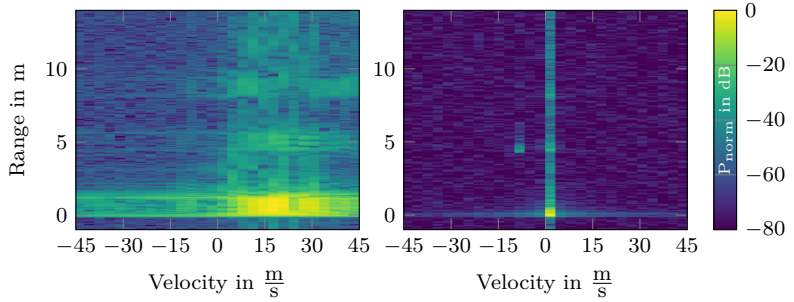

(a) Without synchronization.

(b) With full synchronization, i.e. carrier and timing recovery.

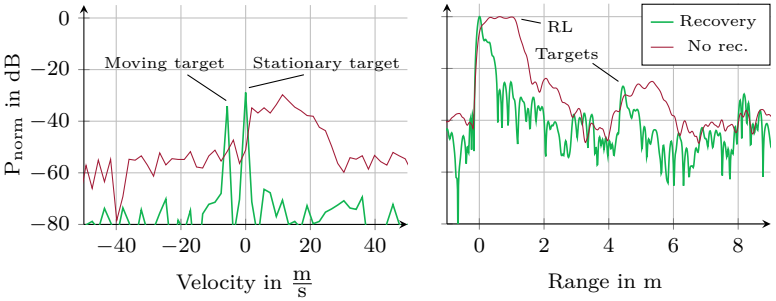

(c) Velocity profile at the targets' range (R=4.3 m).

(d) Range profile at v=0 or, without recovery, at v=v_{err}.

Fig. 4.17: Measurement results using an uncoupled Tx/Rx pair, evaluated with and without the proposed synchronization techniques. The scenario includes the RL via the mutual coupling of the antennas and two corner reflectors, one placed statically at 4.3 m and a second moved by hand at the same range. Adapted from [45], CC BY 4.0 https://creativecommons.org/licenses/by/4.0/.

reflectors at the same range, which are only separated by $3\Delta v$. Fig. 4.17 (c) shows the velocity profile at the range of these targets, validating that they are well distinguishable. Overall, this measurement shows the outstanding performance of the proposed recovery methods in mitigating the effects caused by the uncoupled Tx and Rx.

4.6 Discussion

To synchronize uncoupled radars in network by Rx side signal processing offers a very high flexibility in sensor node placement. Furthermore, no hardware adaptions have to be made to the radar. The single carrier signal of PMCW radars are promising for such a concept, since the signal structure has the channel information accessible without prior demodulation.

This chapter proposes synchronization techniques for PMCW radars. By means of the methods presented, the effects caused by uncoupled DAC/ADC pairs as well as uncoupled LOs are excellently mitigated. This is achieved using only Rx-side digital signal processing, taking advantage of the ability of digital radars to digitize the full bandwidth of the signal. The proposed techniques thereby include a timing recovery and a carrier recovery. The timing recovery enables to detect the SFO, thus allowing for a resampling of the Rx signal to mitigate SFO-induced effects on radar operation. The carrier recovery reconstructs the IF carrier, to which the signal is downconverted. Consequently, a digital intradyne downconversion from IF is performed, successfully mitigating CFO, phase noise, and phase offsets. However, this carrier recovery relies on a dominant signal received via an RL, representing a trade-off: A higher RL Rx power increases the reliability of the carrier recovery, but at the same time compromises the radar dynamics. The best strategy is therefore to adapt the RL to the expected measurement scenarios.

The measurements presented in this chapter verify the outstanding performance of the proposed synchronization techniques: Affected by SFO, CFO and phase noise, the bistatic measurements are barely useful without the recovery steps. Properly synchronizing by means of the timing and carrier recovery in contrast mitigates those impacts nearly entirely. While no radar network consisting of multiple MIMO radars has been presented yet, the proposed synchronization methods are a promising first step in this direction.

5 Network Concept II – OFDM Radar Network Using Symmetrical Path Repeater

Instead of realizing synchrony of uncoupled radar nodes through digital signal processing, as presented in Chapter 4, in this chapter a digital radar network is presented that is inherently synchronized—despite neither employing coupling nor a direct link. Key components are so-called repeaters, which act as additional sensor nodes in conjunction with a MIMO radar, implementing what is called a radar-repeater network. Equipped with a mixer and amplifiers, the repeaters retransmit the Rx signal with a frequency shift, providing an additional bistatic signal. Due to the low modulation frequency in the kHz range, no significant phase noise is added and a coherent bistatic signal evaluation is feasible. The MIMO radar receives the bistatic signals from the repeaters, and signal conversion between baseband and RF as well as signal generation and evaluation is performed only at this radar. Thus, only one sensor node requires a backend for signal evaluation, saving cost and reducing power consumption. The radar-repeater network has first been introduced for FMCW radars in [98], however, with FMCW radar the separation of mono- and bistatic signals is susceptible. In contrast, as shown in [73] by the author, the signal separation by low-frequency shifts fits seamlessly into the multicarrier structure of OFDM signals, allowing subcarrier interleaving within the network. Consequently, it enables the signals from different nodes to be orthogonal and thus separable.

This chapter introduces a radar network concept called symmetrical-path radar-repeater network (SymNW), based on one MIMO OFDM radar and several repeaters. The network topology is explained in detail in Section 5.1, followed by the signal model in Section 5.2. Afterward, OFDM signal processing and multiplexing adapted to the SymNW are proposed in Section 5.3 and Section 5.4, respectively. This allows to exploit the network for an high-resolution DoA estimation using the VNA as introduced in Section 5.5. Finally, the network is verified using measurements in Section 5.6.

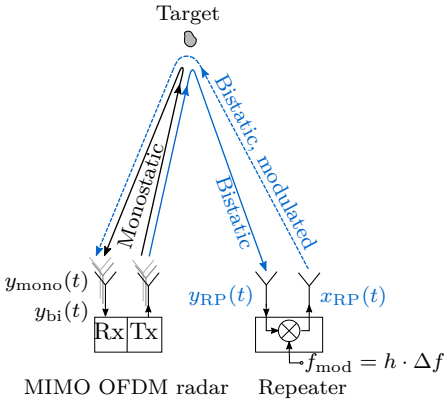

Fig. 5.1: Concept of the SymNW. Adapted from [73], CC BY 4.0 https://creativecommons.org/licenses/by/4.0/.

5.1 System and Measurement Setup

The proposed radar network comprises a single MIMO OFDM radar and two or more repeaters, as illustrated in Fig. 5.1. The repeaters receive a superposition of all Tx signals of the radar via reflections at the targets. These bistatic signals then are modulated, amplified, and retransmitted. After another reflection at the targets, they are captured by all radar Rx channels. Consequently, each bistatic signal contains the phase progression over all Tx and Rx antennas, plus the additional phase offset introduced by the position of the repeater. As discussed in detail in Section 5.5, this leads to an extended virtual array and thus to an improved DoA estimation.

Two types of custom-designed repeaters are employed for the measurements presented in this Chapter: A DSB and an SSB repeater. Both feature MMICs bonded on a Roger3003 PCB, and waveguides transitions to connect Rx and Tx antennas. UMS CHM2179b98F mixers shift the signal by a modulation frequency f_{mod}, and UMS CHA2080-98F variable gain amplifiers (VGAs) increase the repeater's Tx power. The DSB repeater illustrated in Fig. 5.2 (a) includes a single mixer for a DSB modulation, hence shifting the signal by $+f_{\mathrm{mod}}$ as

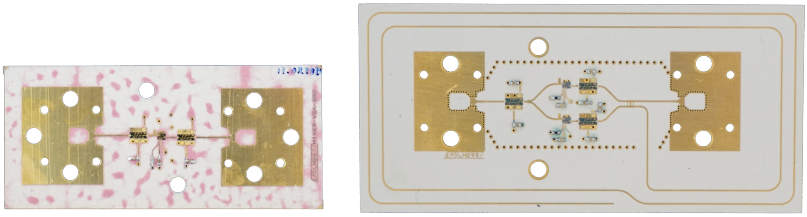

(a) DSB repeater. **(b)** SSB repeater.

Fig. 5.2: Photos of the repeater hardware.

well as $-f_{\mathrm{mod}}$, and has been used in [57], [73]. The SSB repeater features an image-rejection mixer build up by two mixers and three amplifiers, as shown in Fig. 5.2 (b), and has been characterized in detail by the author in [112].

5.2 Signal Model

To account for the bistatic signal of a SymNW, the signal model from Sections 2.1 and 2.3 must be adapted. For the sake of simplicity, the presented signal model w.l.o.g. considers the signal of one single repeater.

5.2.1 Repeater Receive and Transmit Signal

In accordance to the signal paths shown in Fig. 5.1, each repeater receives a superposition of the radar's Tx signals reflected at all N_{T} targets. The path radar–target, characterized by R and v, as well as the path target–repeater, characterized by R^{RP} and v^{RP}, are thereby distinctively considered. Consequently, in analogy to (2.8), a repeater's Rx signal corresponds to

$$y_{\mathrm{RP}}(t) = \sum_{k=1}^{N_{\mathrm{T}}} A_k \, x\left(t - \frac{R_k + R_k^{\mathrm{RP}}}{c_0}\right) \mathrm{e}^{-\mathrm{j}2\pi \frac{v_k + v_k^{\mathrm{RP}}}{c_0} f_{\mathrm{Tx}} t}, \tag{5.1}$$

with the bistatic ToF

$$\tau_k^{\mathrm{bi}} = \frac{R_k + R_k^{\mathrm{RP}}}{c_0} \tag{5.2}$$

and the bistatic Doppler frequency

$$f_{\mathrm{d},k}^{\mathrm{bi}} = -\left(v_k + v_k^{\mathrm{RP}}\right)\frac{f_{\mathrm{Tx}}}{\mathrm{c}_0}. \tag{5.3}$$

In correspondence to (2.28), the phase progression via the subcarriers induced by the bistatic ToF results in

$$\theta_k^{\mathrm{bi}}[n] = -2\pi f_n \tau_k^{\mathrm{bi}} = -2\pi f_n \frac{R_k + R_k^{\mathrm{RP}}}{\mathrm{c}_0}\,. \tag{5.4}$$

The significance of differences between R_k and R_k^{RP} as well as v_k and v_k^{RP} is contingent upon the geometry of the network. Considering radar networks as used in this work, the sensor nodes are placed close to each other to obtain a less sparse VNA. In this case $R_k \approx R_k^{\mathrm{RP}}$ and $v_k \approx v_k^{\mathrm{RP}}$ yields. On the contrary, if the nodes are placed further apart, the difference between v_k and v_k^{RP} can be exploited to provide vectorial velocity estimation [113], [114].

The repeaters' signal modulation capabilities are used to assure a proper multiplexing of the mono- and bistatic signals. This is done by subcarrier interleaving, i.e. FDM: each repeater shifts the signal by an integer number of subcarriers, leading to a modulation frequency of

$$f_{\mathrm{mod}} = h\Delta f, \qquad h \in \mathbb{Z} \setminus 0\,. \tag{5.5}$$

Additionally, the repeater introduces a ToF τ^{RP} between its Rx and Tx antenna, which can be calibrated for, as well as an amplitude alteration A_{RP}. In consequence, a repeater's Tx signal amounts to

$$x_{\mathrm{RP}}(t) = A_{\mathrm{RP}}\; y_{\mathrm{RP}}\left(t - \tau^{\mathrm{RP}}\right) \times \left(\underbrace{\mathrm{e}^{\mathrm{j}\left(2\pi h\Delta f t + \phi_{\mathrm{mod}}\right)}}_{=x_{\mathrm{mod}}(t)} + \underbrace{L_{\mathrm{IR}}\,\mathrm{e}^{-\mathrm{j}\left(2\pi h\Delta f t + \phi_{\mathrm{mod}}\right)}}_{=x_{\mathrm{mod,LSB}}(t)} \right), \tag{5.6}$$

where the sideband suppression is denoted as factor L_{IR}. While the conceptual idea of the repeater's signal modulation is to only shift the signal to another set of subcarriers, the modulation signal also introduces phase errors: First, at the start of the OFDM signal (t=0), the modulation signal includes the phase offset ϕ_{mod}. Without compensation, this affects the network-based DoA estimation.

Second, the modulation signal introduces a phase offset $\Delta\varphi_{\mathrm{mod}}(h)$ between to adjacent OFDM symbols, since its phase continuously rotates during each CP. Both are discussed in detail in Section 5.5.1 and Section 5.3.2, respectively, including mitigation methods.

5.2.2 Bistatic Receive Signal

After the signal is retransmitted by the repeater, it is reflected back to the radar by all targets within the channel, leading to the bistatic receive signal

$$y(t) = \sum_{l=1}^{N_{\mathrm{T}}} A_l \, x_{\mathrm{RP}}\left(t - \frac{R_l + R_l^{\mathrm{RP}}}{\mathrm{c}_0}\right) \mathrm{e}^{-\mathrm{j}2\pi \frac{v_l + v_l^{\mathrm{RP}}}{\mathrm{c}_0} f_{\mathrm{Tx}} t} . \tag{5.7}$$

corresponding to the repeater's Tx signal from (5.6) after traveling the channel a second time.

Combining (5.1), (5.6) and (5.7), it can be concluded that the radar receives a linear combination of signals reflected at the kth target on the way to the repeater, and at the lth target on the way back, with $k, l = 1, \ldots, N_{\mathrm{T}}$. In addition, the signal is shifted in frequency by h subcarriers through the repeater. Hence, the bistatic OFDM Rx matrix $\boldsymbol{\mathcal{D}}^{\mathrm{Rx,bi}}$ is defined analogously to (2.29) by its elements

$$\mathcal{D}_{n+h,m}^{\mathrm{Rx,bi}} = \mathcal{D}_{n,m}^{\mathrm{Tx}} \; A_{\mathrm{RP}} \underbrace{\mathrm{e}^{\mathrm{j}\phi_{\mathrm{mod}}} \mathrm{e}^{\mathrm{j}m\Delta\varphi_{\mathrm{mod}}(h)}}_{\substack{\text{modulation phase errors,} \\ \text{see Sections 5.5.1 and 5.3.2}}}$$
$$\times \sum_{k=1}^{N_{\mathrm{T}}} \sum_{l=1}^{N_{\mathrm{T}}} A_k A_l \underbrace{\mathrm{e}^{\mathrm{j}\left(\theta_k^{\mathrm{bi}}[n] + \theta_l^{\mathrm{bi}}[n+h]\right)}}_{\text{range estimation}} \underbrace{\mathrm{e}^{-\mathrm{j}2\pi f_{\mathrm{Tx}}\left(\tau_k^{\mathrm{bi}} + \tau_l^{\mathrm{bi}} + \tau^{\mathrm{RP}}\right)}}_{\text{DoA estimation}} \underbrace{\mathrm{e}^{\mathrm{j}2\pi\left(f_{\mathrm{d},k}^{\mathrm{bi}} + f_{\mathrm{d},l}^{\mathrm{bi}}\right) mT}}_{\text{velocity estimation}} . \tag{5.8}$$

This signal model can be extended to account for a radar network consisting of one radar and N_{RP} repeaters, each with its own modulation index h_u with $u \in \{1, \ldots, N_{\mathrm{RP}}\}$. At the radar Rx, then the superposition of the bistatic signals of all repeaters and the radar's monostatic signals is received, forming a combined network Rx matrix

$$\boldsymbol{\mathcal{D}}^{\mathrm{Rx,NW}} = \boldsymbol{\mathcal{D}}^{\mathrm{Rx}} + \sum_{u=1}^{N_{\mathrm{RP}}} \boldsymbol{\mathcal{D}}_u^{\mathrm{Rx,bi}} , \tag{5.9}$$

where for each uth repeater an Rx matrix $\boldsymbol{\mathcal{D}}_u^{\mathrm{Rx,bi}}$ as defined in (5.8) is included.

5.3 Bistatic Signal Processing

A comparison of the Rx matrices in (2.29) and (5.8) reveals that, while the fundamental concept of the conventional OFDM processing presented in Section 2.3 remains applicable for bistatic signal evaluation, an adaptation is necessary to account for the influences caused by the signal modulation within the repeater. In the following, the evaluation of the bistatic signal is explained in detail focusing on the steps in the processing chain which differ from conventional OFDM radar signal processing as explained in Section 2.3. This is accompanied by an overview presented in Fig. 5.3.

5.3.1 Demodulation

The first step of the demodulation is to compute the symbol domain Rx matrix $\boldsymbol{\mathcal{D}}^{\mathrm{Rx,NW}}$=DFT↾[$\boldsymbol{\mathcal{Y}}$] as described in Section 2.3.2. Afterward, the division matrix

$$\boldsymbol{\mathcal{D}}(h) = \boldsymbol{\mathcal{D}}^{\mathrm{Rx,NW}} \odot \left(\boldsymbol{\mathcal{D}}^{\mathrm{Sym}}(h)\right)^{*} \tag{5.10}$$

similar to (2.30) is computed. The symbol matrix

$$\boldsymbol{\mathcal{D}}^{\mathrm{Sym}}(h) = \mathrm{circshift}↾\left[\boldsymbol{\mathcal{D}}^{\mathrm{Tx}}, h\right] \tag{5.11}$$

takes into account the subcarrier shift of the repeaters by circularly shifting $\boldsymbol{\mathcal{D}}^{\mathrm{Tx}}$ by h subcarriers. $\boldsymbol{\mathcal{D}}(h{=}0)$ equals the monostatic division matrix from (2.30).

To ensure the separability of the mono- and bistatic signals, they must be orthogonal, which implies that

$$\boldsymbol{\mathcal{D}}_p^{\mathrm{Sym}}(h_u) \odot \boldsymbol{\mathcal{D}}_q^{\mathrm{Sym}}(h_w) = \mathbf{0}^{N,M}, \qquad \forall p,q \in \{1,\ldots,N_{\mathrm{Tx}}\} \wedge h_u \neq h_w, \tag{5.12}$$

h_u, h_w are modulation indices of a repeater or zero for the monostatic signal. The matrix $\mathbf{0}^{N,M}$ is defined as an all-zero matrix of dimension $N{\times}M$. While w.l.o.g. the different $\boldsymbol{\mathcal{D}}^{\mathrm{Tx}}$ of different Tx channels are not explicitly considered in this section, they are also designed to be inherently orthogonal through a proper multiplexing strategy. This will be detailed further on in this chapter.

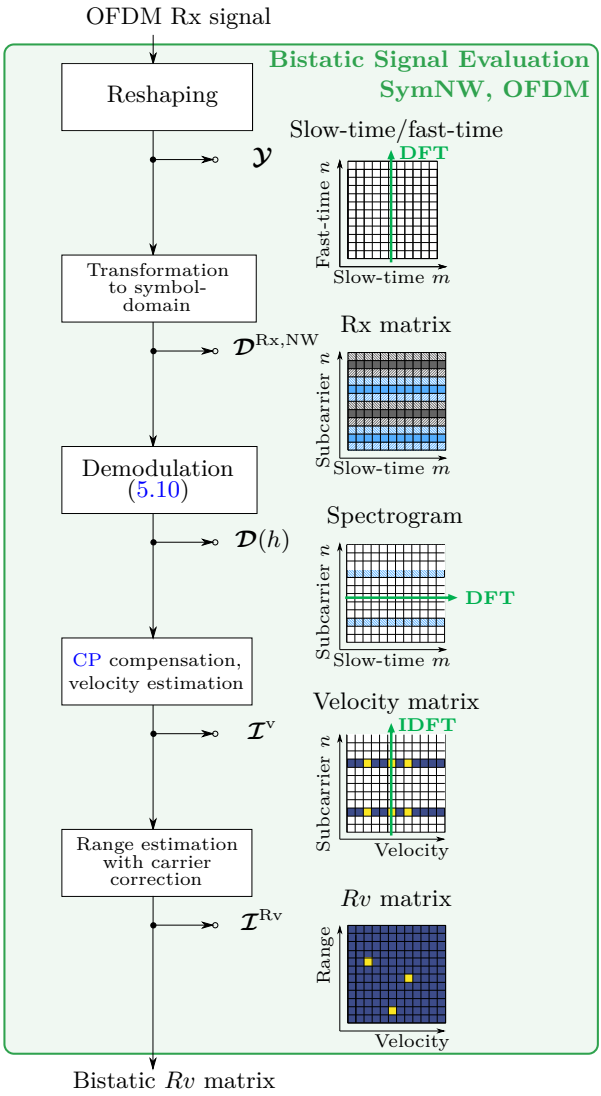

Fig. 5.3: Bistatic OFDM signal processing for a SymNW.

5.3.2 Cyclic Prefix Compensation & Velocity Estimation

The phase rotation of the repeater's modulation signal within each cyclic prefix results in a phase offset between adjacent OFDM symbols of

$$\Delta\varphi_{\mathrm{mod}}\left(h\right) = 2\pi f_{\mathrm{mod}} T_{\mathrm{CP}} = 2\pi h \frac{T_{\mathrm{CP}}}{T_{\mathrm{sym}}} \tag{5.13}$$

affecting $\boldsymbol{\mathcal{D}}^{\mathrm{Rx,bi}}$ as visible in (5.8). If not corrected, the velocity estimation is offset by

$$v_{\mathrm{err}}\left(h\right) = h \frac{T_{\mathrm{CP}}}{T_{\mathrm{sym}}} v^{\mathrm{ua}}\,. \tag{5.14}$$

Given the known parameters h and T_{CP}, $\Delta\varphi_{\mathrm{mod}}\left(h\right)$ can be corrected. This is achieved by employing a correction vector

$$\boldsymbol{\kappa}\left(h\right) = \left(\mathrm{e}^{-\mathrm{j}\Delta\varphi_{\mathrm{mod}}(h)},\ \mathrm{e}^{-2\mathrm{j}\Delta\varphi_{\mathrm{mod}}(h)},\ \ldots,\ \mathrm{e}^{-M\mathrm{j}\Delta\varphi_{\mathrm{mod}}(h)}\right)\,. \tag{5.15}$$

For a correction, each mth element of $\boldsymbol{\kappa}(h)$ must be multiplied with the mth column of $\boldsymbol{\mathcal{D}}(h)$. Combining this step with a velocity estimation analogous to (2.31), the velocity matrix is computed by

$$\boldsymbol{\mathcal{I}}^{\mathrm{v}} = \overrightarrow{\mathrm{DFT}}\left[\boldsymbol{\mathcal{D}}\left(h\right)\ \ \mathrm{diag}\left[\boldsymbol{\kappa}\left(h\right)\right]\right]\,, \tag{5.16}$$

where $\mathrm{diag}\left[\boldsymbol{\kappa}\left(h\right)\right]$ is the diagonal matrix containing the elements of $\boldsymbol{\kappa}\left(h\right)$.

5.3.3 Range Estimation

Due to the frequency shift introduced by the repeaters, prior adaptions are required before applying the range estimation as in (2.32). For the network-based DoA estimation proposed in this thesis, only signals resulting from reflections at the same target on the way to the repeater and on the return path are relevant, i.e., paths with $l{=}k$. Therefore, the following signal processing focuses on the correct evaluation of these so-called single-target (ST) signals. Investigating the range estimation term of (5.8), its phase

$$\theta_k^{\mathrm{bi}}\left[n\right] + \theta_k^{\mathrm{bi}}\left[n+h\right] \overset{(5.4)}{=\!=} -2\pi\tau_k^{\mathrm{bi}} 2 f_{n+h} + \underbrace{2\pi\tau_k^{\mathrm{bi}} h \Delta f}_{=\,\phi_{\mathrm{err}}} \tag{5.17}$$

consists of the phases $\theta_k^{\mathrm{bi}}[n]$ due to the path to the repeater and $\theta_k^{\mathrm{bi}}[n+h]$ due to the return path, both based on different subcarriers. The phase (5.17) alters from the phase expected on subcarrier $n{+}h$ by ϕ_{err}, which if unaddressed interferes network-based DoA estimation by introducing phase errors varying in dependence on the modulation index h. To compensate for the phase error, (5.17) must be evaluated not on the $(n{+}h)$th subcarrier, but on the $(n{+}0.5h)$th subcarrier. For even h, this adjustment is achieved by shifting $\boldsymbol{\mathcal{I}}^{\mathrm{v}}$ by $-0.5h$ subcarriers before performing the range estimation as in (2.32). In contrast, for odd h, a matrix $\widetilde{\boldsymbol{\mathcal{I}}}^{\mathrm{v}} \in \mathbb{C}^{2N \times M}$ with elements

$$\widetilde{\mathcal{I}}^{\mathrm{v}}_{\tilde{n},m} = \begin{cases} \mathcal{I}^{\mathrm{v}}_{0.5\tilde{n},m}, & \tilde{n} \text{ even} \\ 0, & \text{else,} \end{cases} \qquad \text{with } \tilde{n} = 0, 1, \ldots, 2N-1 \,, \tag{5.18}$$

is generated, twice the size of $\boldsymbol{\mathcal{I}}^{\mathrm{v}}$ and containing rows of zeros between the subcarriers. Then, $\widetilde{\boldsymbol{\mathcal{I}}}^{\mathrm{v}}$ is shifted by $-h$ before computing the *Rv*-matrix $\tilde{\boldsymbol{\mathcal{I}}}^{\mathrm{Rv}} \in \mathbb{C}^{2N \times M}$ via a column-wise IDFT↾. Since the empty rows in $\widetilde{\boldsymbol{\mathcal{I}}}^{\mathrm{v}}$ lead to a repetition of the *Rv* matrix, $\tilde{\boldsymbol{\mathcal{I}}}^{\mathrm{Rv}}$ is reduced to $\boldsymbol{\mathcal{I}}^{\mathrm{Rv}} \in \mathbb{C}^{N \times M}$ by taking the first N rows.

5.3.4 Interpretation of the Bistatic Range-Doppler Matrix

Examining the bistatic receive signal from (5.8) and the bistatic signal evaluation reveals that the bistatic *Rv* matrix varies in several aspects compared to its monostatic counterparts. As a result, the interpretation of the *Rv* matrix must be adapted to take into account the anticipated bistatic *Rv* peaks.

Each signal is specified by two reflections: one occurring on the path from the radar to the repeater and another on the return path. Since these reflections can occur on different targets, the bistatic signals inclining at the radar's Rx correspond to a linear combination of all targets. Basically, a distinction can be made between ST paths and multi-target (MT) paths. ST paths result from reflections on the same target twice, i.e., $l{=}k$, and generate the *Rv* peaks required for DoA estimation. These paths yield an peak in the *Rv* matrix at

$$\begin{aligned} R^{\mathrm{bi}}_{k,k} &= R_k + R^{\mathrm{RP}}_k &&= 2R_k + 2\Delta R^{\mathrm{bi}} \\ v^{\mathrm{bi}}_{k,k} &= v_k + v^{\mathrm{RP}}_k &&= 2v_k + 2\Delta v^{\mathrm{bi}}, \end{aligned} \tag{5.19}$$

where R_k and v_k are the monostatic range and velocity, respectively. The

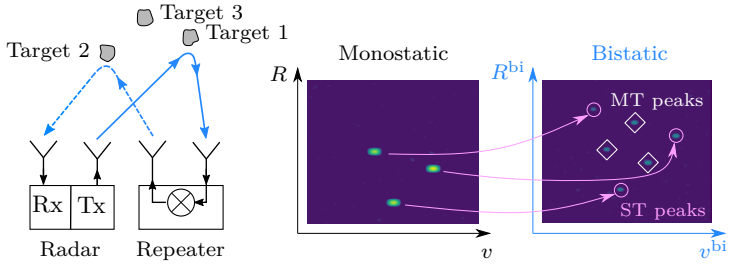

Fig. 5.4: Exemplary MT path and MT peaks.

summands ΔR^{bi} and Δv^{bi} account for the difference in range and velocity between radar–target and repeater–target, and may be exploited for a vectorial velocity estimation [114].

MT paths, as illustrated in the left graph of Fig. 5.4, are caused by signals reflected at different targets on the way there and back to the repeater. Considering a scenario with N_{T} targets, there are

$$N_{\mathrm{MT}} = N_{\mathrm{T}} \left(N_{\mathrm{T}} - 1 \right) \tag{5.20}$$

MT paths in total. Since paths with a reflection at the kth target on the way to the repeater and on the lth on the way back feature the same ToF and Doppler as the opposite path, with the first reflection at target l and the second at k, the MT paths result in $N_{\mathrm{MT}}/2$ MT peaks in the Rv image. Compared to the ST peaks, their range and velocity corresponds to a combination of both targets k and l as

$$\begin{aligned} R^{\mathrm{bi}}_{k,l} &= R^{\mathrm{bi}}_{l,k} = 0.5 R^{\mathrm{bi}}_{k,k} + 0.5 R^{\mathrm{bi}}_{l,l} \\ v^{\mathrm{bi}}_{k,l} &= v^{\mathrm{bi}}_{l,k} = 0.5 v^{\mathrm{bi}}_{k,k} + 0.5 v^{\mathrm{bi}}_{l,l}. \end{aligned} \tag{5.21}$$

In conclusion, for further processing such as a network-based DoA estimation, it is crucial to identify the ST peaks among the MT peaks. This may be achieved by an algorithm presented in [115] by the author and included in Appendix B, where the relations described in (5.19) and (5.21) are exploited for a proper peak classification.

To show the presence of these MT peaks, Fig. 5.5 depicts the measurement



(a) Measurement scenario.

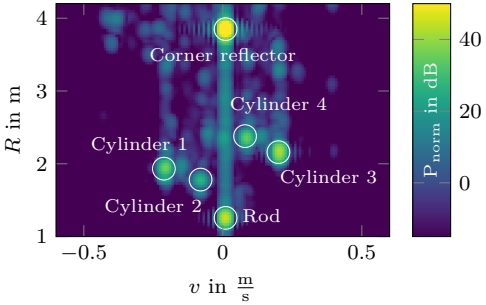

(b) Monostatic *Rv*-image.

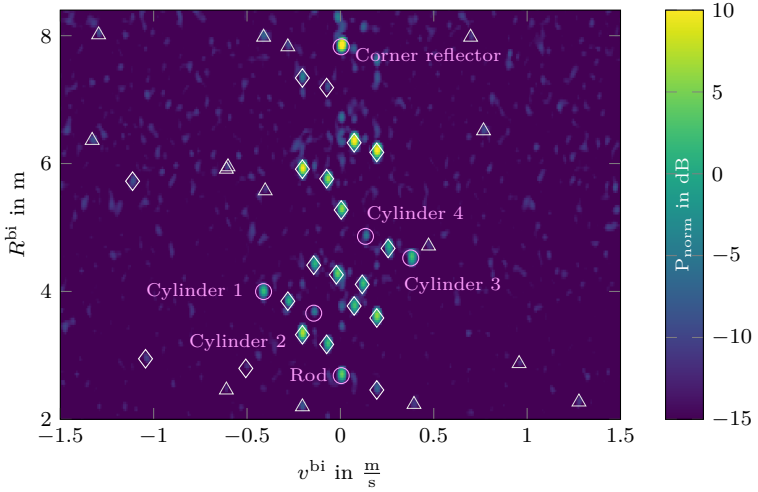

(c) Bistatic *Rv*-image including the peaks classified by algorithm B.2. (○: ST peak; ◊: MT peak; △: Unknown peak (clutter)).

Fig. 5.5: Mono- and bistatic measurement of a complex scenario including two static targets as well as four cylinders mounted on a rotating platform (a). The measurement is performed using a 77-GHz FMCW radar and the SSB repeater shown in Fig. 5.2 (b). (b) presents the monostatic *Rv* image, and (c) the bistatic *Rv* image. The latter includes the peaks as classified by algorithm B.2. Adapted from [115], © 2022 EUMA.

results of a complex scenario with four cylinders mounted on a rotating platform, a rod, and a corner reflector. The measurement is conducted using an FMCW radar operating at 77 GHz, due to the lack of an OFDM radar available with sufficient range resolution for such a scenario. However, the bistatic target characteristics as described in equations (5.19)–(5.21) do not depend on the radar signal modulation. As repeater, the SSB repeater described in Section 5.1 is used. Fig. 5.5 (b) shows the monostatic *Rv* image, including the six target peaks. In Fig. 5.5 (c), the evaluation of the bistatic signal is shown, additionally comprising the 15 MT peaks expected due to (5.20). However, it is shown that all ST peaks can be successfully classified based on the relations from (5.19) and (5.21) using the algorithms B.1 and B.2 in Appendix B.

5.4 Multiplexing

While the repeaters themselves only allow for frequency shifting of their respective signal, thus always using FDM, the flexibility of OFDM signal generation allows to multiplex the radar's Tx channels in both the time and the frequency domains. Thus, by altering $\boldsymbol{\mathcal{D}}^{\mathrm{Tx}}$, different multiplexing strategies are realized within the radar network, which first have been proposed in [57] by the author. This includes a combination of FDM and TDM, as well as a random approach combined with CS.

Frequency-Division Multiplexing

Assigning different subcarriers to different Tx channels allows for a straightforward implementation of FDM when using OFDM signals [116]. In a radar-repeater network, this is achieved by assigning a specific set of subcarriers to each radar Tx channel and leaving empty subcarriers in between for the repeaters to shift their bistatic signal onto. An exemplary FDM assignment is illustrated in Fig. 5.6 (a). However, using FDM, the signal of each Tx channel is sparse in subcarrier domain, leading to regular spacings in a distance of $\Delta n_{\mathrm{Tx}}^{\mathrm{FDM}}$:

$$\Delta n_{\mathrm{Tx}}^{\mathrm{FDM}} = N_{\mathrm{Tx}}\,(sN_{\mathrm{RP}} + 1) \;\text{ and }\; \Delta m_{\mathrm{Tx}}^{\mathrm{FDM}} = 1 \tag{5.22}$$

$\Delta m_{\mathrm{Tx}}^{\mathrm{FDM}}$ denotes the spacing in OFDM symbol domain. The sparsity depends on the number of radar Tx channels N_{Tx}, the number of repeaters N_{RP}, and

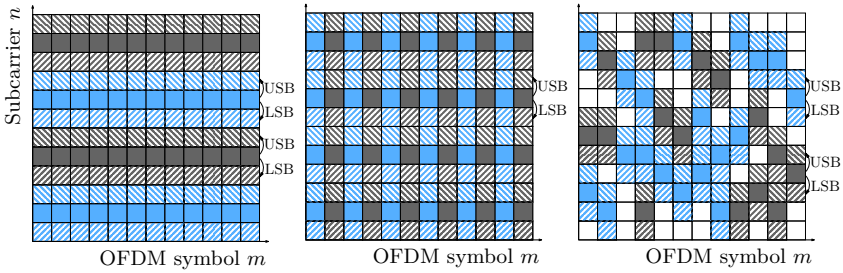

(a) FDM. **(b)** TFDM. **(c)** RFDM.

Fig. 5.6: Multiplexing strategies for OFDM-based SymNW, shown for the example of two radar Tx and one DSB repeater (Tx1: ■, Tx2: ■, unassigned: □). From [57], © 2021 IEEE.

the factor s which is s=1 for SSB and s=2 for DSB repeaters. This leads to an under-sampled division matrix $\boldsymbol{\mathcal{D}}$, affecting the range-estimation IDFT↑ and reducing the unambiguous range to $R^{\mathrm{ua}}_{\mathrm{NW}}{=}R^{\mathrm{ua}}/\Delta n_{\mathrm{Tx}}$.

Time- and Frequency-Division Multiplexing

To avoid the high loss in unambiguous range through applying FDM for both, radar and repeater nodes, time-and-frequency-division multiplexing (TFDM) uses a TDM approach for the radar Tx channels. All radar Tx are separated by transmitting within different OFDM symbols, i.e., time slots, while the repeaters still employ frequency modulation for FDM. This two-dimensional multiplexing is exemplarily shown in Fig. 5.6 (b). Thus, each Tx signal is also sparse in the OFDM symbol domain, with a regular spacing of Δm_{Tx} symbols, resulting in

$$\Delta n^{\mathrm{TFDM}}_{\mathrm{Tx}} = sN_{\mathrm{RP}} + 1 \text{ and } \Delta m^{\mathrm{TFDM}}_{\mathrm{Tx}} = N_{\mathrm{Tx}} \tag{5.23}$$

The unambiguous range R^{ua} is, compared to FDM, improved by factor N_{Tx}. In contrast, the unambiguous velocity is reduced to $v^{\mathrm{ua}}_{\mathrm{NW}}{=}v^{\mathrm{ua}}/\Delta m_{\mathrm{Tx}}$. Since the maximum velocity is already constrained by the condition $f_{\mathrm{d}} \leq 0.1\Delta f$ to prevent fast-time-Doppler-induced effects [58], this is typically not a substantial disadvantage.

Random Frequency-Division Multiplexing

A multiplexing approach avoiding any loss of unambiguous range and velocity is random frequency-division multiplexing (RFDM), which has been introduced for MIMO OFDM radars in [32]. It involves a random assignment of the time- and frequency slots, specifically, the OFDM symbols and subcarriers, to the different Tx channels of the radar. Hereby, an irregular sampling pattern is achieved as exemplified in Fig. 5.6 (c), not leading to ambiguities, but sidelobes within the *Rv* image. Since the number of targets to be estimated is finite, it is possible to reconstruct the missing elements in the division matrix $\boldsymbol{\mathcal{D}}$ using a CS algorithm [117], [118]. In this thesis, a two-dimensional implementation of the complex approximate message passing (CAMP) [119] is used for simultaneous reconstruction in both dimensions of $\boldsymbol{\mathcal{D}}$. This algorithm has been demonstrated to achieve very good performance for this purpose as examined in detail in [120, Section 3.2].

5.4.1 Performance Comparison

The proposed multiplexing strategies FDM, TFDM, and RFDM exhibit distinct advantages and disadvantages, particularly regarding unambiguous range and velocity as well as the achievable target dynamic. This renders them suitable for different applications. In the following, these performance differences are discussed and substantiated by measurements. For the measurement, the 4×4 OFDM radar described in detail in Section 5.6 is used, accompanied by two DSB repeaters. The OFDM signal comprises 2048 OFDM symbols and 1024 subcarriers at a spacing of Δf=400 kHz.

The aforementioned influence of the multiplexing on the unambiguous range is well visible in the mono- and bistatic range profile shown in Fig. 5.7, based on measurements of a single target at R=2.4 m. While the initial unambiguous region equals R^{ua}=375 m and v^{ua}=337.5 $\frac{\mathrm{m}}{\mathrm{s}}$, it is reduced to

$$\begin{aligned}
\text{FDM:}\ \ \Delta n_{\mathrm{Tx}} = 20 \Rightarrow\ R^{\mathrm{ua}}_{\mathrm{NW}} = 18.7\,\mathrm{m}; \qquad \Delta m_{\mathrm{Tx}} = 1 \ \Rightarrow\ v^{\mathrm{ua}}_{\mathrm{NW}} = 337.5\,\mathrm{m/s};\\
\text{TFDM:}\ \ \Delta n_{\mathrm{Tx}} = 5 \ \Rightarrow\ R^{\mathrm{ua}}_{\mathrm{NW}} = 75.0\,\mathrm{m}; \qquad \Delta m_{\mathrm{Tx}} = 4 \ \Rightarrow\ v^{\mathrm{ua}}_{\mathrm{NW}} = 84.3\,\mathrm{m/s}.
\end{aligned}$$

In contrast, using RFDM, the unambiguous region is not reduced.

The sparsity of the Tx signals not only affects the unambiguous range, but

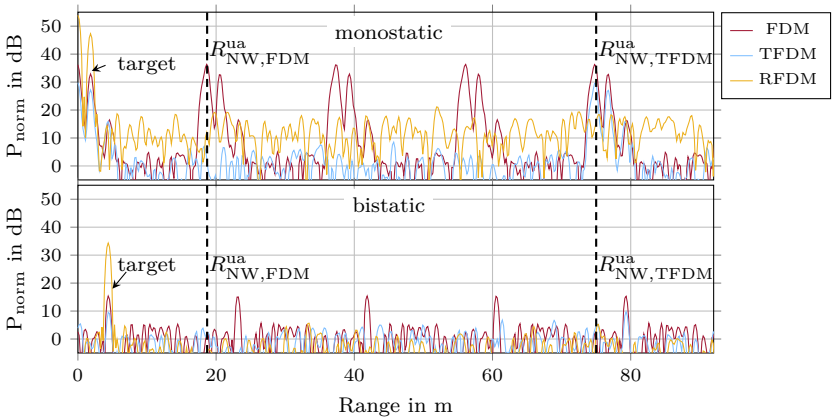

Fig. 5.7: Range profiles at v=0 m/s, normalized to the noise floor, from measurements of a single target at 2.4 m using different multiplexing methods. Adapted from [57], © 2021 IEEE.

also the dynamic performance due to reduced integration gain. For FDM and TFDM, the integration gain is reduced by a sparsity factor of $N_{\mathrm{Tx}}\,(sN_{\mathrm{RP}}+1)$. Employing RFDM further increases the sparsity by a factor of approximately 2, which is attributable to the additional unassigned slots. In addition, using TFDM the average transmitted Tx power is reduced by N_{Tx}, which is visible by the 6 dB lower PNR of TFDM compared to FDM in Fig 5.7. Yet, the highest PNR is achieved with RFDM, due to the additional pseudo-PNR obtained by reconstructing the zero-elements in $\boldsymbol{\mathcal{D}}$, which significantly increases the PNR. The reconstruction employs additional signal energy, without increasing noise energy, since the reconstruction is noise-free [120, Section 3.2.5]. Note that the increased noise in the monostatic range profile using RFDM is caused by the memory constraints of the radar, which limits the $\boldsymbol{\mathcal{D}}^{\mathrm{Tx}}$ to only four different OFDM symbols repeated at random. This leads to a rift at v=0. Nevertheless, while the aforementioned aspects indicate a superior dynamic performance of RFDM, the CS algorithm also imposes a limit on how weak a peak may be compared to the strongest peak to be detectable. Using the same parameters as depicted in Fig 5.7 and employing the CAMP algorithm [119], the dynamic

range is limited to 30 dB in this instance, as demonstrated by simulations in [57] by the author.

In summary, RFDM provides maximum R^{ua} and v^{ua}, while FDM provides the best dynamic performance. TFDM falls in between. Therefore, the choice of the multiplexing method should be based on the specific measurement scenario; however, through the digital signal generation, the multiplexing strategy can be switched or adapted easily between adjacent measurement frames.

5.5 DoA Estimation

Compared to a single MIMO sensor, radar networks allow to span an extended aperture via the subarrays of all sensor nodes. This promises high-resolution DoA estimation and radar imaging, but comes with challenges: First, phase coherency must be achieved to coherently combine the steering vectors obtained from multiple subarrays. This includes phase errors caused by the signal modulation existing in the bistatic receive signal in (5.8). Second, the steering vectors itself must be properly combined to allow for a network-based DoA estimation. By addressing the aforementioned challenges, in this section a concept for network-based DoA estimation using SymNWs is proposed, allowing to outperform the DoA estimation performance of a single radar sensor. The introduced concept has first been proposed in [73], [121] by the author.

5.5.1 Modulation Phase Recovery

Two phase error terms caused by the signal modulation within the repeater can be identified in (5.8): The first, ϕ_{mod}, corresponds to the initial phase of the modulation signal as shown in (5.6); the second to the phase rotation of the modulation signal during each CP. While the latter has been mitigated in (5.16), the first is still present as phase offsets in the phases extracted from bistatic target peaks. Using multiple bistatic signals from different repeaters for a joint DoA estimation is not feasible without compensating for ϕ_{mod}. Investigating the upper sideband (USB) modulation signal from (5.6),

$$x_{\mathrm{mod}}(t) = \mathrm{e}^{\mathrm{j}\left(2\pi h \Delta f t + \phi_{\mathrm{mod}}\right)} = \mathrm{e}^{\mathrm{j}2\pi h \Delta f (t - t_0)}\,, \tag{5.24}$$

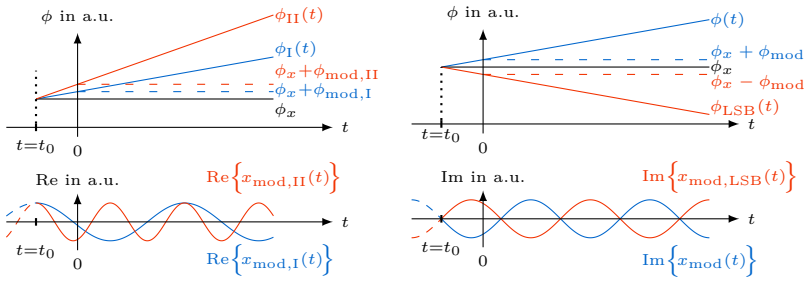

(a) Phase recovery with b=2. **(b)** Phase recovery with b=−1.

Fig. 5.8: Concept of the modulation phase recovery. By comparing the phases of two signals of the same repeater, transmitted at the same time, and obtained at the same bistatic target peak, the modulation phase ϕ_{mod} can be extracted. In (a), these are $\phi_{\mathrm{I}}(t) = \arg\left(x_{\mathrm{RP,I}}(t)\right)$ and $\phi_{\mathrm{II}}(t) = \arg\left(x_{\mathrm{RP,II}}(t)\right)$, and in (b), these are the phase obtained in the upper $\phi(t)$ and the lower $\phi_{\mathrm{LSB}}(t)$ sideband of the bistatic receive signal. (a) from [73], CC BY 4.0 https://creativecommons.org/licenses/by/4.0/. (b) from [121], © 2020 IEEE.

the initial modulation phase can be well described by a time offset t_0, which is the point in time closest to t=0 where $\arg\left(x_{\mathrm{mod}}(t_0)\right)$=0 applies. The phase of the modulation signal at the start of the measurement $t = 0$ is defined as modulation phase

$$\phi_{\mathrm{mod}} = \arg\left(x_{\mathrm{mod}}(0)\right) \tag{5.25}$$

inducing an unknown phase offset in each Rx channel which would interfere with the DoA estimation if not compensated for.

In order to recover and compensate this phase offset ϕ_{mod}, two Tx signals from the same repeater are required. Specifically, the same repeater's Rx signal is shifted on two different sets of subcarriers, either by using a two-tone modulation signal or by exploiting both sidebands when using an DSB repeater. These spectral repetitions of one repeater's Rx signal will be considered as two signals in the following, designated as $x_{\mathrm{RP,I}}(t)$ and $x_{\mathrm{RP,II}}(t)$. Seperately considering the frequency components of the modulation signal leading to each leads to

$$x_{\mathrm{mod,I}}(t) = \mathrm{e}^{\mathrm{j}2\pi h_{\mathrm{I}}\Delta f(t-t_0)} \quad \text{and} \quad x_{\mathrm{mod,II}} = \mathrm{e}^{\mathrm{j}2\pi h_{\mathrm{II}}\Delta f(t-t_0)}, \tag{5.26}$$

respectively. Both repeater Tx signals are modulated on their own set of subcarriers, hence, must be considered for multiplexing. At the radar, both signals are received and independently evaluated as described in Section 5.3. Since both share the same signal path, but the modulation phase differs in dependence on their f_{mod}, this allows for a calculation of ϕ_{mod}, as schematized in Fig. 5.8. The ratio of their modulation frequencies is defined as the modulation factor

$$b = \frac{f_{\mathrm{mod,II}}}{f_{\mathrm{mod,I}}} = \frac{h_{\mathrm{II}}}{h_{\mathrm{I}}} \ , \tag{5.27}$$

and corresponds to the relation of their phases. After *Rv* processing, the phases $\phi_{k,\mathrm{I}}$ and $\phi_{k,\mathrm{II}}$ are extracted from the bistatic *Rv* matrices obtained based on $x_{\mathrm{RP,I}}$ and $x_{\mathrm{RP,II}}$. They must be extracted at the peak of the same target in both *Rv* matrices, such that the range dependent phase term

$$\phi_x = \mathrm{e}^{-\mathrm{j}2\pi f_{\mathrm{Tx}}\left(2\tau_k^{\mathrm{bi}}+\tau^{\mathrm{RP}}\right)} \ , \tag{5.28}$$

which corresponds to the DoA estimation term in (5.8), is identical for both. Thus, as exemplarily shown in Fig. 5.8 (a) for b=2, $\phi_{k,\mathrm{I}}$ and $\phi_{k,\mathrm{II}}$ just differ in their modulation phase offset. Hence, the modulation phase of $x_{\mathrm{RP,I}}(t)$ is extracted as

$$\phi_{\mathrm{mod,I}} = \frac{\phi_{k,\mathrm{II}} - \phi_{k,\mathrm{I}}}{b-1} \ . \tag{5.29}$$

The modulation phase can be determined unambiguously for $1<b\leq 2$, hence, using b=2 is well suited for a carrier recovery. In case of a DSB repeater, it can be an alternative to use the lower sideband as second signal, which inherently leads to $b=-1$ since $f_{\mathrm{mod,II}}=-f_{\mathrm{mod,I}}$ and an ambiguous recovered ϕ_{mod} [121], as shown in Fig. 5.8 (b).

In order to validate the performance of the phase recovery, measurements are conducted and statistically evaluated. An FMCW radar is used, since, in contrast to the OFDM radar available, it allows to exactly trigger each measurement frame and this way to record ground truth values of the respective modulation phase offsets using an oscilloscope. The repeater and the radar are not placed side by side but face each other at varying distances $\tilde{R}$ to induce a high SNR variation. A DSB repeater is used, so the phase is recovered using the USB and the LSB, resulting in $b=-1$ and an ambiguous phase recovery. Fig. 5.9 illustrates the standard deviation σ of the error of the recovered phase after a

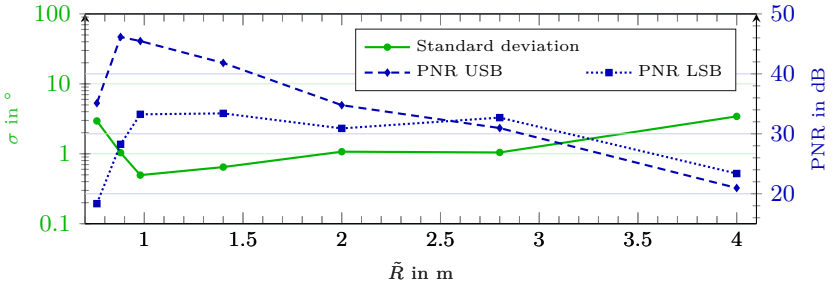

Fig. 5.9: Standard deviation σ of the phase recovery error based on measurements. One FMCW radar and one repeater face each other in varying distances $\tilde{R}$, resulting in varying PNRs of the lower sideband (LSB) and USB. Adapted from [121], © 2020 IEEE.

correction to the unambiguous region of 180°, along with the mean PNR for each distance $\tilde{R}$. The statistical evaluation is based on a total of 50 measurements per data point. As to be expected, σ is inversely proportional to the minimum of the PNRs of USB and LSB. It shows that even for a PNR below 20 dB, the standard deviation is less then 3°, validating the high reliability of the phase recovery. It should be noted that the DoA estimation error resulting from a phase error after DFT processing is significantly lower.[1] DoA estimation results using the presented modulation phase recovery are presented in Section 5.6.

5.5.2 Virtual Network Array

The VNA corresponds to the combination of the different subarrays of the network nodes. In analogy to the virtual array of MIMO radars presented in Section 2.5.2, it can be derived from the network's steering vector $\boldsymbol{a}_{\mathrm{VNA}}$, which is introduced in the following.

On radar Tx side, the phases obtained from the paths between the radar Tx channels and the target correspond to the Tx steering vector $\boldsymbol{a}_{\mathrm{Tx}}$ defined in (2.41). After the first reflection, the signal is received by the uth repeater,

[1] The consistency of the DoA estimation using the proposed modulation phase recovery is exemplarily demonstrated in [121], where a standard deviation of the estimated target angle of 0.09° is achieved.

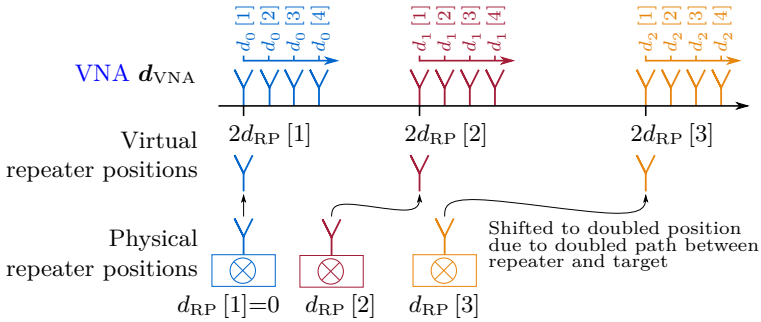

Fig. 5.10: Exemplary VNA of a SymNW consisting of three repeaters and a radar with a four-element virtual array. Partly adapted from [11], CC BY 4.0 https://creativecommons.org/licenses/by/4.0/.

inducing the ToF $\tau_u^{\mathrm{T}\to\mathrm{RP}}$. The signal is then retransmitted by the repeater, traversing the same path back from the repeater to the target since the DoA estimation is performed on basis of the ST peaks. After the second reflection, the bistatic signal is received by the N_{Rx} radar Rx channels, introducing phase shifts corresponding to the radar Rx steering vector $\boldsymbol{a}_{\mathrm{Rx}}$ defined in (2.42). Consequently, the bistatic steering vector of the uth repeater is given by

$$\tilde{\boldsymbol{a}}_{\mathrm{bi}}^{\mathrm{sub},u} = \mathrm{e}^{-\mathrm{j}2\pi f_{\mathrm{Tx}}\left(2\tau_u^{\mathrm{T}\to\mathrm{RP}}+\tau_u^{\mathrm{RP}}\right)}\boldsymbol{a}_{\mathrm{Tx}}\otimes\boldsymbol{a}_{\mathrm{Rx}}\,. \tag{5.30}$$

Hence, each repeaters' steering vector contains a repetition of the radar's steering vector, additionally shifted due to the position of the repeater and the double reflection at the target, as shown in Fig. 5.10. The ToF on the repeater hardware τ_u^{RP} is omitted from here on, since it is target-independent and mitigated by means of a calibration. So far, only the steering vectors of each repeater node have been accounted for, based solely on their corresponding subarray.

The subsequent step involves combining the signals of the N_{RP} repeaters positioned at $d_{\mathrm{RP},u}$ to form a joint steering vector. The prerequisites for this are met by the network design and signal processing: The bistatic signals are all based on the same radar signal, and the low modulation frequency does not introduce significant phase noise or frequency variations compared to the 77-GHz radar signal. In addition, it assumes that static phase offsets have been

mitigated by the CP correction and modulation phase reconstruction from Sections 5.3.2 and 5.5.1, respectively. Similar to (2.40), the normalized ToF of the path between the targets and the repeaters is

$$\overline{\tau}_{\mathrm{RP},u}\left(\theta_{\mathrm{RP}}\right) = 2\tau_u^{\mathrm{T}\star\mathrm{RP}} - 2\tau_1^{\mathrm{T}\star\mathrm{RP}} = \frac{2d_{\mathrm{RP},u}}{\mathrm{c}_0}\sin\theta_{\mathrm{RP}}\,, \tag{5.31}$$

where the factor of 2 is due to the signal traversing the path between the target and repeater twice. This yields the normalized network-node steering vector

$$\boldsymbol{a}_{\mathrm{NW}} = \begin{pmatrix} 1 & \mathrm{e}^{-\mathrm{j}\frac{2\pi}{\lambda}2d_{\mathrm{RP},2}\sin\theta_{\mathrm{RP}}} & \cdots & \mathrm{e}^{-\mathrm{j}\frac{2\pi}{\lambda}2d_{\mathrm{RP},N_{\mathrm{Rx}}}\sin\theta_{\mathrm{RP}}} \end{pmatrix}. \tag{5.32}$$

Although the far field condition from (2.39) is often not satisfied for radar networks, in the next step it is assumed that $\theta_{\mathrm{RP}}{=}\theta_{\mathrm{Tx}}{=}\theta_{\mathrm{Rx}}{=}\theta$ in order to derive the normalized network steering vector. This simplification allows to combine the phases resulting from the repeater positions denoted in (5.32), including the phase progressions of each bistatic subarray given in (5.30), yielding the steering vector based on the entire VNA as

$$\boldsymbol{a}_{\mathrm{VNA}} = \boldsymbol{a}_{\mathrm{NW}} \otimes \boldsymbol{a}_{\mathrm{Tx}} \otimes \boldsymbol{a}_{\mathrm{Rx}} \overset{(2.43)}{=\!=} \boldsymbol{a}_{\mathrm{RP}} \otimes \boldsymbol{a}\,. \tag{5.33}$$

Similar to the virtual array of a MIMO radar, the VNA can be derived from $\boldsymbol{a}_{\mathrm{VNA}}$ and is composed of the radar's virtual array shifted to the position of the repeaters as

$$\boldsymbol{d}_{\mathrm{VNA}} = 2\boldsymbol{d}_{\mathrm{RP}} \oplus \boldsymbol{d}_{\mathrm{Tx}} \oplus \boldsymbol{d}_{\mathrm{Rx}} \overset{(2.47)}{=\!=} 2\boldsymbol{d}_{\mathrm{RP}} \oplus \boldsymbol{d}\,, \tag{5.34}$$

where the factor of 2 from (5.32) directly is considered within $\boldsymbol{d}_{\mathrm{VNA}}$. In conclusion, the VNA comprises a repetition of the radar's virtual array for each repeater, shifted to its doubled position due to the twice-traversed path between the target and the repeater.

There are two additional points worth noting. First, the presented network steering vector and VNA combine only the bistatic signals and subarrays; the monostatic signal is not used for DoA estimation since a common phase normalization is challenging due to the double reflection of the bistatic signals at the target. Second, in (5.33) and (5.34), the far-field condition from (2.39) is assumed to be fulfilled, which typically is not true for close targets. However, by applying a near-field correction as presented by the author in [122], the network

steering vector can be shifted into far-field despite the target being in near-field. This is accomplished by calculating the near-field phase terms using a priori information obtained from both the range estimation and the monostatic DoA estimation using only the MIMO radar.

5.5.3 Compressed-Sensing-based DoA Estimation

Because of the potentially large gaps between the subarrays of adjacent repeaters, the VNA is typically very sparse. This typically results in a high sidelobe level (SLL) in the DoA estimation, thus, weak targets are likely covered by sidelobes in the presence of a stronger target. However, by applying a CS algorithm for DoA estimation, the missing phases in the sparse steering vector are reconstructed, which reduces the SLL. Consequently, the CS algorithm enables the restoration and detection of albeit weak target peaks.

In this work, an FFT-based DoA estimation [64] is combined with an iterative method with adaptive thresholding (IMAT) algorithm for CS reconstruction [123]. This combination has first been proposed for the DoA estimation using single MIMO radars with sparse virtual arrays [67], which is adaptable to VNAs as shown in [11], [73] by the author. As explained in detail in [11], in case of sparse VNAs an interpolation using zero padding (ZP) is crucial to avoid aliasing effects within the network-based DoA estimation.

The IMAT algorithm transforms the phases from the steering vector, as assigned to the sparse VNA, into the angular-spectrum-domain. Then, a threshold is applied, and based on the frequency components over the threshold, the missing positions in the VNA are reconstructed. In the next step, this is repeated, but with already including the reconstructed phases from the previous iteration. The algorithm terminates after a specified number of iterations, while in each iteration the threshold level is reduced. This way, in each iteration sparsity-induced sidelobes are reduced and weak targets initially below the SLL become visible and detectable.

5.6 Measurements

In order to verify the DoA estimation capabilities of the symmetric-path radar-repeater network, measurements in an anechoic chamber are performed. This

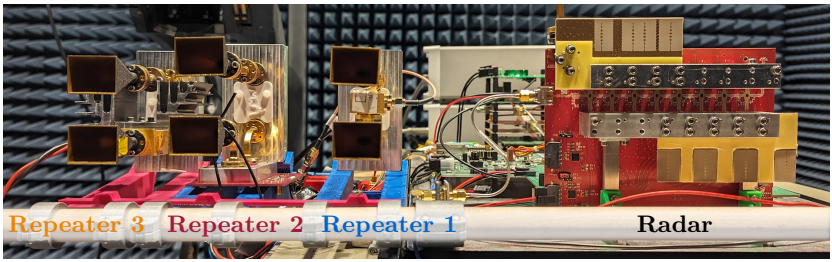

Fig. 5.11: Radar network setup of a 4×4 OFDM radar and three SSB repeaters. Each repeater includes an additional waveguide amplifier at Tx.

includes measurement scenarios with a single target, as well as with two targets in the same *Rv*-cell. Thereby, the measurements facilitate the assessment of the single-target DoA estimation performance, in particular the SLL before CS, as well as the target separability.

5.6.1 Radar Network Setup

The setup shown in Fig. 5.11 includes a 4×4 77-GHz digital radar demonstrator presented in detail in [13]. In addition to the radar, three SSB repeaters are used, as described in Section 5.1 and shown in Fig. 5.2 (b). Each repeater is extended by an additional waveguide amplifier inserted between its output and its Tx antenna to increase bistatic signal power. This way, a SymNW yielding a VNA composed of three subarrays is designed, which establishes a sparse VNA of length $239\,\lambda/2$.

The radar consists of a 77-GHz radar frontend, including an interchangeable antenna frontend with four Tx and four Rx channels, along with a backend generating and digitizing the signal. Main part of the backend is a Xilinx RFSoC, which is an field-programmable gate array (FPGA) incorporating eight DACs and eight ADCs [33] used to generate and digitize both I and Q data for all Tx and Rx channels. It operates with a sample frequency of 1 GHz, which is limited by data handling speed [13]. Additionally, the backend contains a PCB with baseband amplifiers and filters, which connects the DACs and ADCs to the frontend. The frontend incorporates eight MMICs, each containing a Tx

Tab. 5.1: Radar antenna placement.

	Tx array				Rx array			
Element	$d_{\mathrm{Tx},0}$	$d_{\mathrm{Tx},1}$	$d_{\mathrm{Tx},2}$	$d_{\mathrm{Tx},4}$	$d_{\mathrm{Rx},0}$	$d_{\mathrm{Rx},1}$	$d_{\mathrm{Rx},2}$	$d_{\mathrm{Rx},3}$
$x/\frac{\lambda}{2}$	0	9	13	24	0	14	28	41

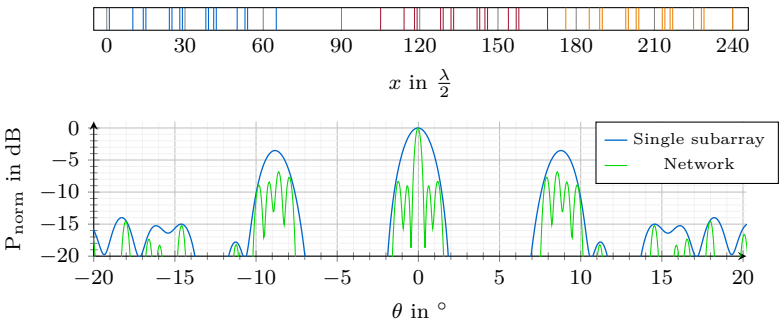

Fig. 5.12: VNA of the radar-repeater network (top), and the calculated angular spectrum of a single target at 0° (bottom). In the VNA, each color corresponds to the subarray of one repeater, consistent with the colors of the repeaters in Fig. 5.11. From [11], CC BY 4.0 https://creativecommons.org/licenses/by/4.0/.

and a Rx channel, whereby each is used either as Tx or as Rx to avoid the severe on-chip leakage. Finally, the antennas placed on an extra antenna PCB connected via waveguide transitions are eight-element patch arrays presented in [65], which provide an isotropic gain of G_i=15.6 dBi.

The radar network forms a VNA consisting of three sparse subarrays of 16 elements, each 65 $\lambda/2$ in size. As explained in Section 5.5.2, all subarrays are defined by the radar array, which comprises an antenna placement as described in Tab. 5.1. The resulting VNA is shown at the top of Fig. 5.12. It has a size of 239 $\lambda/2$, leading to a theoretical resolution of 0.584° according to the Rayleigh criterion [72]. As shown in the calculated angular spectrum of a target at 0° in Fig. 5.12, the VNA allows for a reasonable SLL of 6.8 dB.

Tab. 5.2 gives an overview of the OFDM parameters used in the measurements. Due to the limitations of the radar, a bandwidth of 410 MHz is chosen, which

Tab. 5.2: OFDM radar parameters.

Carrier frequency	f_{Tx}	77 GHz
Subcarrier spacing	Δf	100 kHz
Bandwidth	B	0.410 GHz
Number of subcarriers	N	4104
Number of OFDM symbols	M	2048
CP length	T_{CP}	0.5 μs
Range resolution	ΔR	0.365 m
Velocity resolution	Δv	0.09 $\frac{\mathrm{m}}{\mathrm{s}}$
Unambigous range	$R^{\mathrm{ua}}_{\mathrm{NW}}=R^{\mathrm{ua}}/36$	41.6 m
Unambigous velocity	$v^{\mathrm{ua}}_{\mathrm{NW}}=v^{\mathrm{ua}}$	$\pm$92.6 $\frac{\mathrm{m}}{\mathrm{s}}$

is allocated to 4104 subcarriers with a 100-kHz spacing. A high number of 2048 OFDM symbols is selected to achieve a high integration gain. The multiplexing strategy used is FDM, since the maximum range is limited anyway by the size of the anechoic chamber and the limited bistatic signal power. As indicated in Tab. 5.3, each repeater modulates on two frequencies for carrier recovery with a factor of b=2, ensuring unambiguous phase reconstruction. Fig. 5.4 shows the resulting subcarrier assignment. Note that due to the chosen b=2, there are empty subcarriers, resulting in Δn_{Tx}=36. In total, the unambiguous range is reduced from R^{ua}=1499 m to $R^{\mathrm{ua}}_{\mathrm{NW}}$=41.6 m.

In the measurements presented the DoA estimation is performed with a ZP that extends to eight times the size of the VNA. The calibration is carried out with one pole at boresight, and the DoA estimation is performed without near-field correction, since the poles in the measurement are in approximately the same range as in the calibration.

5.6.2 Single-Target Scenario

The first step is to verify the DoA estimation capabilities of the network regarding the SLL resulting from the VNA. Therefore, a single copper pole with a diameter of 28 mm is placed at a distance of 1.2 m and at an angle of 3.8°.

The result of the DoA estimation is shown in Fig. 5.13, contrasting the DoA estimation using the radar alone (—) against that using the network with (—) and without CS (····). Upon evaluating the measurement based on the network but without CS, the SLL amounts to 6.3 dB, nearly reaching the theoretical value

Tab. 5.3: Modulation frequencies of the repeaters.

	Repeater 1	Repeater 2	Repeater 3
f_{mod}	$1\,\Delta f$ and $2\,\Delta f$	$3\,\Delta f$ and $6\,\Delta f$	$4\,\Delta f$ and $8\,\Delta f$

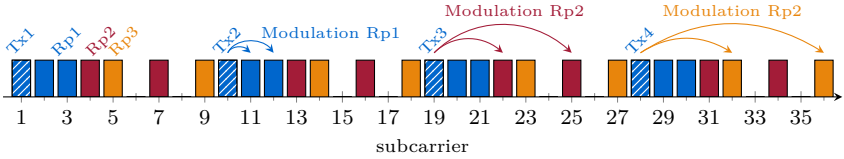

Tab. 5.4: Subcarrier assignment in the measurements and frequency shift applied by the repeaters. One pattern is shown, including signals of all radar Tx channels Tx1–Tx4 ▨. Each Tx signal is modulated and retransmitted by each repeater, shifted on the subcarriers ■ (repeater 1), ■ (repeater 2), and ■ (repeater 3). The pattern is repeated 114 times.

of 6.8 dB. With CS, most of the sidelobes are successfully mitigated by about 20 dB, with only two remaining close to the target exhibiting less mitigation. This is an indication of deviations in the repeater positions, probably caused by inaccuracies in the network setup. The target angle estimated using the radar network is offset from the ground truth by −0.7°. However, the monostatic DoA estimation similarly deviates by −0.9°, so both can be assumed to be caused by a misalignment of the measurement setup.

5.6.3 Multi-Target Scenario

The next measurement scenario involves two targets positioned within the same *Rv*-cell, facilitating the assessment of DoA performance in this particular case, as well as the target separability. Fig. 5.14 shows the measurement results of two copper poles situated 1.07° apart at a range of R=1.35 m. While with the radar alone, only one peak is visible, the targets are well separable using the network. However, high sidelobes occur, and the CS algorithm reconstructs three peaks instead of the expected two ones.

A similar outcome is observed in Fig. 5.15. In this scenario, two aluminum poles are measured, each with a diameter of 10 mm, positioned 1.83° apart at

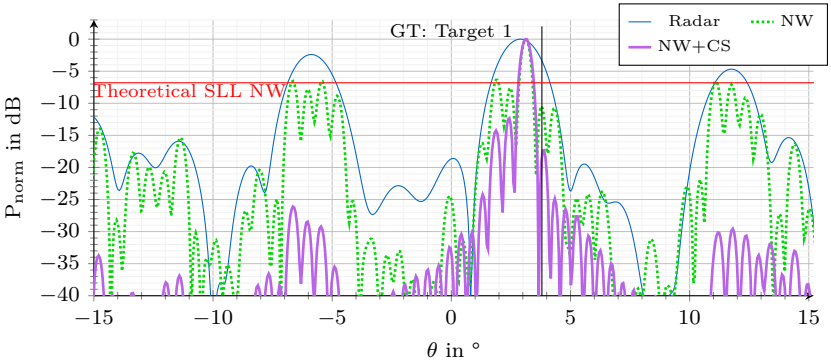

Fig. 5.13: DoA estimation results of a measurement of a single pole positioned at 3.8° at a range of 1.2 m.

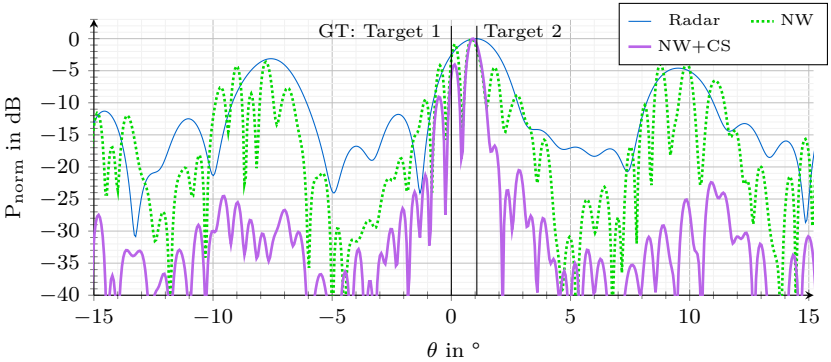

Fig. 5.14: DoA estimation results of a measurement of two poles positioned at 0° and 1.07°, respectively, at a range of 1.35 m.

R=1.25 m. Both targets are detected, yet the SLL is only 1.4 dB.

However, the issues faced by the radar network in scenarios involving multiple targets in the same *Rv*-cell can be attributed to multi-target propagation.

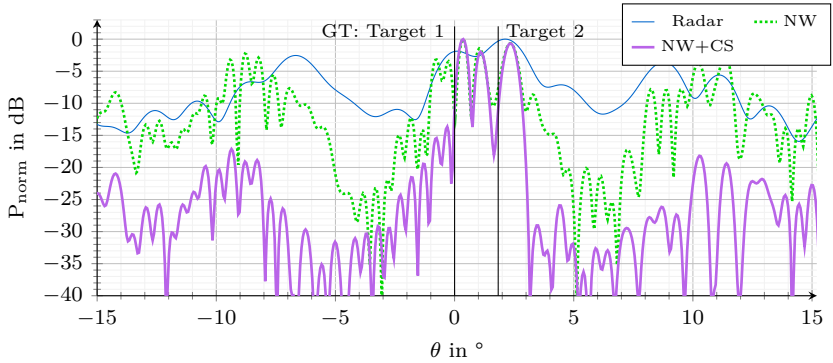

Fig. 5.15: DoA estimation results of a measurement of two poles positioned at 0° and 1.83°, respectively, at a range of 1.25 m.

5.6.4 Multi-Target Propagation in the DoA Estimation

In case of multiple targets within the same *Rv*-cell, the DoA estimation is affected by MT propagation. Specifically, this effect arises from signal paths that reflect off one target on their way to the repeater and off another target on their way back. This effect can be mathematically elucidated based on the network steering vector introduced in Subsection 5.5.2. Considering two targets at the angles θ_{T1} and θ_{T2}, and for simplification, assuming targets located in the far-field, the resulting MT steering vector equals

$$\begin{aligned}\boldsymbol{a}_{\mathrm{MT}}\left(\theta_{\mathrm{T1}},\theta_{\mathrm{T2}}\right) = &\underbrace{A_{\mathrm{T1}}\boldsymbol{a}_{\mathrm{NW}}(\theta_{\mathrm{T1}}) + A_{\mathrm{T2}}\boldsymbol{a}_{\mathrm{NW}}(\theta_{\mathrm{T2}})}_{\text{desired}} \\ &+ \underbrace{\frac{A_{\mathrm{T1}}+A_{\mathrm{T2}}}{2}\boldsymbol{a}_{\mathrm{Tx}}(\theta_{\mathrm{T1}}) \otimes \boldsymbol{a}_{\mathrm{Rx}}(\theta_{\mathrm{T2}}) \otimes \boldsymbol{a}_{\mathrm{MT,RP}}(\theta_{\mathrm{T1}},\theta_{\mathrm{T2}})}_{\text{MT propagation T1}\rightarrow\text{T2}} \\ &+ \underbrace{\frac{A_{\mathrm{T1}}+A_{\mathrm{T2}}}{2}\boldsymbol{a}_{\mathrm{Tx}}(\theta_{\mathrm{T2}}) \otimes \boldsymbol{a}_{\mathrm{Rx}}(\theta_{\mathrm{T1}}) \otimes \boldsymbol{a}_{\mathrm{MT,RP}}(\theta_{\mathrm{T2}},\theta_{\mathrm{T1}})}_{\text{MT propagation T2}\rightarrow\text{T1}} .\end{aligned} \tag{5.35}$$

The amplitude factors A_{T1} and A_{T2} account for the power differences between the signals received via each target. Besides the desired network steering vectors of both targets, the MT steering vectors based on the Tx and Rx steering vectors

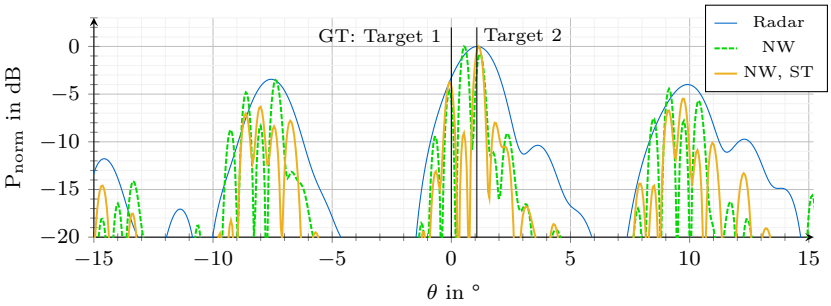

Fig. 5.16: Simulation of two targets at 0°; RCS=−3 dB and 1.07°; RCS=0 dB. The DoA estimation result without CS obtained from a full simulation incorporating MT paths is compared to that of a simulation considering only ST paths.

of different targets are included. Likewise, the corresponding repeater steering vectors are based on different targets:

$$\begin{aligned} &\boldsymbol{a}_{\mathrm{MT,RP}}(\theta_{\mathrm{T1}},\theta_{\mathrm{T2}}) = \boldsymbol{a}_{\mathrm{MT,RP}}(\theta_{\mathrm{T2}},\theta_{\mathrm{T1}}) \\ &= \left(1 \;\; \mathrm{e}^{-\mathrm{j}\frac{2\pi}{\lambda}d_{\mathrm{RP},2}\left(\sin\theta_{\mathrm{T1}}+\sin\theta_{\mathrm{T2}}\right)} \;\; \cdots \;\; \mathrm{e}^{-\mathrm{j}\frac{2\pi}{\lambda}d_{\mathrm{RP},N_{\mathrm{Rx}}}\left(\sin\theta_{\mathrm{T1}}+\sin\theta_{\mathrm{T2}}\right)}\right) . \end{aligned} \tag{5.36}$$

The impact of MT propagation on the DoA estimation is best illustrated through simulations, since they allow to deactivate MT paths. The simulations employ the same OFDM parameters presented in Tab. 5.2. In Fig. 5.16, simulation results are shown resembling the scenario measured in Fig. 5.14. The target at 0° has a RCS of 3 dB less than the RCS of the target at 1.07° to match the peak powers in the measurement scenario. Without MT propagation, two distinct peaks at the correct angles are obtained. In contrast, including MT propagation in the simulation framework yields an additional peak in between. The simulation results closely match the measurement results presented in Fig. 5.14, and the presence of the additional peak is also observed in Fig. 5.15. Consequently, the third peak must be taken into account when interpreting the result of the DoA estimation.

Nevertheless, two targets with a large angular difference may not give rise to a third peak, but may generate very high sidelobes. This can be noticed in

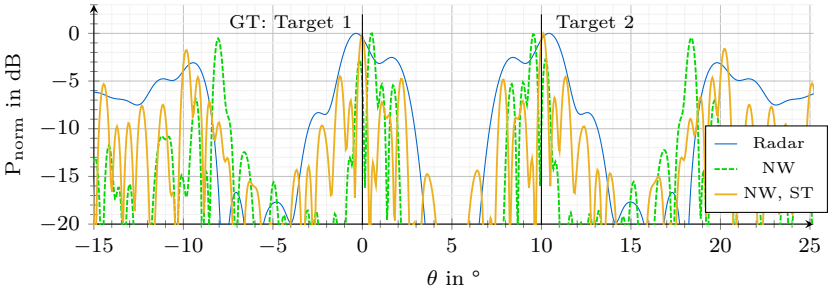

Fig. 5.17: Simulation of two targets at 0°, RCS=0 dB and 10°, RCS=0 dB. The DoA estimation result without CS obtained from a full simulation incorporating MT paths is compared to that of a simulation considering only ST paths.

Fig. 5.17, which shows a simulation of two targets at 0° and 10°. Yet, with this large angle difference, the targets are already separable in the monostatic DoA estimation using only the radar, allowing a correct interpretation of the scene.

5.7 Discussion

The OFDM radar network presented in this section uses repeaters as supplementary sensor nodes to preserve the coherency of the mono- and bistatic signals. By combining the repeaters' capability to shift the signal by a specified frequency with the multicarrier structure inherent in OFDM signals, the network achieves orthogonal signals through intercarrier interleaving. Consequently, this allows for the distinct monostatic and bistatic signals to be evaluated independently and leveraged for network-based DoA estimation. Thereby, the target separability is enhanced through the utilization of the extended VNA.

However, the underlying network concept of the SymNW, wherein the repeaters receive signals from the channel, i.e., via reflections at the targets, and transmit them back into the channel, presents certain drawbacks. These are high additional losses in signal power and the aforementioned effects resulting from MT propagation. The latter not only impacts *Rv* estimation, but also DoA estimation, and must be taken into account when interpreting measurement results.

6 Network Concept III – OFDM Radar Network Using Triangular Path Multi-Channel Repeater

By preserving the coherency between their Rx and Tx signal, repeaters allow for bistatic signals that are inherently frequency coherent and have correlated phase noise. Furthermore, their capability to shift their Rx signal by a low frequency before retransmission allows for orthogonal monostatic and bistatic signals when combined with an OFDM radar. However, a SymNW, as presented in Chapter 5, also introduces inherent drawbacks, specifically, high attenuation of the bistatic signals and MT propagation. Both are caused by the double path via reflections at the targets, on the way from the radar to the repeater and back again. The radar-repeater network presented in this chapter aims to overcome these drawbacks while preserving the benefits by introducing a direct LoS path between the radar and the repeaters. This results in what is called a triangular-path radar-repeater network (TriNW), first proposed in [11] by the author. Through a dedicated LoS path, a double path via the targets is avoided, which significantly improves the dynamic range of the bistatic signals and prevents MT propagation altogether.

Nevertheless, the TriNW also has a shortcoming. Each repeater acts as an additional Tx channel, thus leading only to the repetition of the radar's Rx array in the VNA. Consequently, the VNA is more sparse compared to a SymNW when using the same number of single-channel repeaters. To still achieve a sufficient number of virtual antennas and thus overcome this problem, this chapter introduces a new type of repeater: The so-called multi-channel repeater (MCR). It internally distributes its Rx signal to several repeater Tx channels, each incorporating a dedicated mixer using its own modulation frequency. Consequently, the additional Tx channels on each repeater allow for a less sparse VNA while still providing orthogonal bistatic signals.

These MCR and the measurement system are introduced in Section 6.1, followed in Section 6.2 by the introduction of a signal model which accounts

for the monostatic and bistatic signals occurring in a TriNW. In Section 6.3, a bistatic signal processing concept is proposed, adapting conventional OFDM signal processing to the TriNW. Section 6.4 presents the multiplexing concept used, which is then followed by the DoA estimation concept proposed for the TriNW in Section 6.5. Finally, measurements in an anechoic chamber presented in Section 6.6 verify the outstanding DoA estimation performance of the proposed radar-repeater network.

6.1 System and Measurement Setup

Fig. 6.1 provides an overview of the TriNW. Most importantly, the MCR receives a signal from the radar via a LoS path. While it is advantageous to have a dedicated signal from the radar used only to feed the MCRs, this is not feasible for the available OFDM radar hardware due to the lack of a sufficient number of Tx channels. Therefore, an alternative approach is developed that splits the signal of one Tx channel by means of a power divider to feed both, the LoS antenna in addition to the corresponding radar Tx antenna. In this thesis, the latter is implemented directly on the antenna PCB. Hereby, analogous to Chapter 5, the OFDM radar demonstrator introduced in Section 5.6.1 is used. The MCR then receives the LoS signal via a waveguide antenna and splits it up into its four Tx channels using a power divider, as illustrated on the right side in Fig. 6.1. Each channel features its dedicated DSB mixer. In conclusion, every MCR transmits four bistatic signals into the channel, which are received by the radar Rx channels after being reflected by the targets.

A detailed block diagram of the MCR is depicted in Fig. 6.1 (right), complemented by a photo of the MCR shown in Fig. 6.2. It incorporates a waveguide transition for the LoS Rx antenna and six UMS CHA2080-98F VGAs, resulting in a total of three cascaded amplifiers in every signal path. A UMS CHM2179b98F DSB mixer is integrated into each channel before the last VGA stage. Each VGA provides a maximum gain of 22 dB, while the mixer has a conversion loss of 21.2 dB. Taking into account the loss of the power splitters of 3.2 dB each, and an additional loss of 2.8 dB due to the 3.7 cm of microstrip line per channel[1], the total repeater gain equals 35.6 dB. This repeater gain

[1] The PCB substrate Rogers 3003G2 127 µm is characterized to have a loss of 0.75 dB/m for microstrip lines at 77 GHz [124].

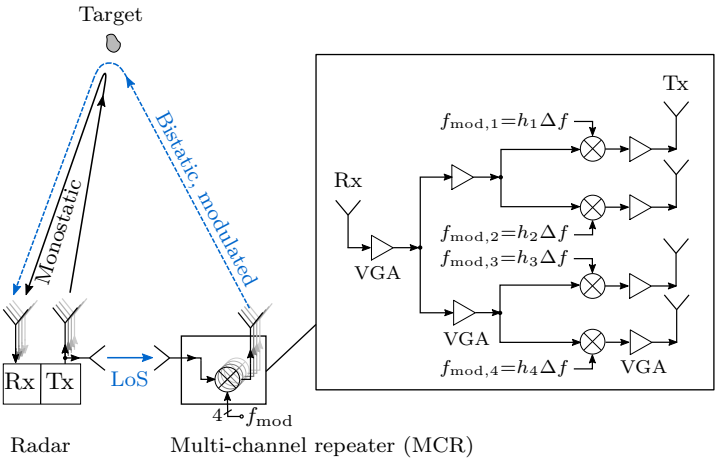

Fig. 6.1: Concept of the TriNW (left), and block diagram of the MCR proposed in this work (right). Adapted from [11], CC BY 4.0 https://creativecommons.org/licenses/by/4.0/.

must compensate for the losses of the LoS path, as well as the unknown losses from the waveguide transition and the VGA bond ribbons. Finally, analogous to the radar frontend, eight-element patch antenna arrays are used, positioned as described in Tab. 5.1 for the radar Tx array.

6.2 Signal Model

The signal received by the MCR via the LoS path is described as

$$y_{\mathrm{MCR}}(t) = L_{\mathrm{LoS}}\, x_{\mathrm{LoS}}\left(t - \tau^{\mathrm{LoS}}\right), \tag{6.1}$$

where τ^{LoS} accounts for the ToF and L_{LoS} for the attenuation within the LoS path. It is assumed that there is no relative motion between the radar and the MCR, so no LoS Doppler is considered in (6.1). While τ^{LoS} causes a range and phase offset in the bistatic radar evaluation, this can be compensated for by calibration.

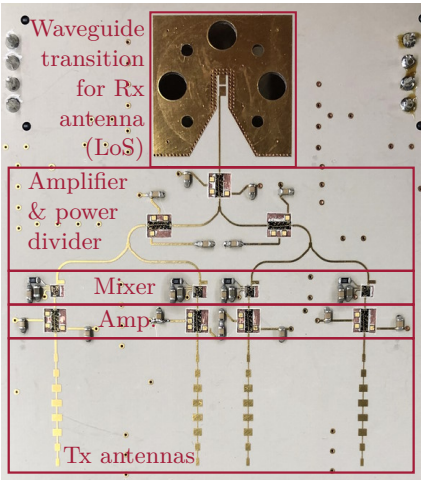

Fig. 6.2: Photography of the MCR. From [11], CC BY 4.0 https://creativecommons.org/licenses/by/4.0/.

Similar to a SymNW, the repeater's Rx signal in a TriNW is shifted by an integer number of Δf. Together with a sparse radar Tx signal that has unassigned subcarriers for each MCR's channels, this allows for orthogonal mono- and bistatic signals. An exemplary subcarrier assignment is shown in Fig. 6.3, visualizing FDM for a network with two four-channel MCRs. Consequently, similar to (5.6), the Tx signal of the lth MCR channel equals

$$\begin{aligned} x_{\mathrm{MCR},l}\left(t\right) = A_{\mathrm{MCR},l}\; y_{\mathrm{MCR}}\left(t-\tau_l^{\mathrm{MCR}}\right) \\ \times\left(\mathrm{e}^{\mathrm{j}\left(2\pi h_l \Delta f t+\phi_{\mathrm{mod},l}\right)}+L_{\mathrm{IR}}\mathrm{e}^{-\mathrm{j}\left(2\pi h_l \Delta f t+\phi_{\mathrm{mod},l}\right)}\right), \end{aligned} \tag{6.2}$$

where $A_{\mathrm{MCR},l}$ and τ_l^{MCR} are defined as the amplitude alteration and the ToF of the MCR channel, respectively. L_{IR} corresponds to the image rejection factor. As DSB mixers are used in this work, $L_{\mathrm{IR}}{\approx}1$ holds. In addition to the subcarrier shift, the signal includes a phase offset $\phi_{\mathrm{mod},l}$ corresponding to the modulation phase at the start of the OFDM signal ($t{=}0$). Furthermore, the modulation signal

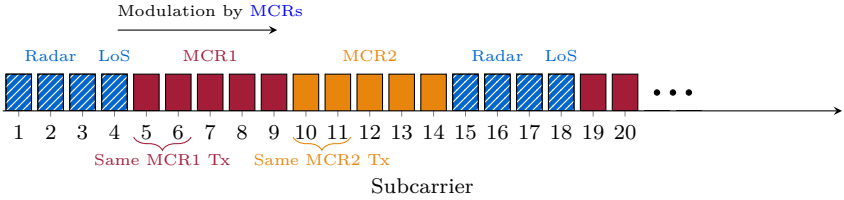

(a) Two four-channel MCRs with SSB mixers.

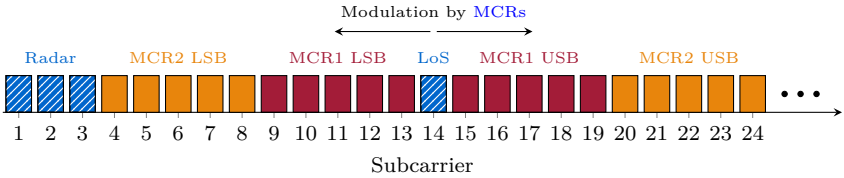

(b) Two four-channel MCRs with DSB mixers.

Fig. 6.3: Subcarrier assignment of a TriNW, exemplarily for a network consisting of a radar with N_{Tx}=4 and two four-channel MCRs. The signal transmitted to the LoS path equals the signal of Tx4. (a) shows the assignment for MCRs with SSB mixers; (b) the assignment for MCRs with DSB mixers, where the subcarriers of the LSB are modulated onto their respective set of subcarriers to avoid self-interference. (a) from [11], CC BY 4.0 https://creativecommons.org/licenses/by/4.0/; (b) based on [11].

is continuous during the CP, thus it introduces a slow-time phase progression $m\Delta\varphi_{\mathrm{mod}}(h_l)$.

6.2.1 Bistatic Receive Signal

The signal path from the MCR's Tx to the radar's Rx with a reflection at the kth target yields the range $R_k + R_k^{\mathrm{RP}}$ and velocity $v_k + v_k^{\mathrm{RP}}$, where R_k^{RP} and v_k^{RP} correspond to the distance and radial velocity between MCR and target. Consequently, the bistatic Doppler frequency $f_{\mathrm{d},k}^{\mathrm{bi}}$ and the bistatic phase progression $\theta_k^{\mathrm{bi}}[n]$ via the subcarriers are defined as in (5.3) and (5.4), respectively. Similar to (2.29) and (5.8), the bistatic Rx matrix in a TriNW is

described by its elements

$$\mathcal{D}^{\mathrm{Rx,bi}}_{n+h_l,m} = \mathcal{D}^{\mathrm{Tx}}_{n,m} A_{\mathrm{MCR},l} \underbrace{\mathrm{e}^{\mathrm{j}\phi_{\mathrm{mod}}} \mathrm{e}^{\mathrm{j}m\Delta\varphi_{\mathrm{mod}}(h_l)}}_{\text{modulation phase errors}} \times \sum_{k=1}^{N_{\mathrm{T}}} A_k \underbrace{\mathrm{e}^{\mathrm{j}\left(\theta^{\mathrm{bi}}_k[n+h_l]+\theta^{\mathrm{MCR}}[n]+\theta^{\mathrm{LoS}}[n]\right)}}_{\text{range estimation}} \underbrace{\mathrm{e}^{-\mathrm{j}2\pi f_{\mathrm{Tx}}\left(\tau^{\mathrm{bi}}_k+\tau^{\mathrm{LoS}}+\tau^{\mathrm{MCR}}\right)}}_{\text{DoA estimation}} \underbrace{\mathrm{e}^{\mathrm{j}2\pi f^{\mathrm{bi}}_{\mathrm{d},k} mT}}_{\text{velocity est.}} . \tag{6.3}$$

Compared to the bistatic Rx matrix (5.8) of the SymNW, the modulation phase errors remain. However, each summand, i.e., each path via a reflection at a target, only depends on one dedicated target, as no MT propagation occurs. Furthermore, since the channel with a reflection at the targets is only traveled once, after the modulation within the MCR, the bistatic range-depended phase $\theta^{\mathrm{bi}}_k[n+h_l]$ only depends on the subcarrier where it is received on. This facilitates a straight-forward range estimation, equivalent to the monostatic one. The influences of ToFs in the LoS path and on the MCR, τ^{LoS} and τ^{MCR}, respectively, as well as the corresponding phase progressions via the subcarriers, $\theta^{\mathrm{MCR}}[n]$ and $\theta^{\mathrm{LoS}}[n]$, are target-independent and constant, thus, can be mitigated using a calibration. Therefore, the signal processing includes the correction of the modulation phase errors, but otherwise allows to follow the conventional OFDM signal processing from Section 2.3.2.

6.3 Bistatic Signal Processing

While the monostatic signals from the radar are processed as described in Section 2.3.2, the evaluation of the bistatic signals from the MCR requires some adaptations. The MCRs receive an OFDM signal via the LoS based on the transmit matrix $\boldsymbol{\mathcal{D}}^{\mathrm{LoS}}$, which either is an OFDM signal used exclusively for the LoS link or, as in this work, the same signal transmitted by a radar Tx channel. In the latter case, $\boldsymbol{\mathcal{D}}^{\mathrm{LoS}}$ is equal to $\boldsymbol{\mathcal{D}}^{\mathrm{Tx}}$ of the corresponding channel.

The Rx matrix $\boldsymbol{\mathcal{D}}^{\mathrm{Rx,NW}}$=DFT$\uparrow[\boldsymbol{\mathcal{Y}}]$ thereby corresponds to a superposition of the Rx matrices representing the monostatic and bistatic signals, resulting in $\boldsymbol{\mathcal{D}}^{\mathrm{Rx,NW}}$=$\boldsymbol{\mathcal{D}}^{\mathrm{Rx}}$+$\boldsymbol{\mathcal{D}}^{\mathrm{Rx,bi}}$. The monostatic division matrices are computed as described in (2.30). In contrast, since the lth MCR channel shifts the LoS matrix

by h_l subcarriers, the respective bistatic division matrices are calculated as

$$\boldsymbol{\mathcal{D}}(h_l) = \boldsymbol{\mathcal{D}}^{\mathrm{Rx,NW}} \odot \left(\boldsymbol{\mathcal{D}}^{\mathrm{LoS}}(h_l)\right)^* . \tag{6.4}$$

Afterwards, the CP compensation is applied as described in Section 5.3.2. This way, the CP-dependent phase error $\mathrm{e}^{\mathrm{j}m\Delta\varphi_{\mathrm{mod}}(h_l)}$ is compensated for. Then, the velocity and range estimation is performed with a row-wise $\overrightarrow{\mathrm{DFT}}$ and a column-wise IDFT$\downarrow$, respectively, in the same manner as described in Section 2.3.2.

6.4 Multiplexing

Similar to a SymNW, the mixer in an MCR channel allows to shift the signal by a low modulation frequency. Thus, for the lth MCR channel, a modulation frequency

$$f_{\mathrm{mod},l} = h_l \Delta f, \qquad h_l \in \mathbb{Z} \setminus 0 \tag{6.5}$$

is chosen to enable subcarrier interleaving in the network. Orthogonality is assured if the conditions

$$\begin{aligned} \boldsymbol{\mathcal{D}}^{\mathrm{LoS}}(h_l) \odot \boldsymbol{\mathcal{D}}_p^{\mathrm{Tx}} &= \mathbf{0}^{N,M}, && \text{and} \\ \boldsymbol{\mathcal{D}}^{\mathrm{LoS}}(h_l) \odot \boldsymbol{\mathcal{D}}^{\mathrm{LoS}}(h_k) &= \mathbf{0}^{N,M}, && h_l \neq h_k \end{aligned} \tag{6.6}$$

are fulfilled for all h_l, h_k used for an MCR channel and all radar Tx channels $\{p \in 1, \ldots, N_{\mathrm{Tx}}\}$.

In principle, all multiplexing schemes presented in Section 5.4 can be adapted for a TriNW, with similar advantages and disadvantages as analyzed there. However, w.l.o.g., FDM is chosen here for illustration. Fig. 6.3 (a) shows an FDM multiplexing concept using the example of two four-channel MCRs with SSB mixers. Here the LoS signal is equal to the signal transmitted by Tx4 of the radar, so $\boldsymbol{\mathcal{D}}^{\mathrm{LoS}} = \boldsymbol{\mathcal{D}}_4^{\mathrm{Tx}}$. It can be observed that each of the MCRs occupies five subcarriers before the pattern repeats, because for each MCR, one channel modulates to two subcarriers to allow for modulation phase recovery. Thereby, it is assumed that the modulation sources for all channels of the same MCR are coherent, which will be explained in detail in section 6.5.1. Fig 6.3 (b) shows the subcarrier assignment for an identical network, but with DSB mixers. In this case, the LSB of each MCR channel must be considered, which is shifted

to the subcarriers below Tx4.

Considering a radar network with N_{Tx} radar Tx channels and N_{MCR} MCRs with $N_{\mathrm{Tx,MCR}}$ channels each, the spacing between two subcarriers occupied by the same channel equals

$$\Delta n_{\mathrm{Tx}}^{\mathrm{FDM}} = N_{\mathrm{Tx}} + sN_{\mathrm{MCR}} \left(N_{\mathrm{Tx,MCR}} + 1 \right) , \tag{6.7}$$

where s=1 for SSB mixers and s=2 for DSB mixers. The additional subcarrier per MCR for the modulation phase recovery is considered. Similar to FDM for SymNWs, this leads to a reduction of the unambiguous range by factor $\Delta n_{\mathrm{Tx}}^{\mathrm{FDM}}$.

6.5 DoA Estimation

In the next step, the network is exploited to provide a network-based DoA estimation. Therefore, at first, the recovery and mitigation of the phase error caused by the signal modulation within the MCR is proposed. Then, the network's subarrays (SAs) are combined to form a VNA. In contrast to the DoA estimation proposed in Section 5.5 for SymNW, this includes both, the monostatic and the bistatic SAs.

6.5.1 Modulation Phase Recovery

Without any synchronization between the radar and the MCRs, the phase of the modulation signals is unknown. In equivalence to (5.24), the modulation signal of the lth channel of an MCR equals

$$x_{\mathrm{mod},l}\left(t\right) = \mathrm{e}^{\mathrm{j}2\pi h_l \Delta f \times (t - t_0)} , \tag{6.8}$$

including the time offset t_0, corresponding to the point in time closest to t=0 where $\arg\left(x_{\mathrm{mod}}(t_0)\right)$=0 applies. Consequently, the phase of the bistatic signals is alternated by

$$\phi_{\mathrm{mod},l} = -h_l \Delta f t_0 . \tag{6.9}$$

If coherency of the modulation sources of all signals of the same MCR is ensured, ϕ_{mod} only has to be reconstructed for one of the channels of the MCR, and be deduced from this for the other ones. This is possible due to the fixed

relationship between the different modulation phases

$$\phi_{\mathrm{mod},l} = \frac{h_l}{h_1}\phi_{\mathrm{mod},1}. \tag{6.10}$$

Therefore, when reconstructing the modulation phase for the reference channel l=1, the other modulation phases can be deduced. As this can only be done unambiguously for $h_l/h_1 \geq 1$, it is advisable to use the channel with the lowest modulation index as reference channel.

The reconstruction of $\phi_{\mathrm{mod},1}$ follows the same concept used for the SymNW. By modulating the signal of the respective channel 1 onto two different subcarriers using the modulation indices $h_{1,\mathrm{I}}$ and $h_{1,\mathrm{II}}$, $\phi_{\mathrm{mod},1}$ can be reconstructed unambiguously for

$$|b-1| = \left|\frac{h_{1,\mathrm{II}}}{h_{1,\mathrm{I}}} - 1\right| \leq 1 \tag{6.11}$$

as described in Section 5.5.1 using equation (5.29). This is considered in the multiplexing concept depicted in Fig 6.3 (a), wherein the first channel of each repeater modulates the signal to two neighboring sets of subcarriers. If employing DSB mixer, one could use the USB and LSB, however, this is not recommended since it leads to b=−1, which means that an unambiguous phase reconstruction is not possible. In contrast, as shown in Fig 6.3 (b), a pattern similar to Fig 6.3 (a) can be used, where the first MCR channel of each MCR modulates to two different set of subcarriers.

6.5.2 Virtual Network Array

After the correction of the modulation induced phase errors, the bistatic signals can be exploited for network-based DoA estimation. In analogy to (2.37), the phase shift of the signals transmitted by the Tx channels uth MCR and received by the radar's Rx channels equals

$$\tilde{\boldsymbol{a}}_{\mathrm{bi,sub},u} = \left(\mathrm{e}^{-\mathrm{j}2\pi\left(\tau^{\mathrm{LoS}}+\tau_u^{\mathrm{MCR}\to\mathrm{T}}+\tau^{\mathrm{T}\to\mathrm{Rx}}\right)f_{\mathrm{Tx}}}\boldsymbol{z}_{\mathrm{MCR}} \odot \boldsymbol{a}_{\mathrm{Tx,MCR}u}\right) \otimes \boldsymbol{a}_{\mathrm{Rx}} \tag{6.12}$$

assuming far field condition. The vector $\boldsymbol{z}_{\mathrm{MCR}} \in \mathbb{C}^{N_{\mathrm{Tx,MCR}}}$ accounts for the phase modulation and ToF within each repeater channel, and is assumed to be removed by calibration. The same applies to the influence of τ^{LoS}, which

is also target-independent and can be suppressed by calibration. This steering vector describes the target-angle dependent phase progression across one MCR subarray. The virtual subarray of the uth MCR therefore equals

$$\boldsymbol{d}_u = \boldsymbol{d}_{\mathrm{Tx},u} \oplus \boldsymbol{d}_{\mathrm{Rx}} \ , \tag{6.13}$$

where $\boldsymbol{d}_{\mathrm{Tx},u}$ is the Tx array of the uth MCR. Although each SA can be used for DoA estimation on its own, to exploit the networks full potential, the SAs must be combined.

In a TriNW, both the monostatic and the bistatic signal paths contain only one reflection at the target. Consequently, the SAs from the radar and the MCRs can be combined for DoA estimation. Defining the vector of the network node positions as

$$\boldsymbol{d}_{\mathrm{NW}} = \begin{pmatrix} d_{\mathrm{radar}} & d_{\mathrm{MCR},1} & d_{\mathrm{MCR},2} & \cdots & d_{\mathrm{MCR},N_{\mathrm{MCR}}} \end{pmatrix} \tag{6.14}$$

where d_{radar} equals the position of the first radar Tx antenna (reference antenna), and $d_{\mathrm{MCR},l}$ the position of the first antenna (reference antenna) of the respective MCR. Typically, the first radar antenna is used as reference within the VNA, so d_{radar}=0, and all $d_{\mathrm{MCR},l}$ are defined by the distance between the respective reference antenna of the MCR and the radar reference antenna. Consequently, the network node steering vector equals

$$\boldsymbol{a}_{\mathrm{NW}} = \begin{pmatrix} \mathrm{e}^{-\mathrm{j}\frac{2\pi}{\lambda} d_{\mathrm{NW}}[1] \sin\theta} & \mathrm{e}^{-\mathrm{j}\frac{2\pi}{\lambda} d_{\mathrm{NW}}[2] \sin\theta} & \cdots & \mathrm{e}^{-\mathrm{j}\frac{2\pi}{\lambda} d_{\mathrm{NW}}\left[N_{\mathrm{MCR}}+1\right] \sin\theta} \end{pmatrix} . \tag{6.15}$$

It should be noted that all elements of $\boldsymbol{a}_{\mathrm{NW}}$ and $\tilde{\boldsymbol{a}}_{\mathrm{bi,sub},u}$ are assumed to have magnitude 1, so any amplitude variations are corrected beforehand by amplitude normalization.

The next step is to derive the non-normalized VNA steering vector $\tilde{\boldsymbol{a}}_{\mathrm{VNA}}$, where the subarrays are combined, including the phase shifts due to the network node position from $\boldsymbol{a}_{\mathrm{NW}}$. This leads to a concatenation of the steering vectors

of all subarrays as

$$\tilde{\boldsymbol{a}}_{\mathrm{VNA}} = \left(a_{\mathrm{NW}}[1]\,\tilde{\boldsymbol{a}}_0 \;\; a_{\mathrm{NW}}[2]\,\tilde{\boldsymbol{a}}_{\mathrm{bi,sub},1} \;\; a_{\mathrm{NW}}[3]\,\tilde{\boldsymbol{a}}_{\mathrm{bi,sub},2} \;\cdots\; a_{\mathrm{NW}}[N_{\mathrm{MCR}}+1]\,\tilde{\boldsymbol{a}}_{\mathrm{bi,sub},N_{\mathrm{MCR}}}\right) \tag{6.16}$$

where $a_{\mathrm{NW}}(n)$ is the nth element of $\boldsymbol{a}_{\mathrm{NW}}$ and $\tilde{\boldsymbol{a}}_0$ the non-normalized radar steering vector. The $\tilde{\boldsymbol{a}}_{\mathrm{VNA}}$ can then be normalized by division with its reference element, which is typically its first element, resulting in

$$\boldsymbol{a}_{\mathrm{VNA}} = \frac{\tilde{\boldsymbol{a}}_{\mathrm{VNA}}}{\tilde{a}_{\mathrm{VNA}}[1]}\,. \tag{6.17}$$

From this VNA steering vector, the VNA itself is defined by the virtual subarrays shifted to the subarray positions as

$$\boldsymbol{d}_{\mathrm{VNA}} = \left(d_{\mathrm{radar}}+\boldsymbol{d}_0 \;\; d_{\mathrm{MCR},1}+\boldsymbol{d}_1 \;\; d_{\mathrm{MCR},2}+\boldsymbol{d}_2 \;\cdots\; d_{\mathrm{MCR},N_{\mathrm{MCR}}}+\boldsymbol{d}_{N_{\mathrm{MCR}}}\right)\,, \tag{6.18}$$

where $\boldsymbol{d}_0$ is the virtual array of the radar as defined in (2.47).

If all virtual subarrays are identical, i.e., $\boldsymbol{d}_n{=}\boldsymbol{d}_0$ and $\boldsymbol{a}_{\mathrm{bi,sub},n}{=}\boldsymbol{a}_0$ $\forall n = [0, 1, \cdots, N_{\mathrm{MCR}}]$, then (6.17) and (6.18) simplify to

$$\boldsymbol{a}_{\mathrm{VNA}} = \boldsymbol{a}_{\mathrm{NW}} \otimes \boldsymbol{a}_0 \tag{6.19}$$

and

$$\boldsymbol{d}_{\mathrm{VNA}} = \boldsymbol{d}_{\mathrm{NW}} \oplus \boldsymbol{d}_0\,, \tag{6.20}$$

respectively.

6.5.3 Compressed Sensing-based DoA Estimation

Based on $\boldsymbol{a}_{\mathrm{VNA}}$ and $\boldsymbol{d}_{\mathrm{VNA}}$ from (6.17) and (6.18), respectively, the DoA estimation is performed. In order to account for the typically sparse VNA consisting of multiple subarrays, an FFT-based DoA estimation algorithm enhanced by IMAT [67], [123] for the reconstruction of the gaps in the VNA is proposed. The procedure is identical to that described in Section 5.5.3.

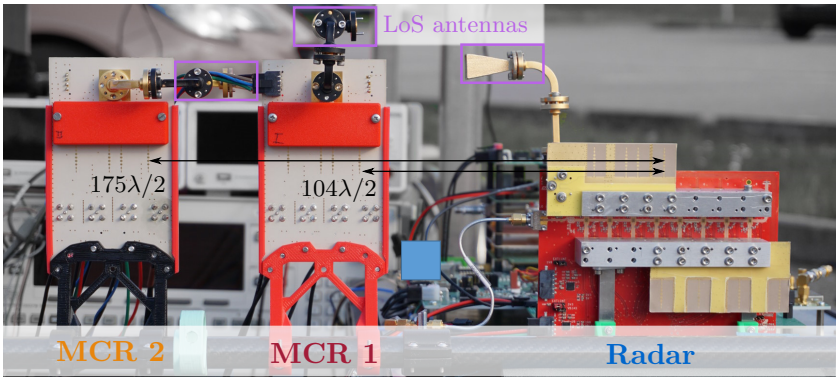

Fig. 6.4: System setup of the TriNW, including a 4×4 MIMO OFDM radar and two four-channel MCRs, fed via a LoS using horn antennas, or, in case of MCR 1, an open waveguide. Adapted from [11], CC BY 4.0 https://creativecommons.org/licenses/by/4.0/.

6.6 Measurements

The network performance is verified through measurements at 77 GHz, including the DoA estimations of multiple scenarios with one and two targets. This allows to evaluate the improvement in target angle separability compared to monostatic evaluation. Additionally, the SLL in single-target measurements is verified. All measurements are calibrated using a copper pole of 27 mm diameter placed at boresight. The calibration as well as the measurements are performed with targets at R=3.5 m.

6.6.1 Radar Network Setup

The measurement setup comprises a 77-GHz OFDM radar and two MCR's, the latter as described in Section 6.1. The OFDM radar incorporates four Rx channels, and one Tx channel, with one of the Tx channels including a power divider to feed the LoS antenna in addition to the respective Tx antenna. While for the LoS path waveguide antennas are used, all Tx and Rx channels of the radar and the MCRs use identical 8-element patch-array antennas with 15.3 dBi

Tab. 6.1: OFDM radar parameters.

Carrier frequency	f_{Tx}	77 GHz
Subcarrier spacing	Δf	100 kHz
Bandwidth	B	0.411 GHz
Number of subcarriers	N	4114
Number of OFDM symbols	M	1024
CP length	T_{CP}	0.5 μs
Range resolution	ΔR	0.364 m
Velocity resolution	Δv	0.181 $\frac{\mathrm{m}}{\mathrm{s}}$
Unambiguous range, considering FDM		68.1 m
Unambiguous velocity		$\pm$92.6 $\frac{\mathrm{m}}{\mathrm{s}}$

gain.

A photograph of the measurement setup is shown in Fig. 6.4. All MCRs are mounted on a carbon pole connected to the radar demonstrator, without an offset in the z- and y-axis. The radar and the MCRs' Tx arrays are identical, with the Tx antenna positions as well as the radar Rx array equaling the positions described in Tab. 5.1. The resulting VNA thus consists of three subarrays, with the MCRs being mounted in distances of 104 $\lambda/2$ and 175 $\lambda/2$ to the radar Tx array. Together, they form the same VNA as presented in Chapter 5 and shown in Fig. 5.12, which features an virtual aperture of 239 $\lambda/2$ and a theoretical theoretical DoA estimation resolution of 0.584° according the Rayleigh criterion [72].

The used OFDM parameters are listed in Tab. 6.1. While they are mostly identical to the parameters from Tab. 5.2, the number of OFDM symbols M differs, because in Chapter 5, M has been increased to increase integration gain due to the higher path loss of bistatic signals in SymNWs. Furthermore, N slightly differs to account for the different multiplexing patterns, since N has to be an integer multiple of Δn_{Tx}.

The modulation signals for both MCRs are generated using one eight-channel AWG. Thus, all modulation signals are coherent. The subcarrier assignment therefore slightly differs from the one presented in Fig. 6.3 (b), since only MCR 1 has a channel modulating onto two subcarriers, as shown in Fig. 6.5. An overview of the modulation frequencies is given in Tab. 6.2.

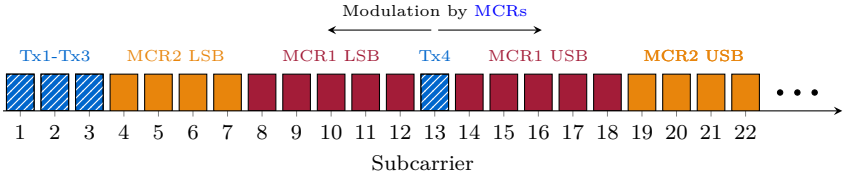

Fig. 6.5: Subcarrier assignment used in the measurements. From [11], CC BY 4.0 https://creativecommons.org/licenses/by/4.0/.

Tab. 6.2: Modulation frequencies of the MCR channels.

	MCR 1				MCR 2			
Channel	1	2	3	4	1	2	3	4
$f_{\mathrm{mod}}/\Delta f$	1 and 2	3	4	5	6	7	8	9

6.6.2 Single-Target Scenario

The first measurement includes the same 27-mm copper pole as used for calibration, positioned at a ground truth (GT) angle of $\theta_{\mathrm{GT}}{=}{-}3°$. The results of the DoA estimations are shown in Fig. 6.6, including the network-based DoA estimation with CS (—), without CS (····), and the DoA estimation using only the radar's subarray without CS (—). With the first, an angle of $\theta{=}{-}2.94°$ is estimated, well within the precision of the measurement setup. As expected, the mainlobe of the network-based DoA estimation is significantly narrower, featuring a 3-dB beamwidth of 0.39° instead of 1.72° when using the radar only. This is consistent with the expectations from Fig 5.12. Similarly, the SLL of the network-based DoA-estimation without CS equals −6.8 dB and matches the theoretical value. The single-target measurement therefore successfully shows that the performance expected from the VNA design are met.

6.6.3 Multi-Target Scenario

To further evaluate the performance improvement of the network-based DoA estimation compared to that of the 4×4-MIMO radar, the target separability

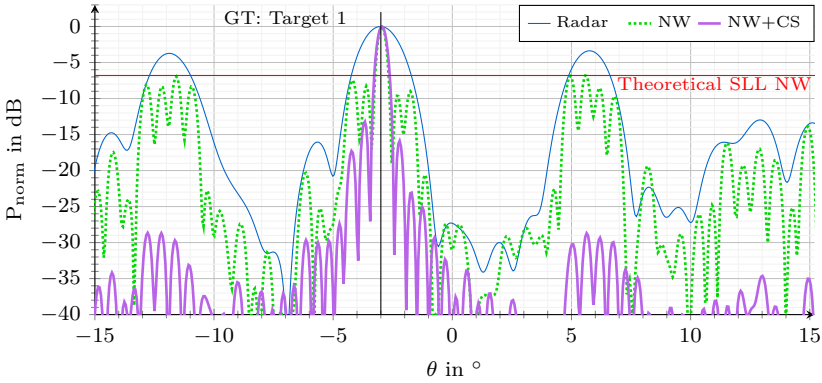

Fig. 6.6: Measurement results of a single pole placed at −3°. From [11], CC BY 4.0 https://creativecommons.org/licenses/by/4.0/.

in the angular domain is systematically analyzed. The measurement setup used consists of two aluminum poles with a diameter of 12 mm, which can be mounted in parallel at varying distances on a 1 cm grid and are placed at R=3.5 m.

The smallest spacing at which the poles can by separated by the network-based DoA estimation is 5 cm, corresponding to an angular spacing of $\Delta\theta_{\mathrm{GT}}$=0.82°. Fig. 6.7 (a) shows the DoA estimation results of this measurement. In contrast to using the radar only, the network-based DoA estimation shows two clear peaks, which are reconstructed correctly by the IMAT algorithm. The minimum between the peaks equals −3.3 dB, hence, the targets are well separated. The targets are measured at −0.2° and −0.81°, hence, the measured spacing is 0.2° lower than the ground truth. However, this is to be expected since two close peaks influence each other depending on their phases [125]. Fig. 6.7 (b) and 6.7 (c) show measurements with $\Delta\theta_{\mathrm{GT}}$=0.99° and $\Delta\theta_{\mathrm{GT}}$=1.15°, respectively. Here, the two poles are also well distinguishable. Similar to Fig. 6.7 (a), the error in Fig. 6.7 (b) equals 0.2°, while Fig. 6.7 (c) shows a very precise result with only 0.03° deviation from GT.

In addition to the network's very good performance in a two-target scenario, the measurement results also show a high consistency of the IMAT performance. Looking at the performance of the network-based DoA without CS, in all three

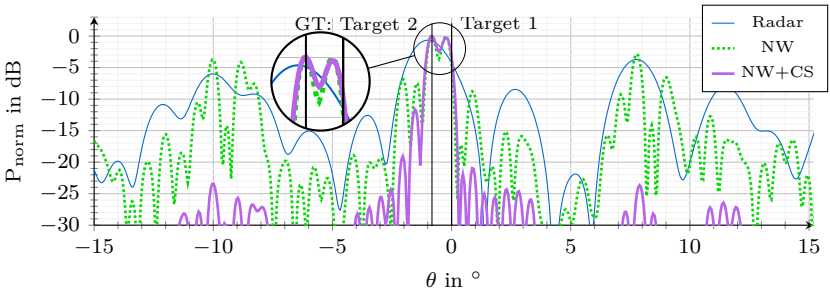

(a) GT: Δx=50 mm, $\Delta\theta_{GT}$=0.82°; measured spacing $\Delta\theta$=0.62°.

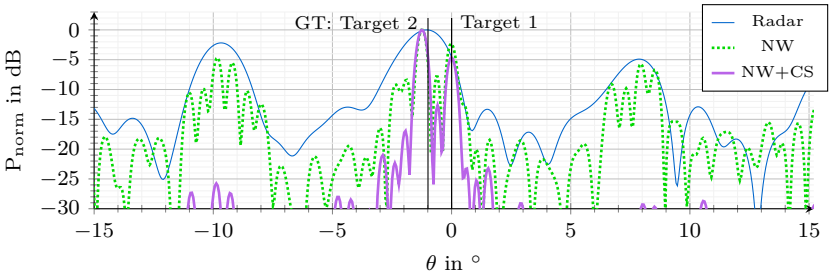

(b) GT: Δx=60 mm, $\Delta\theta_{GT}$=0.99°; measured spacing $\Delta\theta$=1.23°.

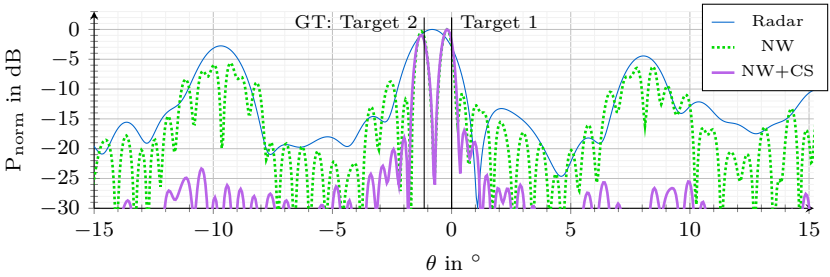

(c) GT: Δx=70 mm, $\Delta\theta_{GT}$=1.15°; measured spacing $\Delta\theta$=1.12°.

Fig. 6.7: Measurement results of two poles placed at a distance of $R = 3.5$ m with varying angular separations $\Delta\Theta_{GT}$. In (a), the poles are just about separable in the network-based DoA estimation, with a 3 dB minima between the peaks. In (b) and (c), the spacing of the targets is increased and their peaks are well separable using the network, but not using the radar only. From [11], CC BY 4.0 https://creativecommons.org/licenses/by/4.0/.

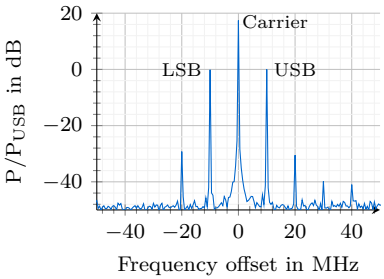

Fig. 6.8: Output spectrum of a single MCR channel with f_{mod}=10 MHz. The frequency axis equals the frequency offset to the input signal, which is a single-tone at 77 GHz.

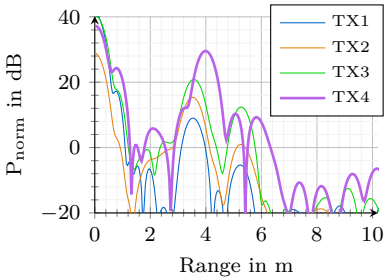

Fig. 6.9: Monostatic range profiles of a single pole at 3.5 m (same measurement as in Fig. 6.6), showing the results of different radar Tx using the same Rx channel.

measurements in Fig. 6.7 the SLLs are worse than in the single-target scenario from Fig. 6.6; they equal −2.8 dB, −4.8 dB, and −5.7 dB in Figures 6.7 (a), 6.7 (b), and 6.7 (c), respectively. However, by using IMAT they are reduced to −11.6 dB, −12.7 dB, and −16.9 dB, respectively, which is close the single-target SLL with IMAT of −13.2 dB.

6.6.4 Input Feedthrough

The system proposed in this work splits one radar Tx channel to also serve as the LoS Tx. Theoretically, the MCRs' signals should be orthogonal to the corresponding radar Tx signal, since they are shifted to different subcarriers. However, this is constrained by the limited suppression of the input feedthrough of the MCRs' mixers, i.e., the suppression of the input signal at the outputs of the MCR. The output spectrum of an MCR channel is shown in Fig 6.8 for an example of a single-tone input signal, revealing that the carrier is not suppressed but, in fact, is higher than the modulated output signal. This is because the mixers used in this work are not designed for use with high frequency in- and output and a low frequency LO; such mixers only exist in experimental studies like [126]. In a network configuration, this problem is aggravated because the unmodulated outputs of all the MCRs' channels sum up on the subcarriers used

by the LoS signal.

The impact of this effect is shown in Fig. 6.9, which shows range profiles of the measurement from Fig. 6.6 obtained using different Tx channels but the same Rx channel. In contrast to the other Tx channels, the profile of Tx4 shows a second peak behind the target peak, which is 16 dB higher and thus almost covers the target peak. In this scenario, the impact of the input feedthrough on the DoA estimation is tolerable because the main feedthrough peak is separated by range due to the longer bistatic paths. However, this may not be the case for scenarios with different geometries. It is therefore recommended that, where feasible, a dedicated radar channel is connected only to the LoS antenna, unless the MCRs have a very low input feedthrough.

6.7 Discussion

The proposed TriNW inherently combines the advantages of a radar repeater network with a dynamic range comparable to that of a monostatic radar. Disadvantages of SymNWs, such as MT propagation, are successfully avoided. Furthermore, by using MCRs instead of single channel repeaters, a high number of virtual elements in the VNA is feasible, enabling a sophisticated and flexible VNA design. Measurements verify the high performance of the TriNW-based DoA estimation, since although the network is based on a radar with only a 4×4 array, a target separability of 0.82° can be achieved while maintaining a reasonable single-target SLL of −6.8 dB before CS. Consequently, the TriNW using MCR shows great potential for high-resolution radar imaging.

However, to take advantage of these benefits, a calibratable LoS path and sufficient separation of the monostatic and bistatic signals are the keys. For the reasons mentioned above, the proposed setup does not fully meet the latter requirement. However, in the case of a less experimental, more sophisticated setup and hardware, e.g., by using custom designed repeater MMICs or a radar with a dedicated LoS Tx channel, these limitations could be overcome. Consequently, the TriNW using MCRs shows great potential for high-resolution radar imaging.

7 Assessment of Digital Radar Networks as Imaging Radar

In the previous three chapters, different concepts for radar networks have been proposed, all based on digital radars. They exploit different aspects of the opportunities provided by all-digital signal generation and processing. Nonetheless, there are substantial differences in the network configuration, signal paths, and the manner in which the proposed radar networks attain coherency. Consequently, there are distinct advantages and limitations to each. The following Chapter does provide a thorough comparison of the networks in Section 7.1, focusing on but not limited to the demands of radar imaging in automotive applications. This way, a detailed insight into the strengths and weaknesses of the different network concepts is provided, enabling the reader to select the appropriate network architecture for a given measurement task. Afterward, it is discussed which network concept is expected to be most suitable for an urban automotive scenario. Finally, in Section 7.2, the chosen network is verified by performing a variety of measurements in automotive scenarios. They focus especially on proving the network's capabilities for high-resolution radar imaging, a pivotal sensing capability for autonomous driving. Therefore, the measurements include dense multi-user scenarios involving a car, a cyclist, a pedestrian, and a motorcyclist.

7.1 Comparison of Digital Radar Networks

In order to thoroughly compare the radar network concepts, four key parameters are selected. Achieving proper **dynamic performance**, i.e., the ability to detect strong and weak targets simultaneously, is a critical performance parameter for automotive radars [12]. **Ghost targets** in the bistatic *Rv* image make a correct target peak identification utterly challenging, though this is crucial for network-based DoA estimation. The **array design** flexibility of the network

defines the optimizability of the VNA [11]. A well-optimized VNA is crucial to achieve a DoA estimation with reasonable SLL, since radar network typically feature a very sparse VNA due to the gaps between the SAs of the different sensor nodes. Finally, the **DoA estimation performance** determines the imaging capabilities of the radar network, which is compared with an emphasis on non-idealities inherent to the network concepts.

7.1.1 Dynamic Performance

The dynamic performance of OFDM and PMCW radars has been studied in great detail in [55], [127] and [41], [128], respectively. Generally, PMCW radars are typically limited by range sidelobes, i.e., a rift of sidelobes in the range profile at a strong target, whereas the main issue of OFDM radars regarding dynamic performance is their poor peak-to-average power ratio (PAPR). These findings also apply to the corresponding radar networks. However, for the proposed radar networks, the effects limiting the dynamic range of the bistatic signal evaluation are mostly of other origin, as is detailed next for Concept I to Concept III.

Uncoupled PMCW Radar Network (Concept I)

The limitation of the dynamic performance of the radar network Concept I, the CRNW, can be explained less as an Rx power limit, but as a challenge in scenarios with a high variability of peak powers. This is due to the following trade-off: On the one hand, it is shown in Section 4.4 that, for a functioning carrier recovery, the RL must always exceed the sum of all other Rx signals by at least 6 dB. On the other hand, the RL path defines the upper limit of the dynamic range of the radar network.

This effect is visualized in Fig. 7.1, evaluating the performance of the carrier recovery for different RL powers. The simulated scenario consists of an RL simulated as target at 1 m and a stationary target at 5 m. The RL Rx power P_{RL} ranges from $P_{\mathrm{RL}}{=}P_{\mathrm{Target}}$, where P_{Target} corresponds to the Rx power of the signal reflected at the target, to 80 dB above P_{Target}. Additionally, the phase noise from Fig. 4.5 (left) is applied.

Fig. 7.1 (a) shows the PNR of the target peak versus the RL power, Fig. 7.1 (b) the PSR, which corresponds to the ratio between the peak power and the noise in the velocity profile at that range, calculated as explained in Section 4.4.2. As

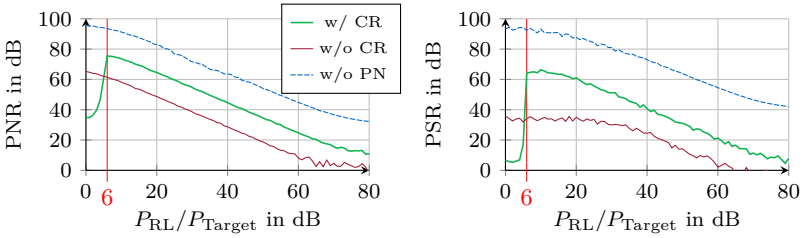

(a) PNR. **(b)** PSR.

Fig. 7.1: Dynamic performance evaluation for Concept I: Simulation results using the carrier recovery for different RL powers relative to the target peak power. The (a) PNR and (b) PSR are shown for the evaluation with carrier recovery (CR) and without carrier recovery (w/o CR). The reference (w/o PN) is simulated without phase noise and evaluated without carrier recovery. Each data point represents the average of ten simulations.

expected, P_{RL} must exceed P_{Target} by 6 dB to ensure a working carrier recovery, which is visible in both graphs of Fig. 7.1. However, increasing P_{RL} without increasing P_{Target} degrades both PNR and PSR. For the PSR, this is especially noticeable for $P_{RL}/P_{Target}>20$ dB, where the PSR converges towards the PNR, since the PSR is no longer limited by the velocity skirt of the target, but by the noise floor. Comparing the results in Fig. 7.1 (a), it is observable, that by applying the carrier recovery, the PNR is improved by 13 dB. However, it does not achieve the same PNR performance as in the reference simulated without phase noise and evaluated without carrier recovery. The limiting effect is not residual phase noise, which would also lead to significant velocity skirts at the RL and the target. Instead, this limitation is explained by the additional term consisting of a multiplication of the Rx signal with the AWGN introduced by the squaring of the Rx signal, described as Term II. in (4.23).

In summary, the dynamic performance of Concept I is significantly dependent on the RL power. The RL must cover the maximum expected target Rx power, and may hardly be adjusted if the target Rx power fluctuates. While this leads to a limitation that is potentially manageable in controlled environments, such as multistatic measurements with unmanned aerial vehicles (UAVs) and industrial applications, it is a significant drawback in uncontrollable automotive scenarios

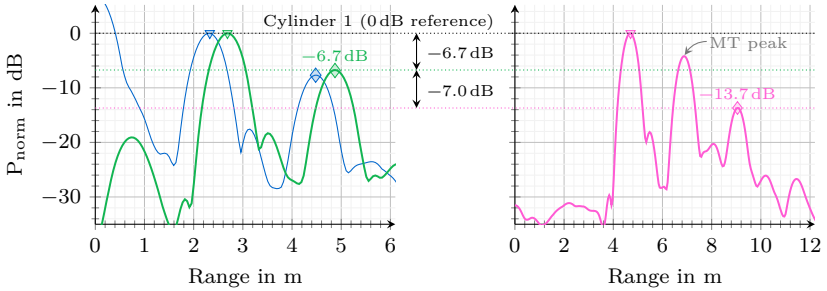

Fig. 7.2: Dynamic performance comparison for Concept II and Concept III: The range profiles of measurements of two cylinders, cylinder 1 (▽) at 2.1 m and cylinder 2 (◇) at 4.2 m, are shown, captured using the TriNW (—), the SymNW (—), and the monostatic radar measurement (—). For each, all channels of the radar or repeater are summed up in magnitude[1]. Every range profile is individually normalized to the respective peak power of Cylinder 1. For the SymNW, the doubled path via the target leads to doubled peak ranges.

—In the latter, the radar network must handle scenarios with high RCS targets nearby, such as trucks, but also scenarios with only low RCS targets, such as pedestrians.

Radar-Repeater Networks (Concept II & Concept III)

Comparing the radar-repeater networks with a monostatic radar measurement, two main factors determine their difference in dynamic range: The loss caused by the path from the radar Tx to the repeater, and the gain of the repeater hardware. The former differs significantly between Concept II, the SymNW, and Concept III, the TriNW.

According to the radar equation, the loss of a signal path via a target with an RCS σ located at range R equals

$$L_{\text{radar}}(R) = G_{\text{ant}}^2 \frac{\lambda^2}{(4\pi)^3 R^k} \sigma, \tag{7.1}$$

[1] Radar and TriNW without Tx4.

where G_{Tx} and G_{ant} are the antenna gains of the Tx and Rx antennas, respectively. The exponent k depends on the target, theoretically being 4 for point targets, and 2 for extended targets. For an ST peak, the signal travels the same path to the repeater as from the repeater Tx to the radar Rx. Thus, w.l.o.g. assuming the repeater antennas to be identical to the radar antennas, and neglecting differences in the mono- and bistatic range and in the angle-dependent RCS, the overall loss of the bistatic path equals

$$L_{\mathrm{snw}}(R) = G_{\mathrm{RP}} L_{\mathrm{radar}}^2(R) \tag{7.2}$$

resulting in an $1/R^8$ dependency for point targets, and an $1/R^4$ dependency for extended targets. Thus, the additional loss scales with the range, making it difficult to compensate for with amplifiers at the repeaters. Since further the gain on the repeater is limited to avoid self-oscillation due to feedback paths via bond wires and the repeater antennas, ranges of more than 10 meters are hardly to be expected for a SymNW.

In contrast, in a TriNW the repeater or MCR receives the signal via a LoS path, introducing an additional range-independent loss of

$$L_{\mathrm{LoS}} = G_{\mathrm{ant,LoS}}^2 \frac{\lambda^2}{(4\pi)^2 \, {d_{\mathrm{LoS}}}^2}, \tag{7.3}$$

and an overall bistatic path loss of

$$L_{\mathrm{tnw}}(R) = G_{\mathrm{RP}} L_{\mathrm{LoS}} L_{\mathrm{radar}}(R). \tag{7.4}$$

Since L_{LoS} is target range independent, and typical $d_{\mathrm{LoS}} \ll R$, L_{LoS} can be compensated for by means of the repeater gain G_{RP}, allowing a dynamic performance comparable to a monostatic radar.

The squared range-dependent loss of the SymNW in comparison to the TriNW and the monostatic radar evaluation is demonstrated in Fig 7.2. The figure shows the range profiles obtained by measurements of two identical cylinders at 2.1 m and 4.2 m. In case of Concept III (TriNW), the peak of the second cylinder exhibits an attenuation of 6.7 dB relative to the peak of the first cylinder. This is analogous to the monostatic radar measurement. In contrast, using Concept II (SymNW) this attenuation equals 13.7 dB, corresponding to the squared increase in attenuation compared to the TriNW.

Conclusion

The dynamic requirements for automotive scenarios can be summarized as follows: First, the link budget of the radar network must be sufficient to allow for a detection of weak targets; Second, the radar network must allow for a wide variety in backscatter strengths; Third, the dynamic range must be sufficient to detect weak targets in the presence of strong targets, such as a pedestrian next to a vehicle.

The bistatic detection of weak targets is severely degraded when using the SymNW, especially at higher ranges. On the other hand, when using the PMCW radar network, the required RL limits the dynamic range. Both limitations do not apply when using the TriNW, where a dynamic performance comparable to a monostatic radar is given.

7.1.2 Ghost Targets

One of the main aspects that aggravate a proper identification of the targets in the bistatic *Rv* images are ghost targets inherently caused by the radar networks. For Concept I (CRNWs), these ghost targets are caused by carrier recovery, and for Concept II (SymNW), they are due to MT propagation, as explained in Sections 4.4.1 and 5.3.4, respectively. Nevertheless, ghost targets can also occur when using Concept III (TriNW), caused by ICI and the subsequent non-orthogonalities between the monostatic and bistatic signals.

To allow for a fair comparison despite the hardware differences between the different radar network systems available, simulations of an urban traffic scenario are used as benchmark. The simulation thereby allows the use of similar radar parameters for each of the networks, which are summarized in Tab. 7.1. The investigated scenario shown in Fig. 7.3 (a) includes an intersection with two moving cars, each simulated using several reflection points, and a stationary pedestrian, who is a weak target compared to a vehicle but crucial to detect, especially when standing at a crosswalk. The scene is observed by the radar network from the perspective of the car at the bottom of the figure.

PMCW Radar Network with Carrier Recovery (Concept I)

Analyzing the simulation results in Fig. 7.4, three sources of ghost targets can be identified in Fig. 7.4 (b) compared to 7.4 (a). First, the Doppler shifts of the

Tab. 7.1: Radar parameters used for the ghost target comparison.

Parameter		CRNW	SymNW	TriNW	TriNW, meas.
Carrier frequency	f_{Tx}	77 GHz	77 GHz	77 GHz	77 GHz
Bandwidth	B	1 GHz	1 GHz	1 GHz	0.4 GHz
Observation time	T_{obs}	11.3 ms	11.3 ms	10.8 ms	10.8 ms
Code length/subcarriers	N	4008	10010	10010	4114
Code repetitions/OFDM symbols	M	2820	1024	1024	1024
Range resolution	ΔR	0.15 m	0.15 m	0.15 m	0.36 m
Velocity resolution	Δv	0.17 $\frac{\mathrm{m}}{\mathrm{s}}$	0.18 $\frac{\mathrm{m}}{\mathrm{s}}$	0.18 $\frac{\mathrm{m}}{\mathrm{s}}$	0.18 $\frac{\mathrm{m}}{\mathrm{s}}$

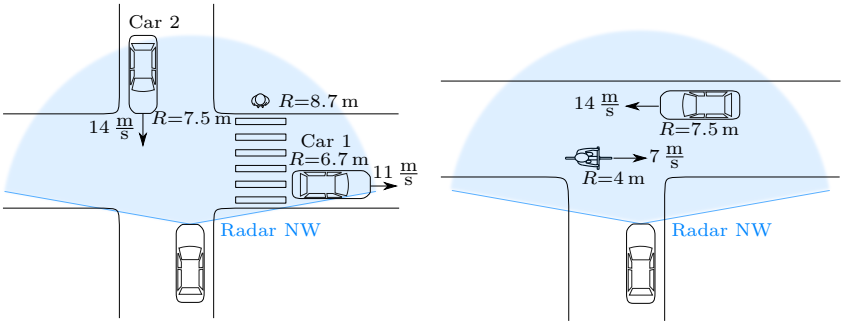

(a) Simulation scenario. **(b)** Measurement scenario.

Fig. 7.3: Automotive scenarios for ghost target comparison.

peaks at $v \neq 0$ affect the autocorrelation properties of the code sequences, leading to artifacts at $v=0$m/s as well as along the range profiles at the velocities where target peaks occur. The effect is present in both, the phase-noise-free reference simulation in Fig. 7.4 (a) as well as the bistatic simulation with carrier recovery in Fig. 7.4 (b). This is an inherent problem of PMCW radars, and can be reduced by code diversity [128]. Second, ghost targets are induced by the carrier recovery, specifically, by a recovery of additional carriers based on target peak responses. This effect is described in detail in Section 4.4, and explains the ghost targets mainly visible at $R \approx 1$ m and $v \approx \pm 20$m/s in Fig. 7.4 (b). Third, in Fig. 7.4 (b), target peaks mirrored at $v=0$ are visible, indicating a slight IQ-imbalance in the carrier recovery. However, despite the existence of carrier-recovery-induced ghost

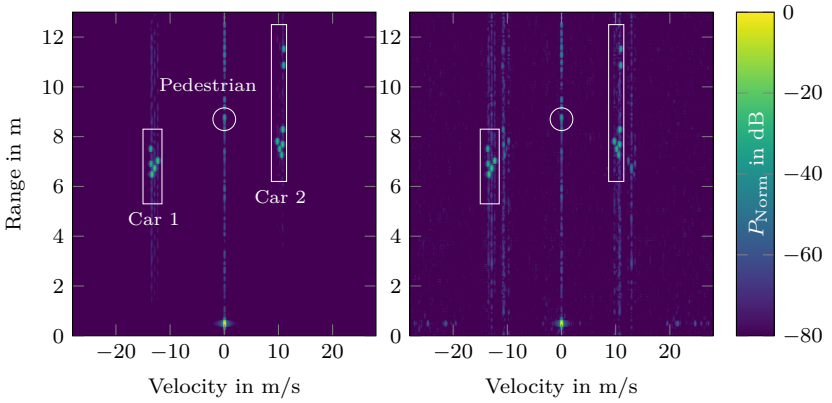

(a) Reference. **(b)** With carrier recovery.

Fig. 7.4: Ghost target evaluation for Concept I: Comparison of the *Rv* images showing the simulation of the scenario from Fig. 7.3 (a). (a) Reference, phase-noise-free and without carrier recovery; (b) Bistatic, with phase noise and SFO, evaluated with carrier recovery. Both plots are normalized to their maximum, i.e., the RL.

targets, the dominant sources of ghost targets when using a CRNW are the aforementioned Doppler-induced correlation errors typical for PMCW radars.

Symmetrical-Path Radar-Repeater Network (Concept II)

The most common cause of ghost targets in a SymNW is MT propagation, i.e., signal paths with reflections at different targets on the way to the repeater and back. As explained in Section 5.3.4, they give rise to additional peaks in between every two ST peaks. The effect can be observed in Fig. 7.5, which shows in Fig. 7.5 (a) monostatic and in Figs. 7.5 (c) and (e) bistatic simulation results of the scenario from Fig. 7.3 (a). While all targets are clearly identifiable in the monostatic *Rv* image, the bistatic *Rv* images are severely affected by MT peaks. Note that bistatic ST peaks are at twice the range and velocity compared to the monostatic peaks.

Comparing Figs. 7.5(c) and (e), however, further ghost targets appear. These

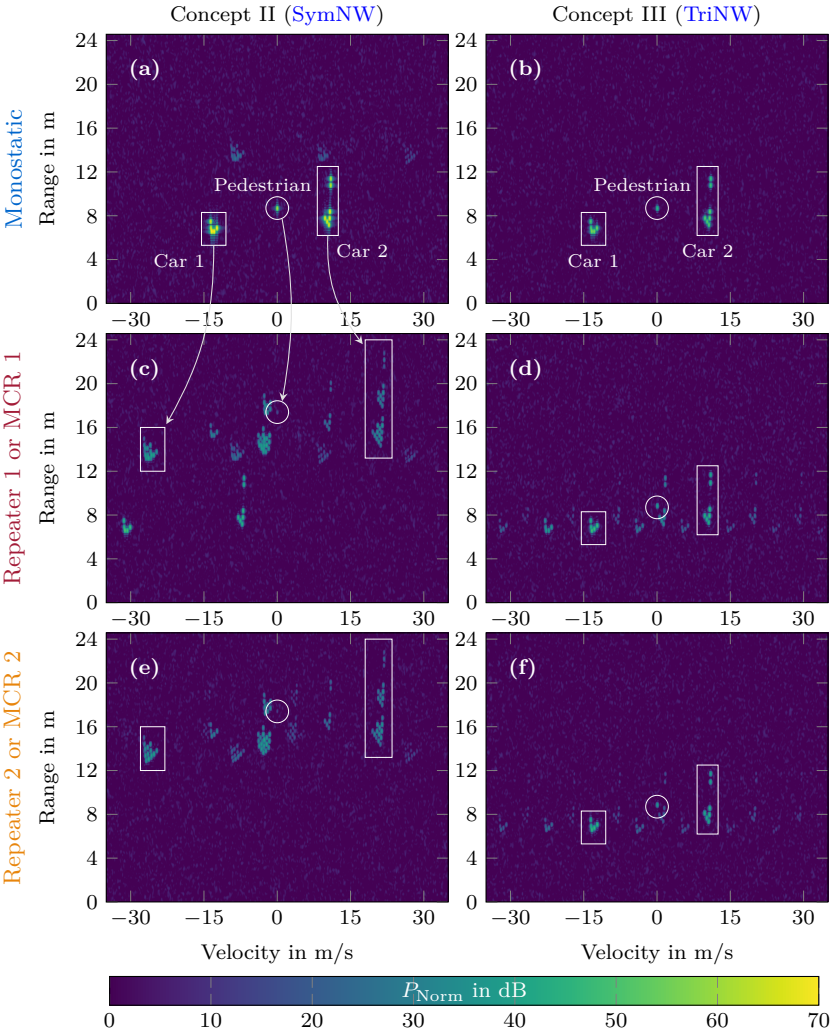

Fig. 7.5: Ghost target evaluation for Concept II and Concept III: Comparison of the *Rv* images obtained by different network nodes in a SymNW (left) and a TriNW (right). The scenario shown in Fig. 7.3 (a) is simulated; all plots are normalized to their noisefloor.

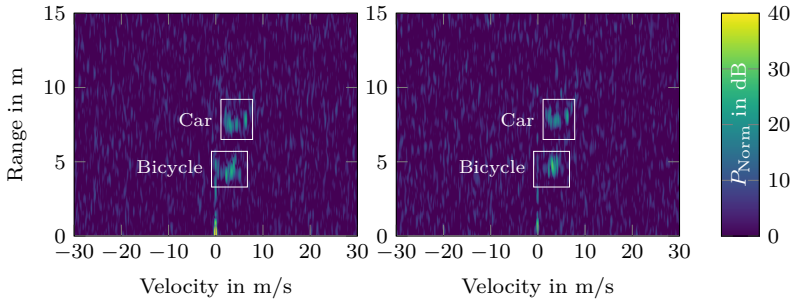

(a) Monostatic **(b)** MCR 1

Fig. 7.6: Measurement results of the scenario shown in Fig. 7.3 (b) using Concept III (TriNW).

are caused by ICI. While ideally, all subcarriers of OFDM signals are orthogonal, any Doppler shifts lead to ICI [55], [59]. Usually, adjacent subcarriers are coded differently, thus, ICI does not lead to a ghost target but to an increased noise floor. In contrast, the frequency shift of a repeater leads to multiple adjacent subcarriers being coded identically, so ICI in between them causes ghost targets. This is best visible in Fig. 7.5(c), showing the *Rv* image of a bistatic channel with subcarriers directly adjacent to monostatic subcarriers, so the ICI causes a spill-over of monostatic peaks into the bistatic *Rv* image. Their velocity shift is induced by the CP correction from Section 5.3.2. In addition, the monostatic *Rv* image is affected by ICI-induced ghost targets, but their power is significantly lower due to the low power of bistatic signals in a SymNW. As shown in [73] by the author, it is possible to mitigate ICI-induced ghost targets by using RP-OFDM in combination with All Cell Doppler Correction (ACDC) [59]. However, this comes at the cost of a higher susceptibility to ICI induced by hardware impairments due to the lack of code diversity.

Triangular-Path Radar-Repeater Network (Concept III.)

The latter radar repeater network, the TriNW, is not affected by MT peaks. Thus, all appearing ghost targets are ICI-induced and correspond to the aforementioned ICI-induced ghost targets in SymNWs. In contrast, they do not appear in the

monostatic *Rv* images. Furthermore, their power is significantly lower compared to the bistatic peak power in a SymNW. This is explained by the Doppler shifts in a SymNW being twice as high due to the doubled reflection at the targets.

In measurements with the radar network demonstrator from Chapter 6, these ghost targets are not detected at all. This can be observed in Fig. 7.6, which depicts the results of a measurement of a bicycle and a car traversing the radar network in opposing directions. In the *Rv* images, both targets are discernible, including multiple reflection points, without ghost targets above noisefloor. A plan of the scenario is provided in Fig. 7.3 (b).

7.1.3 Array Design

High flexibility in the placement and design of a network's subarray is crucial for the design of a proper VNA—and thus for managing the balancing act between a high target separability in the DoA estimation, i.e., a large VNA, and an SLL low enough for a correct detection of weak targets using CS. The relationship between VNA design and DoA estimation performance is mathematically described based on the VNA-dependent angular spectrum, as first introduced in [11] by the author. The angular spectrum $\mathbf{A}(\Psi)$ is defined as Fourier transform of the steering vector corresponding to a target at angle θ:

$$\mathbf{A}(\Psi) \propto \underbrace{\delta(\Psi - \Psi_\theta)}_{\text{target angle}} * \underbrace{\underbrace{W\left(\Psi \frac{l_{\text{sub}}}{2}\right) \mathrm{e}^{-\mathrm{j}\Psi \frac{l_{\text{sub}}}{2}}}_{\text{subarray}} \underbrace{\left(\sum_{k=1}^{N_{\text{NW}}} \mathrm{e}^{-\mathrm{j}\Psi d_{\text{NW}}[k]}\right)}_{\text{node position}}}_{=V(\Psi),\ \text{VNA function}}. \tag{7.5}$$

Its complete mathematical derivation is given in Appendix C. It is composed of a Dirac delta function $\delta(\Psi - \Psi_\theta)$ corresponding to the target angle, and a VNA function $V(\Psi)$, describing the peak shaping due to virtual antenna positions within the VNA. In a radar network, $V(\Psi)$ comprises the subarray functions $W(\Psi)$ of each SA and the position of each subarray. W.l.o.g. equal subarrays, i.e., identical $W(\Psi)$ for each SA, as well as virtual antennas in a $\lambda/2$ grid and a subarray size of $l_{\text{sub}}\lambda/2$ are assumed. Here, l_{sub} corresponds to the distance between first and last virtual antenna, regardless of sparsity. Since the VNA function acts as shaping function convolved with the Dirac, it defines target

separability and SLL, and thus a proper VNA is crucial for a well-performing radar network. Thereby, $W(\Psi)$ corresponds to the peak shape when using only one subarray, and in the network context acts as envelope of $V(\Psi)$.

In the following, the influence of $V(\Psi)$ is shown with several examples, all are using a VNA of size $239\lambda/2$ composed of 16-element subarrays. For each example, the VNA and the angular spectrum of a target at $\theta{=}0°$ are depicted in Fig. 7.7. To start with, the angular spectrum of a VNA consisting of two 16-element ULAs shown in Fig. 7.7 (a) is analyzed. Mathematically, the absolute value of the angular spectrum of such a constellation corresponds to

$$\left|\mathbf{A}(\Psi)\right| \propto \delta(\Psi-\Psi_\theta) * \left|\mathrm{si}\left(\Psi\frac{l_{\mathrm{sub}}}{2}\right)\right| \sqrt{2\cos\left(\Psi d_{\mathrm{NW}}[2]\right)+2}, \tag{7.6}$$

as derived in Appendix C. The VNA function is defined by the sinc function $\mathrm{si}(\Psi\, 0.5 l_{\mathrm{sub}})$ corresponding to the rectangular sampling pattern of the subarrays and the cosine function resulting from the node position-induced exponential terms in (7.5). The latter leads to a main peak narrowed in dependence of the distance between the network nodes, i.e., the VNA size, but also results in numerous peaks within the sinc envelope and thus in a lot of sidelobes with a potentially devastating SLL. This can be seen in Fig. 7.7 (a), where the SLL of 0.2 dB makes the VNA barely usable.

Improvement is achieved by increasing the number of subarrays. In this way, the node position induced part of $V(\Psi)$ from (7.5) is formed by the superposition of multiple exponential functions, and by a proper positioning of the SAs, they interfere destructively at the sidelobes. In the example shown in Fig. 7.7 (b), this allows to reduce the SLL to -1.9 dB by choosing the position of the middle SA that results in the lowest SLL. The importance of the position of the additional SAs becomes evident by juxtaposing Fig. 7.7 (b) with the VNA shown in Fig. 7.7 (c) consisting of four SAs, but the middle two being centered. The latter is a typical configuration for radar networks consisting of two MIMO radars, with two outer monostatic subapertures and two bistatic ones in between, like used in [8]. Although the VNA contains more virtual antennas than the VNAs in Fig. 7.7 (b), the SLL is very high at -0.7 dB.

To further improve the SLL, sparse SAs can be used, which improves the ratio between l_{sub} and the gaps between the SAs. This is visible in Fig. 7.7 (d),

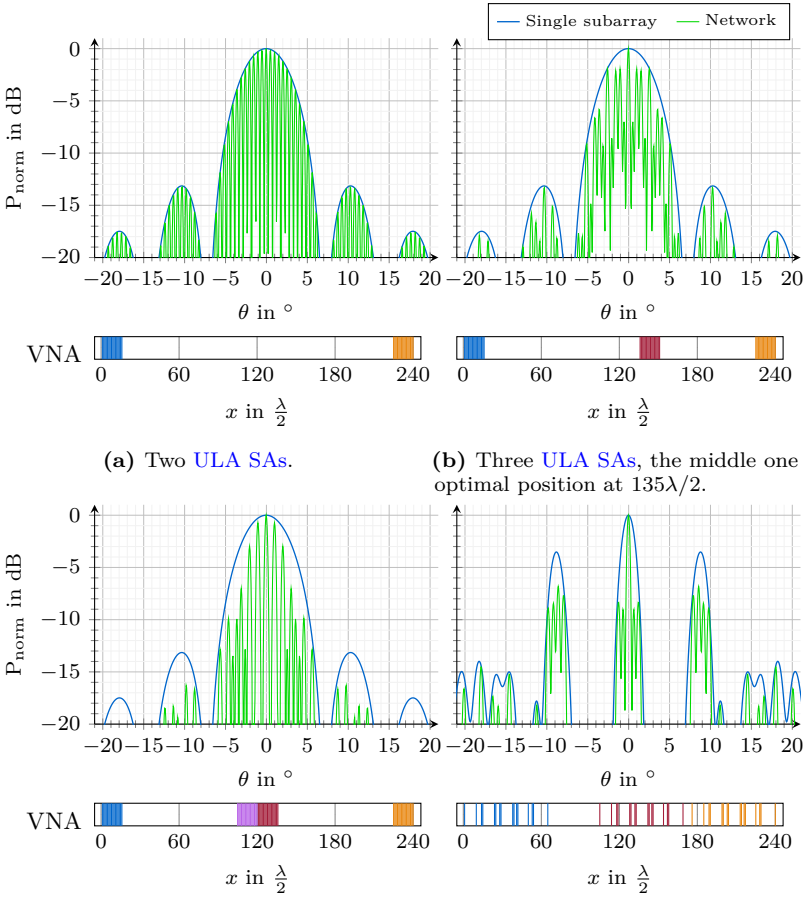

(a) Two ULA SAs.

(b) Three ULA SAs, the middle one the optimal position at $135\lambda/2$.

(c) Four ULA SAs, corresponding to a network of two 4×4 MIMO radars.

(d) Three sparse SAs.

Fig. 7.7: Simulation of the angular spectrum for a target at θ=0° using different VNAs, evaluated with ZP to eight times the VNA length. All VNA are based on 16-element SAs and have a size of $239\lambda/2$. (a), (b), and (d) are adapted from [11], CC BY 4.0 https://creativecommons.org/licenses/by/4.0/.

which shows the angular spectrum using a VNA incorporating three sparse SAs of size $l_{\text{sub}} = 65\lambda/2$. An SLL of $-6.8\,\text{dB}$ is achieved, which is outstanding for a radar network and more than adequate for a DoA estimation with CS.

Network Requirements & Comparison

From the mathematical representation in (7.5) and in accordance to the examples presented in Fig. 7.7, the requirements for a network concept are concluded as:

1. The network should allow for multiple, at least three, SAs ;
2. The SAs should be positionable in a flexible manner in order to reduce the SLL by means of a destructive interference of the node position-induced exponential terms in $V(\Psi)$;
3. It should be possible to create sparse SAs to facilitate a better virtual antenna distribution in the VNA.

These requirements are met to varying degrees by the different network concepts. While for the CRNW, no DoA estimation is presented, it leads to a network of synchronized MIMO radars. The VNA is independent of signal modulation and synchronization method, thus, is as analyzed in detail using FMCW radars in [8], [74], [87]. It allows for large number of SAs, since each pair of Tx and Rx array, either from the same radar node or from different ones, leads to an SA. However, the flexibility of SA positioning is limited, since the bistatic SAs will always sit in between the monostatic SAs of the corresponding MIMO radars, typically in the center. This yields configurations like the one exemplarily shown in Fig. 7.7 (c), which is not optimal for sidelobe suppression.

In contrast, the repeater in a SymNW can be placed arbitrarily, offering a high degree of freedom in VNA design. The only restriction is that all SAs are inherently identical. The former also applies for the TriNW from Chapter 6, where MCRs can be placed arbitrarily provided that the LoS path is preserved. However, they also allow for different SAs within the network, since each MCR's Tx array can be different, thus offering the highest array design flexibility among the proposed network concepts.

7.1.4 DoA Estimation Performance

Improving DoA estimation capabilities is one of the main motivating factors for employing radar networks, especially in an automotive context [74]. In the

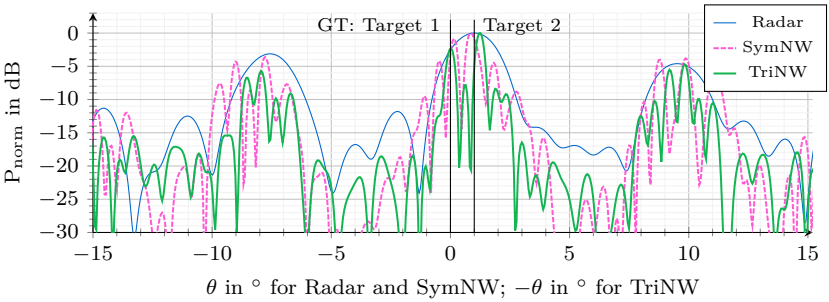

Fig. 7.8: DoA estimation comparison Concept II (SymNW) and Concept III (TriNW): Measurement results of two poles in a 1 degree spacing from Fig. 5.14 (radar and SymNW) and Fig. 6.7 (b) (TriNW). To compare the DoA estimation performance before sidelobe suppression, no CS is applied.

following, the DoA estimation performance of the two radar-repeater networks, Concept II (SymNW) and Concept III (TriNW), are compared in detail. Concept I (CRNW) is not included in the comparison due to the limitation of the single-input single-output (SISO) PMCW radar demonstrator.

In single-target cases, specifically, DoA estimations of a single target in an *Rv* cell, main performance indicator is the accuracy of the estimation of a target's angle. The main influences are the SNR [61] and the precision of the network setup like the sensor node placement, making a fair comparison using measurements difficult due to the limited network setup precision. However, two important points are worth noting: First, any positioning error, i.e., an error in $\boldsymbol{d}_{\mathrm{NW}}$, results in a phase error twice as high when using a SymNW compared to a TriNW. This is due to the factor of 2 in (5.34) resulting from the SymNW signal being reflected twice at the target. Second, the SymNW typically has a significantly lower bistatic SNR, as demonstrated in Fig 7.2, which also affects DoA estimation accuracy. Therefore, the TriNW is expected to have a better DoA estimation performance in the single-target case.

In the multi-target case, using the SymNW the DoA estimation is inherently affected by MT propagation, as explained in 5.6.4. In contrast, the TriNW does not suffer from MT propagation, resulting in a much better performance. This can be seen in Fig. 7.8, which compares the measurements results of two targets

Tab. 7.2: Comparison of the proposed radar network concepts.

	CRNW	SymNW	TriNW
Dynamic performance	-	- -	+
Ghost Targets	+	-	○
Array Design	○	+	+ +
DoA Performance	N/A	-	+

offset by $\approx 1°$. Here, the DoA estimation is performed without CS to juxtapose the performance of the networks before sidelobe suppression. While TriNW allows a correct estimation of the angles of both targets, using the SymNW produces three peaks, including an additional peak caused by MT propagation.

7.1.5 Conclusion

Based on the analysis and comparison of the three radar networks proposed in this thesis, the TriNW achieves the best overall performance in automotive applications, as also summarized in Tab. 7.2. The SymNW has significant issues with the Rx power of the bistatic signal, and the assessment of its bistatic signal is significantly impaired by ghost targets resulting from MT paths. The CRNW promises low susceptibility to ghost targets and a good performance in controlled scenarios. However, for measurement tasks with a high fluctuation of target RCS, an RL with a high back-off needs to be chosen, though, this affects the detectability of weak targets. In contrast, the TriNW enables a dynamic range that is comparable to that of the monostatic radar evaluation. It allows for the highest flexibility in VNA design, and demonstrates excellent DoA estimation performance within the laboratory setting of an anechoic chamber. Thus, in the next Section, the TriNW using MCR is further verified by demonstrating its radar imaging capabilities in various automotive scenarios.

7.2 Digital Radar Network as Automotive Imaging Radar

To properly demonstrate the radar imaging capabilities of the TriNW in automotive scenarios, measurement results of different scenarios including a car, a pedestrian, a motorcycle, and a bicycle are shown. For the measurements, the radar network demonstrator shown in Fig. 6.4 is assembled in a parking lot. The

antennas are located at 55 cm (Tx and MCR) and 44 cm (Rx) above ground. Together, the radar and the two MCRs form the VNA shown in Fig. 7.7 (d). The parameters correspond to the ones shown in Tab. 6.1, lacking a high range resolution due to bandwidth limitations of the available OFDM radar demonstrator. Several steps are performed to generate a Cartesian plot, i.e. a bird's eye view of the scene, based on the radar network measurement: First, range and velocity shift in bistatic *Rv* images due to LoS range and f_{mod} deviations causing velocity offsets are corrected. At each range, the velocity bin with the maximum power is selected. Then, for each *Rv* bin determined this way, a DoA estimation is performed, which is weighted in the Cartesian plot by the corresponding *Rv* bin amplitudes. The DoA estimation includes a near-field correction, adapting the method presented in [122], and CS using the IMAT algorithm. It should be noted that this processing may result in sharp edges of the target peaks in case the IMAT algorithm detects a target in one range cell, but suppresses it at the next range.

7.2.1 Target Feature Detection

The first measurements presented include scenarios with one or two separate road users, as shown in the top row of Fig. 7.9 (a). They aim to show the ability of the network to image the road users in great detail. In particular, the high resolution of the DoA estimation is expected to allow the detection of multiple features, i.e., reflection points, per road user.

The first scenario is a cyclist at 5 m distance from the radar network. In the result obtained by the radar network, visible in Fig. 7.9 (a) (center), the front of the bicycle is shown in great detail. The left fork tube is recognizable, as is the fork head tube. In addition, the rider's straight leg is visible as a distinct peak. While the right fork tube is not detectable as a clear peak, the measurement result still shows a weak peak at the expected location that merges into the peak from the leg. In contrast, using only the radar, the bicycle is only visible as a single peak, see Fig. 7.9 (a) (bottom). Here the aforementioned sharp edge in the target peak, which is caused by the algorithm IMAT, is also visible. The next scenario employs a motorcycle approaching the radar. The Cartesian plot in Fig. 7.9 (b) (center) obtained via the network-based DoA estimation reveals a large number of features, including distinct reflections from the fork, engine, and

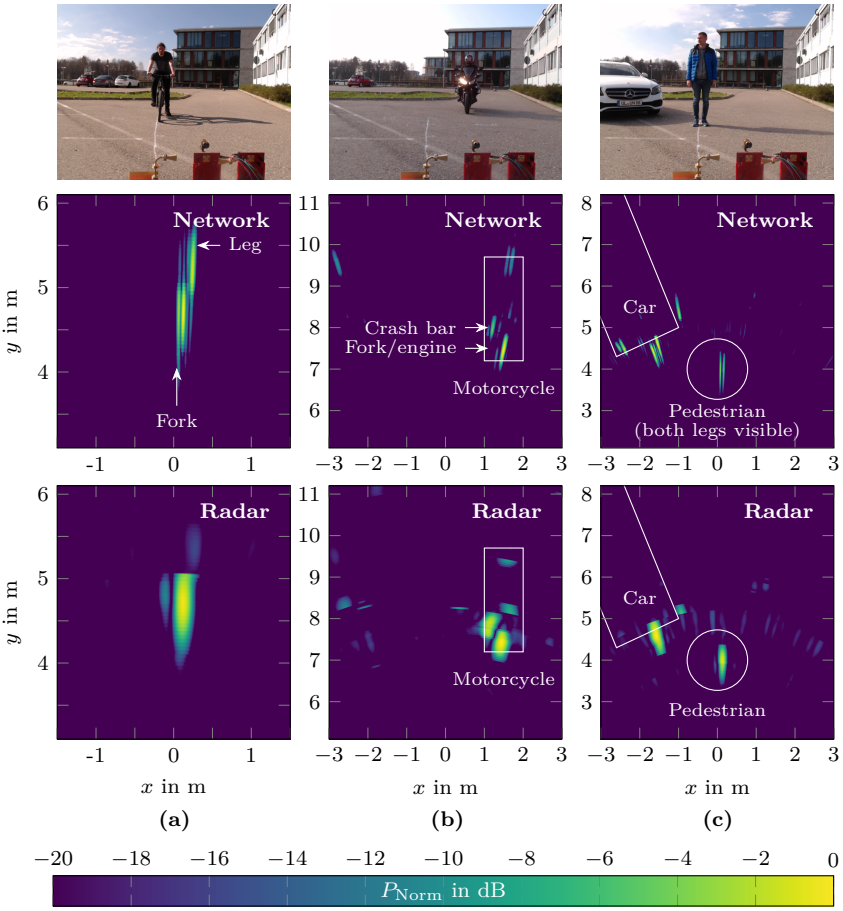

Fig. 7.9: Measurement results of automotive scenarios with a single road user or two road users placed apart; (a): cyclist; (b): motorcycle approaching the radar; (c): car and pedestrian; as shown in the photographs (top). For each measurement, the Cartesian plots obtained by using the radar network (center) and using only the radar (bottom) are compared. Partly adapted from [11], CC BY 4.0 https://creativecommons.org/licenses/by/4.0/.

crash bar. In contrast, as visible in Fig. 7.9 (b) (bottom), significantly less details are obtained using the radar only. In Fig. 7.10 (c), measurement results of a scenario including two road users, a car and a pedestrian, are shown. In contrast to the result using the radar only (bottom), the TriNW (center) captures both road users in great detail, e.g., showing both legs of the pedestrian.

In summary, the radar network demonstrates a high potential for radar imaging of traffic participants. Particularly, by detecting a high number of features per road user, target classification becomes feasible [7].

7.2.2 Differentiation between Road Users

Next, multiple road users are placed close to each other, typical for urban automotive scenarios. This includes a combination of weak targets, such as pedestrians and cyclists, and strong targets, such as cars and motorcycles. The challenge is to detect both strong and weak targets, especially when they can only be separated by their angle.

The first example is a measurement of a car, a pedestrian, and a bicycle placed side by side, shown in Fig. 7.10 (a) Using the radar network, both, the car and the bicycle, are detected in great detail, as shown in Fig. 7.10 (a) (center). In addition, the pedestrian, despite being at the same range as the car and not detected by radar alone, is well visible. In contrast, using the radar only, the pedestrian is not detected, as visible in Fig. 7.10 (a) (bottom). The outstanding performance of the radar network also is visible in Fig. 7.10 (b), where the same road users are placed even closer together. Although the target peaks of the pedestrian are weak and some features of the bicycle are missing, the radar network is able to detect all of them. Using the radar, way fewer details are obtained, see Fig. 7.10 (b) (center) and (bottom), respectively. In Fig. 7.10 (c), the bicycle and the motorcycle are placed handlebar to handlebar, with only 0.8 m from center to center. Yet again both are detected by the radar network in great detail, whereas the with the radar, only one peak for each is obtained, see Fig. 7.10 (c) (center) and (bottom), respectively.

In summary, these measurements demonstrate the ability of the network-based DoA estimation with CS to detect a weak target, including its detailed features, in the presence of a strong one.

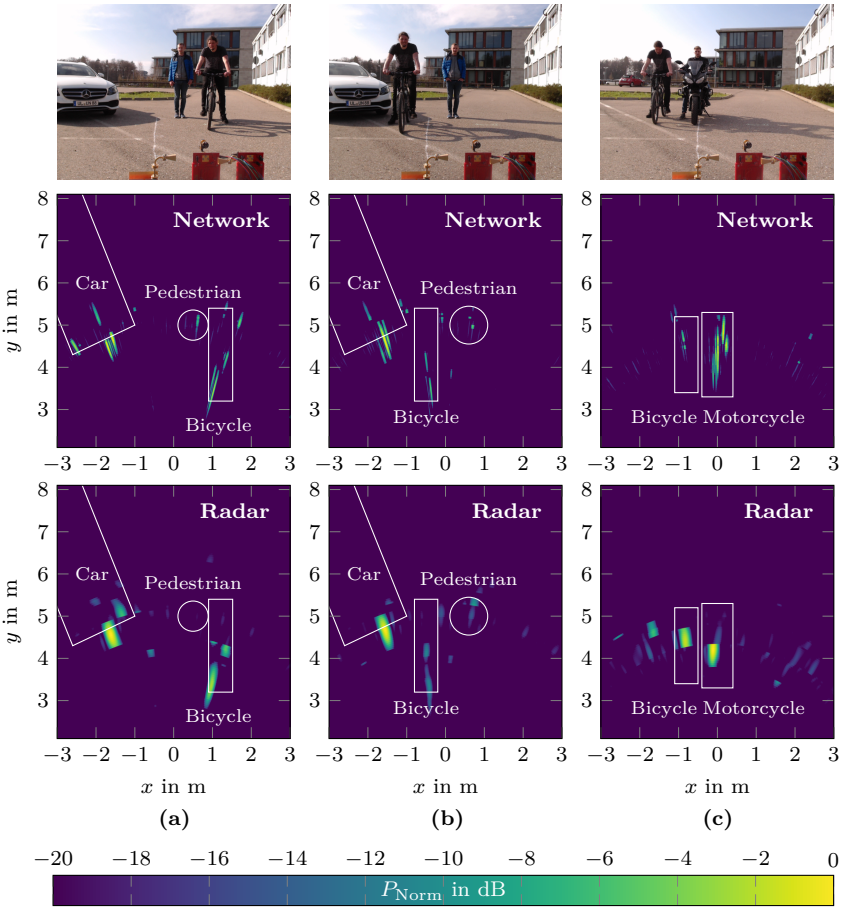

Fig. 7.10: Measurement results of multiple road users spaced closely; (a) and (b): car, pedestrian, and bicycle; (c): bicycle and motorcycle; as shown in the photographs (top). For each measurement the Cartesian plots obtained by using the radar network (center) and using only the radar (bottom) are compared. Adapted from [11], CC BY 4.0 https://creativecommons.org/licenses/by/4.0/.

8 Conclusion

In recent years, automotive radars are developing from detecting single targets to obtain image-like sensing of the surroundings. This way, other road user can be detected in great detail, facilitating their classification. However, this requires a high-resolution DoA estimation, which in turn necessitates the use of very large apertures. While the design of ever larger radar sensors achieves these goals, due to their sheer size, their potential is limited by the space available in vehicles. This limitation is overcome by coherent radar networks: Combining monostatic and bistatic subapertures for a network-based DoA estimation, the extended aperture of the network can be exploited, promising radar imaging capabilities. Still, each sensor node within the network can be kept small, facilitating integration, i.e., in vehicles, and reducing costs. The kind of radar network providing the highest flexibility are uncoupled radar networks, where no synchronization signal is distributed via cables—yet, this also makes them the most challenging radar networks to synchronize. While the synchronization and multiplexing capabilities of analog FMCW radars are constrained by their limited flexibility in signal design and processing, digital radars have already shown the potential to overcome these limitations in areas such as interference mitigation and joint communication and sensing.

This thesis extends the state of the art by presenting the first uncoupled fully-coherent radar networks based on digital radars, demonstrating the potential of a digital radar's highly flexible signal design and processing for radar networks. It is shown that digital radars offer a whole new set of possibilities to solve the key challenges of radar networks, synchronization and multiplexing. The first key objective of this thesis, specifically to propose and investigate different concepts for radar networks based on digital radars, is fulfilled by introducing different network concepts using either single-carrier or multi-carrier signals. Three different radar networks based on PMCW and OFDM radars are presented, exploiting different aspects of the flexible signal design and processing capabilities provided by a digital radar.

The first, called CRNW, is based on uncoupled PMCW radars using single-carrier BPSK modulation and is introduced in Chapter 4. Processing the bistatic signals of uncoupled radars leads to significant errors such as CFO, SFO, and phase noise, as analyzed in detail. By exploiting the characteristics of the BPSK-modulated single carrier signal, techniques are proposed which allow to overcome these errors by using Rx-side signal processing: A timing recovery is employed to detect the SFO between the DAC and ADC, which is then followed by a sample rate correction. Furthermore, a carrier recovery is proposed to reconstruct an IF carrier the signal is downconverted to based on an RL—including the phase noise induced by both, Tx and Rx. This way, a digital intradyne downconversion is performed, mitigating CFO, phase offsets, and phase noise. The efficacy of these techniques is validated by measurements.

The second concept proposed in Chapter 5 preserves coherency by avoiding a downconversion from RF at another sensor node altogether. A single OFDM radar is accompanied by multiple repeaters that receive the radar signal via reflections at the targets, leading to the so-called SymNW. After applying a frequency shift in the kHz-range, the signal is retransmitted and, subsequent to a second reflection at the targets, is received by the radar. The OFDM signal with its orthogonal subcarriers allows for excellent multiplexing—each repeater shifts the signal onto dedicated subcarriers initially unassigned by the radar. It is shown, that this radar network can be exploited for network-based DoA estimation, especially, since each repeater leads to a repetition of the radar's virtual array in the VNA. However, the SymNW is affected by MT propagation, i.e., by signal paths with reflections at different targets on the way to the repeater and back, creating ghost targets and impacting DoA estimation.

The third concept called TriNW is presented in Chapter 6. It combines an OFDM radar with a new type of repeater fed directly from a LoS path. These repeaters called MCRs distribute their signal to four different Tx channels, each with its own mixer to apply distinct frequency shifts. In this way, the TriNW is the most flexible radar network in terms of VNA design among those presented in this work, and shows excellent DoA estimation capabilities in measurements in an anechoic chamber.

In accordance with the second objective, the proposed radar networks are elaborately compared in Chapter 7 using four key criteria: The dynamic performance; the severity of ghost targets introduced by the network concept; VNA

design constraints; and finally the DoA estimation performance. The latter is compared for SymNW and TriNW using measurements. Each of the proposed networks demonstrates distinctive strengths and weaknesses. The signal processing-based Rx-side synchronization of a CRNW is appealing, yet, it is contingent upon an RL signal that must exceed the combined power of all other Rx signals. In controlled scenarios, such as UAV-based radar measurements or industrial applications, this concept is promising. However, it is not well suited for the high variability of target RCSs and ranges in automotive scenarios. The SymNW is severely limited by the signal attenuation resulting from doubling the propagation path to the target. This constraint renders it suitable only for very short ranges of approximately 10 m at most. Additionally, it is significantly affected by ghost targets due to MT paths. The TriNW, on the contrary, enables bistatic signal powers comparable to monostatic ones, and is only moderately impacted by ghost targets. It features a high flexibility in VNA design and shows an outstanding DoA estimation performance. The employed TriNW achieves a target separability of 0.8° and an SLL of −6.8 dB before CS, although it is based on a 4×4 MIMO radar only. Consequently, this network concept is the most promising for automotive radar imaging.

Finally, the potential of digital radar networks for radar imaging is verified by presenting extensive measurements of automotive scenarios using the TriNW. The scenarios include multiple road users such as a car, a pedestrian, a bicycle, and a motorcycle. It is demonstrated that the radar network detects each road user in great detail. This encompasses a multitude of features, including the legs of the pedestrian and cyclist, and the forks of the bicycle and motorcycle. In scenarios where multiple road users are in proximity, the TriNW demonstrates remarkable performance, allowing to detect a weak target such as a pedestrian next to a vehicle. The measurements thus provide compelling validation of the digital radar network's outstanding capabilities in radar imaging, thereby fulfilling the third key objective.

The benefits of uncoupled coherent radar networks extend far in excess of their application in automotive radar imaging. Their capability of processing bistatic signals is also valuable for applications such as the evaluation of bistatic backscatter and for bistatic SAR in remote sensing. This renders the network concepts and synchronization techniques presented in this thesis valuable beyond the demonstrated applications of network-based DoA estimation.

Appendix A Notation

The following provides a brief overview of the notation, selected operators, and functions used in this work. For an overview of the symbols used, refer to the Symbols section.

A.1 Matrices, Vectors, and Signals

- Matrices are notated using bold calligraphic capital letters, i.e., $\boldsymbol{\mathcal{A}}$. The element at the mth row and nth column of a matrix is referred to by $\mathcal{A}_{m,n}$.
- Vectors are notated using bold lowercase letters, i.e., $\boldsymbol{v}$. The kth element of a vector is referred to either using the index, i.e., v_k, or by using square brackets, i.e., $v[k]$, depending on the context.
- Continuous-time signals are denoted using round brackets, i.e., $x(t)$, while discrete-time signals are denoted using square brackets, $x[n]$, where n corresponds to the sample index.

A.2 Operators and Functions

- $\odot$ corresponds to an element-wise multiplication.
- $\otimes$ denotes the Kronecker product.
- $\oplus$ corresponds to an additive version of the Kronecker product. For two vectors $\boldsymbol{a} \in \mathbb{C}^M$, $\boldsymbol{b} \in \mathbb{C}^N$, their additive Kronecker product $(\boldsymbol{a} \oplus \boldsymbol{b}) \in \mathbb{C}^{M+N}$ is defined by its elements as

$$(\boldsymbol{a} \oplus \boldsymbol{b})_{(k-1)N+l} = a_k + b_l \,. \tag{A.1}$$

Note that this definition differs from the common definition of the Kronecker sum.

- $*$ denotes a convolution.
- $\delta(\cdot)$ is the Dirac delta function.
- DFT and IDFT are denoted as $\mathrm{DFT}[\cdot]$ and $\mathrm{IDFT}[\cdot]$. Consindering a matrix $\boldsymbol{\mathcal{M}}$, a row-wise DFT is denoted as $\overrightarrow{\mathrm{DFT}}\,[\boldsymbol{\mathcal{M}}]$ and a column-wise DFT as $\mathrm{DFT}\restriction[\boldsymbol{\mathcal{M}}]$.
- The set $\{a, \ldots, b\}$ refers to the set of all natural numbers $\mathbb{N}$ between a and b, including both a and b. Formally, $\{a, \ldots, b\} = \{x \in \mathbb{N} \mid a \leq x \leq b\}$.

Appendix B Algorithms for Single-Target Peak Classification

The classification of single target peaks is performed in two steps. The first step is to identify a reference peak, which must be chosen in a way that this first peak is a single target peak. Then, using this peak as a starting point, in the next step the other peaks are identified. The algorithms used for the ST peak classification have first been proposed in [115] by the author.

For the algorithm, a pre-processing resulting in two target-lists, a monostatic and a bistatic one, is required. The target lists must be in decreasing order of peak power, and have a length of $N_{\text{peak}}^{\text{mono}}$ and $N_{\text{peak}}^{\text{bi}}$, respectively. Any peaks resulting from mutual coupling or LoS between the Tx and Rx antennas must be excluded. Ideally, $N_{\text{peak}}^{\text{mono}} = N_{\text{T}}$ and $N_{\text{peak}}^{\text{bi}} = N_{\text{T}} + N_{\text{MT}}/2$, where N_{T} is the number of targets in the channel and N_{MT} the number of expected multi-target paths defined in (5.20). Yet, the target lists typically deviate from this due to false positives and false negatives in the peak detection.

B.1 Reference Peak

The reference peak is the starting point for the bistatic peak classification, and it is selected as described in Algorithm B.1. Starting with the first monostatic peak, i.e., the one with the highest peak power, the algorithm tests whether a monostatic peak k is separated by a minimum range offset ΔR_{min} and a minimum velocity offset Δv_{min} from every other monostatic peak $l \in \{1, \ldots, N_{\text{peak}}^{\text{mono}}\}$:

$$\begin{aligned} &|R_l - R_k| > \Delta R_{\text{min}} \\ &|v_l - v_k| > \Delta v_{\text{min}} \end{aligned}, \forall l \neq k \tag{B.1}$$

ΔR_{min} and Δv_{min} have to be selected with respect to the *Rv* resolution and the expected density of the target scenario. If (B.1) is not satisfied, the algorithm

Pseudocode B.1 Reference peak, adapted from [115], © 2022 EUMA.

Input: Mono- and bistatic target lists, sorted in decreasing order of peak power.
Output: Reference peak pair k_{ref}, p_{ref}

```
k_ref = 0
p_ref = 0
k = 1
while k ≤ N_peak^mono & k_ref = 0 do
  if k fulfills (B.1) then
    p = 1
    while p ≤ N_peak^bi & p_ref = 0 do
      if p, k fulfill (B.2) then
        if p fulfills (B.3) then
          k_ref = k
          p_ref = p
        end if
      end if
      p = p + 1
    end while
  end if
  k = k + 1
end while
```

continues with the next monostatic peak. Else, it searches a bistatic peak at approximatly twice the range and velocity, i.e., it searches a bistatic target fulfilling the condition

$$\begin{aligned} \left| R_p^{\mathrm{bi}} - 2R_k \right| &< \epsilon_R \\ \left| v_p^{\mathrm{bi}} - 2v_k \right| &< \epsilon_v \,. \end{aligned} \tag{B.2}$$

The thresholds ϵ_R and ϵ_v correspond to the maximum tolerable deviation of the bistatic peak position from the expected one. They must take into account the *Rv* resolution and the different aspect angles, but should be small enough to ensure that the peaks are correctly assigned. To further prevent misclassification, it is also ensured that the bistatic peak is well separated from other bistatic peaks, i.e., if

$$\begin{aligned} \left| R_q^{\mathrm{bi}} - R_p^{\mathrm{bi}} \right| &> \Delta R_{\min} \\ \left| v_q^{\mathrm{bi}} - v_p^{\mathrm{bi}} \right| &> \Delta v_{\min} \;\forall q \in \{1, \ldots, N_{\mathrm{peak}}^{\mathrm{bi}}\},\; q \neq p. \end{aligned} \tag{B.3}$$

applies. If a peak pair k_{ref}, p_{ref} is found that satisfies the conditions (B.1)–(B.3), it will be used as a reference peak pair in the next step.

B.2 Bistatic Peak Classification

Based on the bistatic reference peak p_{ref} identified as ST peak, all other bistatic peaks are classified in the next step. It is assumed, that if a bistatic peak q is an ST peak, then an MT peak must lie in between peak q and peak p_{ref}. Therefore, according to (5.21), in this case there must be a bistatic peak at

$$\begin{aligned} R_{p_{\mathrm{ref}},q}^{\mathrm{bi}} &= 0.5 R_{p_{\mathrm{ref}}}^{\mathrm{bi}} + 0.5 R_q^{\mathrm{bi}} \\ v_{p_{\mathrm{ref}},q}^{\mathrm{bi}} &= 0.5 v_{p_{\mathrm{ref}}}^{\mathrm{bi}} + 0.5 v_q^{\mathrm{bi}}. \end{aligned} \tag{B.4}$$

Consequently, using Algorithm B.2, for each peak in the bistatic targetlist

$s \in \{1, \ldots, N_{\text{peak}}^{\text{bi}}\},\ s \neq p_{\text{ref}} \wedge s \neq q$, it is checked whether

$$\begin{aligned} \left| R_s^{\text{bi}} - R_{p_{\text{ref}},q}^{\text{bi}} \right| &< \epsilon_R \\ \left| v_s^{\text{bi}} - v_{p_{\text{ref}},q}^{\text{bi}} \right| &< \epsilon_v. \end{aligned} \tag{B.5}$$

is fulfilled. If there is a peak to which (B.5) applies, then this peak s is an MT peak belonging to the ST peaks p_{ref} and q.

Pseudocode B.2 Bistatic target peak classification, adapted from [115], © 2022 EUMA.

Input: Mono- and bistatic target lists, sorted in decreasing order of peak power; reference peak pair k_{ref}, p_{ref}.
Output: Bistatic target lists with each peak either identified as ST or MT peak.

```
q = 1
while q ≤ N_peak^bi do
  s = 1
  while s ≤ N_peak^bi do
    if q, s fulfill (B.5) then
      Peak q is a ST peak
      Peak s is a MT peak based on p_ref and q
    end if
    s = s + 1
  end while
  q = q + 1
end while
```

In theory, assuming all bistatic peaks are correctly classified, only one iteration of Algorithm B.2 is sufficient. However, to increase robustness in the presence of clutter and noise, multiple iterations are recommended, each with a new reference target. In each iteration, a peak classified as ST peak in the previous iterations may serve as a new reference peak if a matching monostatic peak fulfilling (B.2) is found. The results of several iterations can then be combined, e.g., by checking whether a peak was classified as an ST peak in the majority of iterations. The classification example shown in Fig. 5.5 (c) is the result after six iterations.

Appendix C Array Design Influence on Angular Spectrum

In the following, the relation between the VNA design and the angular spectrum is derived. This has first been presented in [11] by the author. Assuming a network employing N_{NW} subarrays in the VNA. Every kth subarray at position $d_{\mathrm{NW}}[k]$ acts as a window function $w(x)$ of size l_{sub} when spatially acquiring the steering vector. Each $w(x)$ is centred at $d_{\mathrm{NW}}[k]+0.5l_{\mathrm{sub}}$, respectively. Assuming an ULA, $w(x)$ corresponds to a rectangular function $\mathrm{rect}(x)$, assuming a sparse subarray, $w(x)$ accounts for this sparse pattern. For the sake of simplicity, w.l.o.g. identical subarrays and thus identical $w(x)$ are assumed. The steering vector, as sampled by the VNA, and the resulting angular spectrum corresponding to the Fourier transform of the steering vector (defined in (2.49)), are described as follows:

$$\boldsymbol{\alpha}(x) \propto \mathrm{e}^{-\mathrm{j}\Psi_\theta x} \qquad \sum_{k=1}^{N_{\mathrm{NW}}} w\left(\frac{x-\frac{l_{\mathrm{sub}}}{2}-d_{\mathrm{NW}}[k]}{l_{\mathrm{sub}}}\right) \tag{C.1}$$

$$\begin{aligned}\mathbf{A}(\Psi) &\propto \delta(\Psi-\Psi_\theta) \quad * \sum_{k=1}^{N_{\mathrm{NW}}} W\left(\Psi\,\frac{l_{\mathrm{sub}}}{2}\right)\mathrm{e}^{-\mathrm{j}\Psi\left(\frac{l_{\mathrm{sub}}}{2}+d_{\mathrm{NW}}[k]\right)} \\ &= \underbrace{\delta\left(\Psi-\Psi_\theta\right)}_{\text{target angle}} \quad \underbrace{* W\left(\Psi\,\frac{l_{\mathrm{sub}}}{2}\right)\mathrm{e}^{-\mathrm{j}\Psi\frac{l_{\mathrm{sub}}}{2}}}_{\text{subarray}} \underbrace{\left(\sum_{k=1}^{N_{\mathrm{NW}}}\mathrm{e}^{-\mathrm{j}\Psi d_{\mathrm{NW}}[k]}\right)}_{\text{node position}}.\end{aligned} \tag{C.2}$$

$=V(\Psi)$, VNA function

The main factors determining the spectral response of a target peak thus are the following: The subarray function $w(x)$, including the size of the respective subarray l_{sub}, and the number of subarrays N_{NW} and their positions $d_{\mathrm{NW}}[k]$. Their influence can be exemplarily described for the example of two ULA-subarrays with a gap in between. Hence, $w(x)$=rect(x) and, in consequence, $W(\Psi)$=si(Ψ). In this example, and further assuming $d_{\mathrm{nw}}[1]$=0, the angular spectrum from (C.2) simplifies to

$$\mathbf{A}(\Psi) \propto \underbrace{\delta\left(\Psi - \Psi_\theta\right)}_{\substack{\text{target}\\ \text{angle}}} * \underbrace{\underbrace{\mathrm{si}\left(\Psi\frac{l_{\mathrm{sub}}}{2}\right)\mathrm{e}^{-\mathrm{j}\Psi\frac{l_{\mathrm{sub}}}{2}}}_{\text{subarray}}\underbrace{\left(1+\mathrm{e}^{-\mathrm{j}\Psi \boldsymbol{d}_{\mathrm{NW}}[2]}\right)}_{\text{node positions}}}_{=V(\Psi),\ \text{VNA function}}. \tag{C.3}$$

The DoA estimation typically uses the absolute value of the angular spectrum. This corresponds to

$$\left|\mathbf{A}(\Psi)\right| \propto \delta\left(\Psi - \Psi_\theta\right) * \left|\mathrm{si}\left(\Psi\frac{l_{\mathrm{sub}}}{2}\right)\right| \left|1+\mathrm{e}^{-\mathrm{j}\Psi \boldsymbol{d}_{\mathrm{NW}}[2]}\right| \tag{C.4}$$

$$= \delta\left(\Psi - \Psi_\theta\right) * \left|\mathrm{si}\left(\Psi\frac{l_{\mathrm{sub}}}{2}\right)\right| \sqrt{2\cos\left(\Psi d_{\mathrm{nw}}[2]\right)+2}\,. \tag{C.5}$$

The sinc function corresponds to the angular spectrum when using only a single SA, whereas the cosine leads to a narrow mainlobe, but also high sidelobes. This is described in detail in Section 7.1.3.

List of Symbols and Acronyms

The following is a glossary of symbols and acronyms used throughout this thesis. It includes all acronyms, as well as all important symbols, except for those used only locally. Where possible, duplicate entries have been avoided. In cases where symbols have multiple meanings, the correct interpretation can be deduced from the context. In accordance with DIN 1338, all symbols are displayed in italics.

Symbols

A	amplitude	64, 65, 88
$\boldsymbol{a}$	steering vector	20
$\tilde{\boldsymbol{a}}$	non-normalized steering vector	101
$\boldsymbol{\alpha}$	extended steering vector (in virtual array grid)	24
$\mathbf{A}(\Psi)$	angular spectrum	24
B	bandwidth	18
b	modulation factor	77
D	array size	21
$\boldsymbol{d}$	code vector	10
$\boldsymbol{\mathcal{D}}$	division matrix	11
$\boldsymbol{\mathcal{D}}^{\mathrm{LoS}}$	symbol-domain Tx matrix of the LoS path	96
d_{LoS}	length of the LoS path	113
$\boldsymbol{d}_{\mathrm{VNA}}$	VNA	80
$\boldsymbol{\mathcal{D}}^{\mathrm{Rx}}$	symbol-domain Rx matrix	15
$\boldsymbol{\mathcal{D}}^{\mathrm{Sym}}$	symbol matrix	66
$\boldsymbol{\mathcal{D}}^{\mathrm{Tx}}$	symbol-domain Tx matrix	14
$\boldsymbol{d}$	virtual array	23
δ	relative clock error	41
Δf_{d}	Doppler frequency resolution	39
ΔR	range resolution	115

Δv	velocity resolution ... 60
Δf	subcarrier spacing ... 13
Δm_{Tx}	spacing between two assigned symbols ... 73
Δn_{Tx}	spacing between two assigned subcarriers ... 73
$\Delta\varphi_{\mathrm{mod}}$	phase offset of the modulation signal during CP ... 65
ΔT_{s}	sample time error ... 41
f_{d}	Doppler frequency ... 16
f_{CFO}	CFO ... 9
f_{IF}	IF frequency ... 46
f_{mod}	modulation frequency ... 62
f_n	subcarrier frequency ... 14
f_{Rx}	Rx carrier frequency ... 8
f_{s}	sample frequency ... 11
f_{SFO}	SFO ... 28
$f_{\mathrm{s,Rx}}$	Rx-side sample frequency ... 28
$f_{\mathrm{s,Tx}}$	Tx-side sample frequency ... 28
f_{Tx}	Rx carrier frequency ... 6
G	gain ... 112
h	modulation index ... 64
$h(t)$	pulse filter ... 10
$\boldsymbol{\mathcal{I}}^{\mathrm{R}}$	range matrix ... 11
$\boldsymbol{\mathcal{I}}^{\mathrm{Rv}}$	*Rv* matrix ... 6
$\boldsymbol{\mathcal{I}}^{\mathrm{v}}$	velocity matrix ... 15
L	attenuation ... 64, 93
l_{sub}	size of the subarray ... 119
λ	wavelength ... 21
M	number of sequences ... 6
m	sequence enumerator ... 6
N	code length (PMCW); number of subcarriers (OFDM) ... 10
N_{T}	number of targets ... 7
$n_{\mathrm{cr}}(t)$	noise and interference in the carrier recovery ... 47
N_{MCR}	number of MCRs ... 98
N_{RP}	number of repeater ... 65
N_{Rx}	number of Rx channels ... 20
N_{Tx}	number of Tx channels ... 18

n_b	oversampling factor	11
P	power	6, 7, 39, 48
P_Tx	Tx power	6
$\mathcal{L}(f_\mathrm{offset})$	power density spectrum	38
ϕ_err	phase error, including phase noise	9
P_n	noise power	48
P_pn	phase noise power	39
Ψ	angular frequency	24
ϕ_mod	modulation phase	64
$\phi_\mathrm{Rx}(t)$	Rx phase	8
$\phi_\mathrm{Tx}(t)$	Tx phase	6
R	range	6
R^bi	bistatic range	69
R_c	code rate	10
R^ua	unambiguous range	18
σ	RCS	112
$s_\mathrm{Rx}(t)$	carrier signal at Rx	8
$s_\mathrm{Tx}(t)$	carrier signal at Tx	6
$s_\mathrm{IF}(t)$	IF carrier	46
t	time	6
T_CP	CP length	14
T_sym	OFDM symbol length	13
T_c	chip duration	10
T_obs	observation time	6
T_s	sample time	12
T	duration of a single sequence	6
$\tau(t)$	ToF	7
τ^R	range-dependent ToF	8
$\tau^\mathrm{v}(t)$	velocity-dependent ToF	7
θ	azimuth angle	20
$\theta[n]$	range-dependent phase term via the subcarriers	16
$V(\Psi)$	VNA function	119
v^bi	bistatic velocity	69
v_err	velocity error	37
v	radial velocity	6

v^{ua}	unambiguous velocity ... 18
$W(\Psi)$	SA function ... 119
$\boldsymbol{\mathcal{X}}$	time-domain Tx matrix ... 15
$x(t)$	Tx signal ... 6
$x_{\mathrm{BB}}(t)$	baseband Tx signal ... 6
$x_{\mathrm{mod}}(t)$	modulation signal ... 64
$x_{\mathrm{RP}}(t)$	repeater Tx signal ... 64
$x_{\mathrm{seq}}(t)$	single sequence ... 10, 12, 38, 46
$\boldsymbol{\mathcal{Y}}$	time-domain Rx matrix ... 15
$y(t)$	Rx signal ... 6
$y_{\mathrm{BB}}(t)$	baseband Rx signal ... 6
$y_{\mathrm{IF}}(t)$	IF Rx signal ... 47
$y_{\mathrm{MCR}}(t)$	MCR Rx signal ... 93
$y_0(t)$	Rx signal from RL ... 47
$y_{\mathrm{RP}}(t)$	repeater Rx signal ... 63

Acronyms

Rv	range-Doppler ... 11
ACDC	All Cell Doppler Correction ... 118
ADC	analog-to-digital converter ... 18
APAS	Almost Perfect Autocorrelation Sequence ... 10
AWG	arbitrary waveform generator ... 35
AWGN	additional white Gaussian noise ... 47
BP	bandpass filter ... 50
BPSK	binary phase shift keying ... 5
CAMP	complex approximate message passing ... 74
CDM	code-division multiplexing ... 2
CFO	carrier frequency offset ... 9
CP	cyclic prefix ... 15
CRNW	PMCW-based radar network with carrier recovery ... 33
CS	compressed sensing ... 19
CW	continous wave ... 5

DAC	digital-to-analog converter ... 6
DFT	discrete Fourier transform ... 13
DoA	direction of arrival ... 1
DSB	double-sideband ... 6
FDM	frequency-division multiplexing ... 2
FFT	fast Fourier transform ... 13
FMCW	frequency modulated continuous-wave ... 1
FPGA	field-programmable gate array ... 83
GT	ground truth ... 104
ICI	intercarrier interference ... 16
IDFT	inverse discrete Fourier transform ... 15
IF	intermediate frequency ... 33
IFFT	inverse fast Fourier transform ... 15
IMAT	iterative method with adaptive thresholding ... 82
IQ	in-phase & quadrature ... 6
ISI	intersymbol interference ... 13
LF	low frequency ... 27
LO	local oscillator ... 28
LoS	line-of-sight ... 4, VIII
LP	lowpass filter ... 36
LSB	lower sideband ... 79
MCR	multi-channel repeater ... 91, VIII
MIMO	multiple-input multiple-output ... 2, 5
ML	maximum likelihood ... 23
MMIC	monolithic microwave integrated circuit ... 1, 25
MT	multi-target ... 69
MUSIC	multiple signal classification ... 24
OFDM	orthogonal frequency-division multiplexing ... 2, VII
OTA	over-the-air ... 30, 31
PAPR	peak-to-average power ratio ... 110
PCB	printed ciruit board ... 25
PLL	phase-locked loop ... 27
PMCW	phase-modulated continous wave ... 2, VII
PNR	peak-to-noise ratio ... 13
PSD	power spectral density ... 39

PSR	peak-to-skirt ratio	51
QPSK	quadrature phase-shift keying	14
RCS	radar cross section	26
RF	radio frequency	2
RFDM	random frequency-division multiplexing	73, 74
RL	reference link	31, 34
RP-OFDM	repeat OFDM	14
Rx	receive	1
SA	subarray	98
SAR	synthetic aperture radar	25
SFO	sample frequency offset	26
SISO	single-input single-output	123
SLL	sidelobe level	82
SNR	signal-to-noise ratio	47
SoC	system-on-chip	5
SSB	single-sideband	39
ST	single-target	68
SymNW	symmetrical-path radar-repeater network	61
TDM	time-division multiplexing	2
TFDM	time-and-frequency-division multiplexing	73
ToF	time-of-flight	7
TriNW	triangular-path radar-repeater network	91
Tx	transmit	1
UAV	unmanned aerial vehicle	111
ULA	uniform linear array	23
USB	upper sideband	76
VGA	variable gain amplifier	62
VNA	virtual network-array	29, VIII
w.l.o.g.	without loss of generality	16
ZP	zero padding	82

Bibliography

[1] C. Waldschmidt, J. Hasch, and W. Menzel, "Automotive Radar — From First Efforts to Future Systems," *IEEE J. Microw.*, vol. 1, no. 1, pp. 135–148, January 2021 (cit. on pp. 1, 20, 25).

[2] J. Jeffs, *Short-Range Radars Have Huge Potential in the Automotive Radar Market*, URL: https://www.idtechex.com/de/research-article/short-range-radars-have-huge-potential-in-the-automotive-radar-market/29984 last accessed: 4.8.2024, October 2023 (cit. on p. 1).

[3] A. Och, C. Pfeffer, J. Schrattenecker, S. Schuster, and R. Weigel, "A Scalable 77 GHz Massive MIMO FMCW Radar by Cascading Fully-Integrated Transceivers," in *Asia-Pacific Microw. Conf. (APMC)*, November 2018, pp. 1235–1237 (cit. on p. 1).

[4] J. Kim, B. Kim, S. Choi, *et al.*, "79-GHz Four-RFIC Cascading Radar System for Autonomous Driving," in *IEEE Int. Symp. Circuits Syst. (ISCAS)*, October 2020, pp. 1–5 (cit. on p. 1).

[5] F. Engels, P. Heidenreich, M. Wintermantel, L. Stäcker, M. Al Kadi, and A. M. Zoubir, "Automotive Radar Signal Processing: Research Directions and Practical Challenges," *IEEE J. Sel. Topics Signal Process.*, vol. 15, no. 4, pp. 865–878, Jun. 2021 (cit. on pp. 1, 20, 25).

[6] D. Schwarz, N. Riese, I. Dorsch, and C. Waldschmidt, "System Performance of a 79 GHz High-Resolution 4D Imaging MIMO Radar With 1728 Virtual Channels," *IEEE J. Microw.*, vol. 2, no. 4, pp. 637–647, October 2022 (cit. on pp. 1, 25).

[7] A. Stroescu, M. Cherniakov, and M. Gashinova, "Classification of High Resolution Automotive Radar Imagery for Autonomous Driving Based on Deep Neural Networks," in *20th Int. Radar Symp. (IRS)*, ISSN: 2155-5753, Jun. 2019, pp. 1–10 (cit. on pp. 1, 127).

[8] M. Gottinger, P. Gulden, and M. Vossiek, "Coherent Signal Processing for Loosely Coupled Bistatic Radar," *IEEE Trans. Aerosp. Electron. Syst.*, vol. 57, no. 3, pp. 1855–1871, 2021 (cit. on pp. 1, 27, 120, 122).

[9] A. Dürr, D. Böhm, D. Schwarz, S. Häfner, R. Thomä, and C. Waldschmidt, "Coherent Measurements of a Multistatic MIMO Radar Network With Phase Noise Optimized Non-Coherent Signal Synthesis," *IEEE J. Microw.*, vol. 2, no. 2, pp. 239–252, 2022 (cit. on pp. 1, 31).

[10] V. Janoudi, P. Schoeder, T. Grebner, N. Appenrodt, J. Dickmann, and C. Waldschmidt, "Signal Model for Coherent Processing of Uncoupled and Low Frequency Coupled MIMO Radar Networks," *IEEE J. Microw.*, pp. 1–17, 2023 (cit. on pp. 1, 29–31).

[11] D. Werbunat, B. Woischneck, J. Lerch, *et al.*, "Multichannel Repeater for Coherent Radar Networks Enabling High-Resolution Radar Imaging," *IEEE Trans. Microw. Theory Techn.*, pp. 1–13, 2023 (cit. on pp. 2, 25, 28, 30, 31, 80, 82, 84, 91, 93–95, 102, 104–106, 110, 119, 121, 126, 128, 139).

[12] G. Hakobyan and B. Yang, "High-Performance Automotive Radar: A Review of Signal Processing Algorithms and Modulation Schemes," *IEEE Signal Process. Mag.*, vol. 36, no. 5, pp. 32–44, Sep. 2019 (cit. on pp. 2, 5–7, 109).

[13] B. Schweizer, A. Grathwohl, G. Rossi, *et al.*, "The Fairy Tale of Simple All-Digital Radars: How to Deal With 100 Gbit/s of a Digital Millimeter-Wave MIMO Radar on an FPGA [Application Notes]," *IEEE Microw. Mag.*, vol. 22, no. 7, pp. 66–76, Jul. 2021 (cit. on pp. 2, 18, 83).

[14] J. Sachs, "M-Sequence Ultra-Wideband-Radar: State of Development and Applications," in *Proc. Int. Conf. Radar*, Sep. 2003, pp. 224–229 (cit. on pp. 2, 5, 9).

[15] H. J. Ng, R. Feger, and A. Stelzer, "A Fully-Integrated 77-GHz UWB Pseudo-Random Noise Radar Transceiver With a Programmable Sequence Generator in SiGe Technology," *IEEE Trans. Circuits Syst. I: Regular Papers*, vol. 61, no. 8, pp. 2444–2455, August 2014 (cit. on pp. 2, 5, 9, 10).

[16] V. Giannini, D. Guermandi, Q. Shi, *et al.*, "A 79 GHz Phase-Modulated 4 GHz-BW CW Radar Transmitter in 28 nm CMOS," *IEEE J. Solid-State Circuits*, vol. 49, no. 12, pp. 2925–2937, December 2014 (cit. on pp. 2, 5, 9, 10, 18).

[17] Nadav Levanon, "Multifrequency complementary phase-coded radar signal," *IEE Proc. - Radar, Sonar and Navig.*, vol. 147, no. 6, p. 276, 2000 (cit. on pp. 2, 5, 14).

[18] C. Sturm, E. Pancera, T. Zwick, and W. Wiesbeck, "A Novel Approach to OFDM Radar Processing," in *IEEE Radar Conf.*, IEEE, 2009, pp. 1–4 (cit. on pp. 2, 14, 17, 18).

[19] G. Hakobyan and B. Yang, "A Novel Narrowband Interference Suppression Method for OFDM Radar," in *24th Eur. Signal Process. Conf. (EUSIPCO)*, ISSN: 2076-1465, August 2016, pp. 2230–2234 (cit. on p. 2).

[20] S. Stephany, B. Schweizer, C. Knill, and C. Waldschmidt, "Impact of an Automotive Chirp-Sequence Interferer on a Wideband Pseudo-Noise Radar," in *Int. Conf. Electromagn. Adv. Appl. (ICEAA)*, Sep. 2019, pp. 0859–0862 (cit. on pp. 2, 10).

[21] C. Knill, B. Schweizer, S. Stephany, D. Werbunat, and C. Waldschmidt, "FMCW-Interference of Frequency Agile OFDM Radars," in *17th Europ. Radar Conf.*, 2021, pp. 160–163 (cit. on p. 2).

[22] B. Schweizer, C. Knill, D. Werbunat, S. Stephany, and C. Waldschmidt, "Mutual Interference of Automotive OFDM Radars—Analysis and Countermeasures," *IEEE J. Microw.*, vol. 1, no. 4, pp. 950–961, October 2021 (cit. on p. 2).

[23] C. Sturm and W. Wiesbeck, "Waveform Design and Signal Processing Aspects for Fusion of Wireless Communications and Radar Sensing," *Proc. of the IEEE*, vol. 99, no. 7, pp. 1236–1259, 2011 (cit. on p. 2).

[24] L. Giroto de Oliveira, B. Nuss, M. B. Alabd, A. Diewald, M. Pauli, and T. Zwick, "Joint Radar-Communication Systems: Modulation Schemes and System Design," *IEEE Trans. Microw. Theory Techn.*, vol. 70, no. 3, pp. 1521–1551, March 2022 (cit. on p. 2).

[25] V. Shatov, B. Nuss, S. Schieler, *et al.*, "Joint Radar and Communications: Architectures, Use Cases, Aspects of Radio Access, Signal Processing, and Hardware," *IEEE Access*, vol. 12, pp. 47 888–47 914, 2024 (cit. on p. 2).

[26] S. Faghih-Naini, C. Sebastian, T. Reissland, R. Weigel, and B. Scheiner, "Hardware Design Challenges and Modulation Schemes in Joint Communication and Sensing: Analyzation and Comparison of the State-of-the-Art Co-Located Communication and Sensing Systems," *IEEE Microw. Mag.*, vol. 25, no. 3, pp. 84–97, March 2024 (cit. on p. 2).

[27] R. Michev, Y. Shu, D. Werbunat, J. Hasch, and C. Waldschmidt, "Adaptive Compensation of Hardware Impairments in Digitally Modulated Radars Using ML-Based Behavioral Models," *IEEE Trans. Microw. Theory Techn.*, pp. 1–14, 2023 (cit. on p. 2).

[28] C. Sturm, Y. L. Sit, M. Braun, and T. Zwick, "Spectrally interleaved multi-carrier signals for radar network applications and multi-input multi-output radar," *IET Radar, Sonar & Navigation*, vol. 7, no. 3, pp. 261–269, 2013 (cit. on pp. 2, 5, 14, 19).

[29] H. Haderer, R. Feger, C. Pfeffer, and A. Stelzer, "Millimeter-Wave Phase-Coded CW MIMO Radar Using Zero- and Low-Correlation-Zone Sequence Sets," *IEEE Trans. Microw. Theory Techn.*, vol. 64, no. 12, pp. 4312–4323, December 2016 (cit. on pp. 2, 19).

[30] A. Bourdoux, U. Ahmad, D. Guermandi, S. Brebels, A. Dewilde, and W. Van Thillo, "PMCW Waveform and MIMO Technique for a 79 GHz CMOS Automotive Radar," in *IEEE Radar Conf.*, ISSN: 2375-5318, May 2016, pp. 1–5 (cit. on pp. 2, 19).

[31] C. Knill, F. Embacher, B. Schweizer, S. Stephany, and C. Waldschmidt, "Coded OFDM Waveforms for MIMO Radars," *IEEE Trans. Veh. Techn.*, vol. 70, no. 9, pp. 8769–8780, Sep. 2021 (cit. on pp. 2, 19).

[32] C. Knill, F. Roos, B. Schweizer, D. Schindler, and C. Waldschmidt, "Random Multiplexing for an MIMO-OFDM Radar With Compressed Sensing-Based Reconstruction," *IEEE Microw. Wireless Compon. Lett.*, vol. 29, no. 4, pp. 300–302, April 2019 (cit. on pp. 2, 19, 74).

[33] B. Farley, J. McGrath, and C. Erdmann, "An All-Programmable 16-nm RFSoC for Digital-RF Communications," *IEEE Micro*, vol. 38, no. 2, pp. 61–71, 2018 (cit. on pp. 5, 83).

[34] *Apollo MxFE Quad, 16-Bit, 28 GSPS RF DAC and Quad, 12-Bit, 20 GSPS RF ADC*, Rev. PrA, AD9084, Analog Devices, 2023 (cit. on p. 5).

[35] Nadav Levanon, "Multifrequency Radar Signals," in *Rec. IEEE Int. Radar Conf.*, IEEE, 2000 (cit. on pp. 5, 14).

[36] M. C. Budge and M. P. Burt, "Range Correlation Effects in Radars," in *IEEE Nat. Radar Conf.*, IEEE Aerospace and Electronic Systems Society, 1993, pp. 212–216 (cit. on pp. 8, 30, 37).

[37] W. Lee, T. Dinc, and A. Valdes-Garcia, "Multi-Mode 60-GHz Radar Transmitter SoC in 45-nm SOI CMOS," *IEEE J. Solid-State Circuits*, vol. 55, no. 5, pp. 1187–1198, May 2020 (cit. on p. 10).

[38] F. Probst, A. Engelmann, P. Hetterle, V. Issakov, R. Weigel, and M. Dietz, "A 15-Gb/s PMCW Radar PRBS-Generator for MIMO and Joint Radar-Communication Systems," in *Asia-Pacific Microw. Conf. (APMC)*, November 2022, pp. 288–290 (cit. on p. 10).

[39] J. G. Proakis, *Digital Communications*, en. McGraw-Hill, 2001 (cit. on p. 10).

[40] H. Zhu, X. Shang, and J. Li, "Target Parameter Estimation via One-Bit PMCW Radar," in *IEEE Int. Conf. Acoustics, Speech Signal Process. (ICASSP)*, ISSN: 2379-190X, May 2020, pp. 9145–9149 (cit. on p. 10).

[41] W. Van Thillo, P. Gioffré, V. Giannini, D. Guermandi, S. Brebels, and A. Bourdoux, "Almost perfect auto-correlation sequences for binary phase-modulated continuous wave radar," in *Eur. Radar Conf. (EuRAD)*, October 2013, pp. 491–494 (cit. on pp. 11, 110).

[42] M. I. Skolnik, *Radar Handbook, Third Edition*, en. McGraw-Hill Education, 2008 (cit. on p. 11).

[43] R. Gold, "Optimal Binary Sequences for Spread Spectrum Multiplexing (Corresp.)," *IEEE Trans. Inf. Theory*, vol. 13, no. 4, pp. 619–621, October 1967 (cit. on p. 11).

[44] A. Bourdoux and M. Bauduin, "PMCW Waveform Cross-correlation Characterization and Interference Mitigation," in *17th Eur. Radar Conf. (EuRAD)*, January 2021, pp. 164–167 (cit. on p. 11).

[45] D. Werbunat, J. Aguilar, M. Almarashly, *et al.*, "On the Synchronization of Uncoupled Multistatic PMCW Radars," *IEEE Trans. Microw. Theory Techn.*, 2024 (cit. on pp. 11, 31, 33, 35, 36, 38–40, 43, 45, 47, 51, 52, 54, 56, 58, 59).

[46] J. Overdevest, F. Jansen, F. Uysal, and A. Yarovoy, "Doppler Influence on Waveform Orthogonality in 79 GHz MIMO Phase-Coded Automotive Radar," *IEEE Trans. Veh. Techn.*, vol. 69, no. 1, pp. 16–25, January 2020 (cit. on pp. 13, 37, 42).

[47] S. Xu and A. Yarovoy, "Doppler Shifts Mitigation for PMCW Signals," in *Int. Radar Conf. (RADAR)*, ISSN: 2640-7736, Sep. 2019, pp. 1–5 (cit. on p. 13).

[48] R. W. Chang, "Synthesis of Band-Limited Orthogonal Signals for Multichannel Data Transmission," *The Bell System Tech. J.*, vol. 45, no. 10, pp. 1775–1796, December 1966 (cit. on p. 13).

[49] S. Weinstein and P. Ebert, "Data Transmission by Frequency-Division Multiplexing Using the Discrete Fourier Transform," *IEEE Trans. Communication Technol.*, vol. 19, no. 5, pp. 628–634, October 1971 (cit. on p. 13).

[50] T. Hwang, C. Yang, G. Wu, S. Li, and G. Ye Li, "OFDM and Its Wireless Applications: A Survey," *IEEE Trans. Veh. Techn.*, vol. 58, no. 4, pp. 1673–1694, May 2009 (cit. on p. 13).

[51] J. G. Andrews, S. Buzzi, W. Choi, *et al.*, "What Will 5G Be?" *IEEE J. Sel. Areas Commun.*, vol. 32, no. 6, pp. 1065–1082, Jun. 2014 (cit. on p. 13).

[52] C. Y. Wong, R. Cheng, K. Lataief, and R. Murch, "Multiuser OFDM with adaptive subcarrier, bit, and power allocation," *IEEE J. Sel. Areas Commun.*, vol. 17, no. 10, pp. 1747–1758, October 1999 (cit. on p. 13).

[53] F. Frederiksen and R. Prasad, "An overview of OFDM and related techniques towards development of future wireless multimedia communications," in *Proc. RAWCON IEEE Radio and Wireless Conf.*, August 2002, pp. 19–22 (cit. on p. 13).

[54] Y. L. Sit, C. Sturm, and T. Zwick, "Doppler Estimation in an OFDM Joint Radar and Communication System," in *German Microw. Conf. (GeMiC)*, 2011, pp. 1–4 (cit. on p. 14).

[55] G. Hakobyan, "Orthogonal Frequency Division Multiplexing Multiple-Input Multiple-Output Automotive Radar with Novel Signal Processing Algorithms," en, Ph.D. dissertation, 2018 (cit. on pp. 14, 110, 118).

[56] J. Aguilar, D. Werbunat, V. Janoudi, C. Bonfert, and C. Waldschmidt, "Uncoupled Digital Radars Creating a Coherent Sensor Network," *IEEE J. Microw.*, pp. 1–14, 2024 (cit. on pp. 14, 29–31).

[57] D. Werbunat, F. Sgroi, C. Knill, *et al.*, "Multiplexing of OFDM-Based Radar Networks," in *IEEE Radar Conf.*, IEEE, 2021, pp. 1–6 (cit. on pp. 14, 63, 72, 73, 75, 76).

[58] C. Sturm, T. Zwick, and W. Wiesbeck, "An OFDM System Concept for Joint Radar and Communications Operations," in *IEEE 69th Veh. Technol. Conf.*, IEEE, 2009, pp. 1–5 (cit. on pp. 16, 73).

[59] G. Hakobyan and B. Yang, "A Novel Intercarrier-Interference Free Signal Processing Scheme for OFDM Radar," *IEEE Trans. Veh. Techn.*, vol. 67, no. 6, pp. 5158–5167, Jun. 2018 (cit. on pp. 16, 118).

[60] S. H. Talisa, K. W. O'Haver, T. M. Comberiate, M. D. Sharp, and O. F. Somerlock, "Benefits of Digital Phased Array Radars," *Proc. of the IEEE*, vol. 104, no. 3, pp. 530–543, March 2016 (cit. on p. 20).

[61] J. Li and P. Stoica, "MIMO Radar with Colocated Antennas," *IEEE Signal Process. Mag.*, vol. 24, no. 5, pp. 106–114, 2007 (cit. on pp. 20, 123).

[62] J. Li and P. Stoica, Eds., *MIMO Radar Signal Processing*. Wiley, 2009 (cit. on p. 20).

[63] C. A. Balanis, *Antenna Theory: Analysis and Design*, 3rd Ed. Wiley, 2005 (cit. on p. 21).

[64] L. Tao and H. Kwan, "A Novel Approach to Fast DOA Estimation of Multiple Spatial Narrowband Signals," in *45th Midwest Symp. Circuits Syst.*, IEEE (cit. on pp. 23, 82).

[65] C. Vasanelli, F. Roos, A. Durr, *et al.*, "Calibration and Direction-of-Arrival Estimation of Millimeter-Wave Radars: A Practical Introduction," *IEEE Antennas Propag. Mag.*, vol. 62, no. 6, pp. 34–45, December 2020 (cit. on pp. 23, 24, 84).

[66] X. Zhang, L. Xu, L. Xu, and D. Xu, "Direction of Departure (DOD) and Direction of Arrival (DOA) Estimation in MIMO Radar with Reduced-Dimension MUSIC," *IEEE Communications Lett.*, vol. 14, no. 12, pp. 1161–1163, December 2010 (cit. on p. 24).

[67] F. Roos, P. Hügler, L. L. Tovar Torres, *et al.*, "Compressed Sensing based Single Snapshot DoA Estimation for Sparse MIMO Radar Arrays," in *German Microw. Conf. (GeMiC)*, IEEE, 2019 (cit. on pp. 24, 82, 101).

[68] D. Kirk, J. Bergin, P. Techau, and J. Don Carlos, "Multi-Static Coherent Sparse Aperture Approach to Precision Target Detection and Engagement," in *IEEE Int. Radar Conf.*, May 2005, pp. 579–584 (cit. on p. 25).

[69] A. M. Haimovich, R. S. Blum, and L. J. Cimini, "MIMO Radar with Widely Separated Antennas," *IEEE Signal Process. Mag.*, vol. 25, no. 1, pp. 116–129, 2008 (cit. on p. 25).

[70] G. Krieger and A. Moreira, "Spaceborne bi- and multistatic SAR: Potential and challenges," en, *IEE Proc. - Radar, Sonar and Navig.*, vol. 153, no. 3, pp. 184–198, Jun. 2006 (cit. on pp. 25, 28).

[71] P. van Dorp, M. Otten, and J. Verzeilberg, "Coherent Multistatic ISAR imaging," in *IET Int. Conf. on Radar Systems (Radar 2012)*, October 2012, pp. 1–6 (cit. on p. 25).

[72] J. Hasch, E. Topak, R. Schnabel, T. Zwick, R. Weigel, and C. Waldschmidt, "Millimeter-Wave Technology for Automotive Radar Sensors in the 77 GHz Frequency Band," *IEEE Trans. Microw. Theory Techn.*, vol. 60, no. 3, pp. 845–860, March 2012 (cit. on pp. 25, 84, 103).

[73] D. Werbunat, B. Meinecke, B. Schweizer, J. Hasch, and C. Waldschmidt, "OFDM-Based Radar Network Providing Phase Coherent DOA Estimation," *IEEE Trans. Microw. Theory Techn.*, vol. 69, no. 1, pp. 325–336, January 2021 (cit. on pp. 25, 28, 30, 31, 61–63, 76, 77, 82, 118).

[74] M. Gottinger, M. Hoffmann, M. Christmann, *et al.*, "Coherent Automotive Radar Networks: The Next Generation of Radar-Based Imaging and Mapping," *IEEE J. Microw.*, vol. 1, no. 1, pp. 149–163, 2021 (cit. on pp. 25, 27–29, 122).

[75] A. Dürr, "Koppelbare Radarsensoren zur hochauflösenden Bildgebung bei 150 GHz," Ph.D. dissertation, Universität Ulm, December 2022 (cit. on p. 25).

[76] R. Burkholder, L. Gupta, and J. Johnson, "Comparison of monostatic and bistatic radar images," *IEEE Antennas Propag. Mag.*, vol. 45, no. 3, pp. 41–50, Jun. 2003 (cit. on p. 26).

[77] J. A. Jackson, B. D. Rigling, and R. L. Moses, "Canonical Scattering Feature Models for 3D and Bistatic SAR," *IEEE Trans. Aerosp. Electron. Syst.*, vol. 46, no. 2, pp. 525–541, April 2010 (cit. on pp. 26, 28).

[78] A. Grathwohl, B. Meinecke, M. Widmann, J. Kanz, and C. Waldschmidt, "UAV-Based Bistatic SAR-Imaging Using a Stationary Repeater," *IEEE J. Microw.*, vol. 3, no. 2, pp. 625–634, April 2023 (cit. on pp. 26, 28).

[79] G. Krieger, A. Moreira, H. Fiedler, *et al.*, "TanDEM-X: A Satellite Formation for High-Resolution SAR Interferometry," *IEEE Trans. Geosci. Remote Sens.*, vol. 45, no. 11, pp. 3317–3341, November 2007 (cit. on p. 26).

[80] M. Zink, A. Moreira, I. Hajnsek, *et al.*, "TanDEM-X: 10 Years of Formation Flying Bistatic SAR Interferometry," *IEEE J. Sel. Topics Appl. Earth Observ. Remote Sens.*, vol. 14, pp. 3546–3565, 2021 (cit. on p. 26).

[81] V. Zavorotny, D. Masters, A. Gasiewski, *et al.*, "Seasonal Polarimetric Measurements of Soil Moisture Using Tower-Based GPS Bistatic Radar," in *Proc. IEEE Int. Geosci Remote Sens Symp.*, vol. 2, Jul. 2003, 781–783 vol.2 (cit. on p. 26).

[82] N. Pierdicca, L. Pulvirenti, F. Ticconi, and M. Brogioni, "Radar Bistatic Configurations for Soil Moisture Retrieval: A Simulation Study," *IEEE Trans. Geosci. Remote Sens.*, vol. 46, no. 10, pp. 3252–3264, October 2008 (cit. on p. 26).

[83] M. Pieraccini, L. Miccinesi, and N. Rojhani, "A GBSAR Operating in Monostatic and Bistatic Modalities for Retrieving the Displacement Vector," *IEEE Geosci. Remote Sensing Lett.*, vol. 14, no. 9, pp. 1494–1498, Sep. 2017 (cit. on pp. 26, 28).

[84] M. Stefko, O. Frey, C. Werner, and I. Hajnsek, "Calibration and Operation of a Bistatic Real-Aperture Polarimetric-Interferometric Ku-Band Radar," *IEEE Trans. Geosci. Remote Sens.*, vol. 60, pp. 1–19, 2022 (cit. on pp. 26, 28).

[85] P. K. Rennich, M. D. Casciato, A. M. Chan, and S. D. Eye, "Coherent Multistatic SAR Collections and Target Phenomenology," in *Eur. Radar Conf. (EuRAD)*, October 2008, pp. 152–155 (cit. on p. 27).

[86] M. Zhan, X. Xie, H. Yao, R. Xu, and W. Lin, "A Novel Full Phase-Coherent Frequency Synthesis Method for SFWF Radar Application," *IEEE Trans. Microw. Theory Techn.*, vol. 59, no. 7, pp. 1840–1845, Jul. 2011 (cit. on p. 27).

[87] V. Janoudi, P. Schoeder, T. Grebner, *et al.*, "Antenna Array Design for Coherent MIMO Radar Networks," in *IEEE Radar Conf.*, May 2023, pp. 1–6 (cit. on pp. 27, 122).

[88] S. Futatsumori, K. Morioka, A. Kohmura, K. Okada, and N. Yonemoto, "Design and Field Feasibility Evaluation of Distributed-Type 96 GHz FMCW Millimeter-Wave Radar Based on Radio-Over-Fiber and Optical Frequency Multiplier," *J. Lightw. Technol.*, vol. 34, no. 20, pp. 4835–4843, October 2016 (cit. on p. 27).

[89] P. Ghelfi, L. Lembo, F. Scotti, G. Serafino, S. Maresca, and A. Bogoni, "Distributed Coherent Radars Enabled by Fiber Networks," in *21st Int. Conf. Transparent Optical Networks (ICTON)*, ISSN: 2161-2064, Jul. 2019, pp. 1–4 (cit. on p. 27).

[90] A. Dürr, D. Schwarz, S. Häfner, *et al.*, "High-Resolution 160-GHz Imaging MIMO Radar Using MMICs With On-Chip Frequency Synthesizers," *IEEE Trans. Microw. Theory Techn.*, vol. 67, no. 9, pp. 3897–3907, Sep. 2019 (cit. on pp. 27, 39).

[91] A. Dürr, R. Kramer, D. Schwarz, M. Geiger, and C. Waldschmidt, "Calibration-Based Phase Coherence of Incoherent and Quasi-Coherent 160-GHz MIMO Radars," *IEEE Trans. Microw. Theory Techn.*, vol. 68, no. 7, pp. 2768–2778, 2020 (cit. on pp. 27, 30, 31).

[92] A. Dürr, B. Schneele, D. Schwarz, and C. Waldschmidt, "Range-Angle Coupling and Near-Field Effects of Very Large Arrays in mm-Wave Imaging Radars," *IEEE Trans. Microw. Theory Techn.*, vol. 69, no. 1, pp. 262–270, 2021 (cit. on p. 27).

[93] Z. Geng, "Evolution of Netted Radar Systems," *IEEE Access*, vol. 8, pp. 124 961–124 977, 2020 (cit. on p. 28).

[94] M. Steiner, T. Grebner, and C. Waldschmidt, "Millimeter-Wave SAR-Imaging With Radar Networks Based on Radar Self-Localization," *IEEE Trans. Microw. Theory Techn.*, vol. 68, no. 11, pp. 4652–4661, November 2020 (cit. on p. 28).

[95] N. Kern, L. Paulus, T. Grebner, V. Janoudi, and C. Waldschmidt, "Radar-Based Gesture Recognition Under Ego-Motion for Automotive Applications," *IEEE Trans. Radar Syst.*, vol. 1, pp. 542–552, 2023 (cit. on p. 28).

[96] B. Nuss, Y. L. Sit, and T. Zwick, "3D Radar Image Fusion using OFDM-based MIMO Radar," in *German Microw. Conf. (GeMiC)*, March 2016, pp. 209–212 (cit. on p. 28).

[97] A. Demir, A. Mehrotra, and J. Roychowdhury, "Phase Noise in Oscillators: A Unifying Theory and Numerical Methods for Characterisation," in *Proc. 35th annu. Design Automat. Conf.*, New York, NY, USA: Association for Computing Machinery, May 1998, pp. 26–31 (cit. on p. 29).

[98] B. Meinecke, M. Steiner, J. Schlichenmaier, J. Hasch, and C. Waldschmidt, "Coherent Multistatic MIMO Radar Networks Based on Repeater Tags," *IEEE Trans. Microw. Theory Techn.*, vol. 67, no. 9, pp. 3908–3916, 2019 (cit. on pp. 30, 31, 61).

[99] M. Ash, M. Ritchie, K. Chetty, and P. V. Brennan, "A New Multistatic FMCW Radar Architecture by Over-the-Air Deramping," *IEEE Sensors J.*, vol. 15, no. 12, pp. 7045–7053, 2015 (cit. on pp. 30, 31).

[100] A. Frischen, G. Hakobyan, and C. Waldschmidt, "Coherent Measurements With MIMO Radar Networks of Incoherent FMCW Sensor Nodes," *IEEE Microw. Wireless Compon. Lett.*, vol. 30, no. 7, pp. 721–724, 2020 (cit. on pp. 30, 31).

[101] M. Gottinger, F. Kirsch, P. Gulden, and M. Vossiek, "Coherent Full-Duplex Double-Sided Two-Way Ranging and Velocity Measurement Between Separate Incoherent Radio Units," *IEEE Trans. Microw. Theory Techn.*, vol. 67, no. 5, pp. 2045–2061, 2019 (cit. on p. 31).

[102] P. Fenske, T. Koegel, R. Ghasemi, and M. Vossiek, "Constellation Estimation, Coherent Signal Processing, and Multiperspective Imaging in an Uncoupled Bistatic Cooperative Radar Network," *IEEE J. Microw.*, pp. 1–15, 2024 (cit. on p. 31).

[103] "IEEE Standard for Information Technology - Telecommunications and information exchange between systems - Local and Metropolitan Area networks - Specific requirements - Part 11: Wireless LAN Medium Access Control (MAC) and Physical Layer (PHY) specifications," *ANSI/IEEE Std 802.11, 1999 Ed. (R2003)*, pp. 1–512, November 1998 (cit. on p. 33).

[104] "IEEE Standard for Low-Rate Wireless Networks," *IEEE Std 802.15.4-2015 (Revision of IEEE Std 802.15.4-2011)*, pp. 1–709, April 2016 (cit. on p. 33).

[105] J. P. Costas, "Synchronous Communications," *Proc. of the IRE*, vol. 44, no. 12, pp. 1713–1718, December 1956 (cit. on p. 33).

[106] F. M. Gardner, *Phaselock Techniques*, 2nd Ed. Wiley, 2005 (cit. on pp. 33, 47).

[107] J. Layland, "An Optimum Squaring Loop Prefilter," *IEEE Trans. Communication Technol.*, vol. 18, no. 5, pp. 695–697, October 1970 (cit. on pp. 33, 46).

[108] M. Bauduin and A. Bourdoux, "Impact of Phase Noise on FMCW and PMCW Radars," in *IEEE Radar Conf.*, May 2023, pp. 1–6 (cit. on p. 38).

[109] L. Smaini, *RF Analog Impairments Modeling for Communication Systems Simulation: Application to OFDM-based Transceivers*. Wiley, 2012 (cit. on p. 41).

[110] M. Oerder and H. Meyr, "Digital Filter and Square Timing Recovery," *IEEE Trans. Commun.*, vol. 36, no. 5, pp. 605–612, May 1988 (cit. on p. 44).

[111] T. Hentschel and G. Fettweis, "Continuous-Time Digital Filters for Sample-Rate Conversion in Reconfigurable Radio Terminals," *Frequenz*, vol. 55, no. 5-6, pp. 185–188, May 2001 (cit. on p. 44).

[112] P. Schoeder, A. Martin, B. Meinecke, D. Werbunat, and C. Waldschmidt, "A Modulation-Based Radar Target Simulator and Its Hardware Non-idealities," in *19th Europ. Radar Conf.*, Sep. 2022, pp. 1–4 (cit. on p. 63).

[113] B. Meinecke, M. Steiner, J. Schlichenmaier, and C. Waldschmidt, "Instantaneous Target Velocity Estimation Using a Network of a Radar and Repeater Elements," in *16th Eur. Radar Conf. (EuRAD)*, October 2019, pp. 241–244 (cit. on p. 64).

[114] B. Meinecke, D. Werbunat, P. Schoeder, and C. Waldschmidt, "Matching Bistatic Target Responses in Radar Networks to Enable Vectorial Velocity Estimation," in *18th Europ. Radar Conf.*, April 2022, pp. 42–45 (cit. on pp. 64, 70).

[115] D. Werbunat, B. Schweizer, B. Meinecke, R. Michev, J. Hasch, and C. Waldschmidt, "Ghost-Target Suppression in Coherent Radar Networks," in *18th Europ. Radar Conf.*, April 2022, pp. 54–57 (cit. on pp. 70, 71, 135, 136, 138).

[116] Z. Lin and Z. Wang, "Interleaved OFDM Signals for MIMO Radar," *IEEE Sensors J.*, vol. 15, no. 11, pp. 6294–6305, 2015 (cit. on p. 72).

[117] M. A. Hadi, S. Alshebeili, K. Jamil, and F. E. Abd El-Samie, "Compressive sensing applied to radar systems: An overview," *Signal, Image and Video Process.*, vol. 9, no. 1, pp. 25–39, 2015 (cit. on p. 74).

[118] F. Roos, J. Bechter, C. Knill, B. Schweizer, and C. Waldschmidt, "Radar Sensors for Autonomous Driving: Modulation Schemes and Interference Mitigation," *IEEE Microw. Mag.*, vol. 20, no. 9, pp. 58–72, Sep. 2019 (cit. on p. 74).

[119] A. Maleki, L. Anitori, Z. Yang, and R. G. Baraniuk, "Asymptotic Analysis of Complex LASSO via Complex Approximate Message Passing (CAMP)," *IEEE Trans. Inf. Theory*, vol. 59, no. 7, pp. 4290–4308, 2013 (cit. on pp. 74, 75).

[120] C. Knill, "Novel MIMO OFDM Waveform Designs and High-Performance Signal Processing Methods for Digital Radars," en, April 2022 (cit. on pp. 74, 75).

[121] D. Werbunat, B. Meinecke, M. Steiner, and C. Waldschmidt, "Phase Recovery in Sensor Networks Based on Incoherent Repeater Elements," in *IEEE/MTT-S Int. Microw. Symp.*, ISSN: 2576-7216, August 2020, pp. 1149–1152 (cit. on pp. 76–79).

[122] B. Meinecke, D. Werbunat, Q. Haidari, M. Linder, and C. Waldschmidt, "Near-Field Compensation for Coherent Radar Networks," *IEEE Microw. Wireless Compon. Lett.*, vol. 32, no. 10, pp. 1251–1254, 2022 (cit. on pp. 81, 125).

[123] F. Marvasti, A. Amini, F. Haddadi, *et al.*, "A unified approach to sparse signal processing," *EURASIP J. Advances Signal Process.*, vol. 2012, no. 1, p. 44, 2012 (cit. on pp. 82, 101).

[124] S. Klimenko, "Entwurf und Bewertung vertikaler MMIC-zu-Hohlleiterübergänge im E-Band," Bachelor's Thesis, Universität Ulm, 2021 (cit. on p. 92).

[125] J. P. Lee and M. B. Comisarow, "The Phase Dependence of Magnitude Spectra," *J. Magn. Reson.*, vol. 72, pp. 139–142, January 1987 (cit. on p. 105).

[126] M. S. Dadash, J. Hasch, P. Chevalier, A. Cathelin, N. Cahoon, and S. P. Voinigescu, "Design of Low-Power Active Tags for Operation With 77-81-GHz FMCW Radar," *IEEE Trans. Microw. Theory Techn.*, vol. 65, no. 12, pp. 5377–5388, 2017 (cit. on p. 107).

[127] R. Michev, R. N. Sridhar, J. Hasch, and C. Waldschmidt, "Enhancing the Dynamic Range of OFDM Radars Using Non-Linear Operation and Symbol-Based Equalization," *IEEE J. Microw.*, vol. 3, no. 2, pp. 614–624, April 2023 (cit. on p. 110).

[128] M. Bauduin and A. Bourdoux, "Code Diversity for Range Sidelobe Attenuation in PMCW and OFDM Radars," in *IEEE Radar Conf.*, ISSN: 2375-5318, May 2021, pp. 1–5 (cit. on pp. 110, 115).

Index of own Publications

Parts of this thesis have already been published in the following publications.

Articles in Peer-Reviewed Scientific Journals

[1] D. Werbunat, B. Meinecke, B. Schweizer, J. Hasch, and C. Waldschmidt, "OFDM-Based Radar Network Providing Phase Coherent DOA Estimation," *IEEE Trans. Microw. Theory Techn.*, vol. 69, no. 1, pp. 325–336, January 2021.

[2] B. Schweizer, C. Knill, D. Werbunat, S. Stephany, and C. Waldschmidt, "Mutual Interference of Automotive OFDM Radars—Analysis and Countermeasures," *IEEE J. Microw.*, vol. 1, no. 4, pp. 950–961, October 2021.

[3] P. Schoeder, V. Janoudi, B. Meinecke, D. Werbunat, and C. Waldschmidt, "Flexible Direction-of-Arrival Simulation for Automotive Radar Target Simulators," *IEEE J. Microw.*, vol. 1, no. 4, pp. 930–940, October 2021.

[4] B. Meinecke, D. Werbunat, Q. Haidari, M. Linder, and C. Waldschmidt, "Near-Field Compensation for Coherent Radar Networks," *IEEE Microw. Wireless Compon. Lett.*, vol. 32, no. 10, pp. 1251–1254, 2022.

[5] L. L. Tovar Torres, T. Grebner, D. Werbunat, and C. Waldschmidt, "Automotive Radar Interference Mitigation by Subtraction of the Interference Component," *IEEE Microw. Wireless Technol. Lett.*, vol. 33, no. 9, pp. 1397–1400, Sep. 2023.

[6] R. Michev, Y. Shu, D. Werbunat, J. Hasch, and C. Waldschmidt, "Adaptive Compensation of Hardware Impairments in Digitally Modulated Radars Using ML-Based Behavioral Models," *IEEE Trans. Microw. Theory Techn.*, pp. 1–14, 2023.

[7] D. Werbunat, B. Woischneck, J. Lerch, *et al.*, "Multichannel Repeater for Coherent Radar Networks Enabling High-Resolution Radar Imaging," *IEEE Trans. Microw. Theory Techn.*, pp. 1–13, 2023.

[8] D. Werbunat, J. Aguilar, M. Almarashly, *et al.*, "On the Synchronization of Uncoupled Multistatic PMCW Radars," *IEEE Trans. Microw. Theory Techn.*, 2024.

[9] J. Aguilar, D. Werbunat, V. Janoudi, C. Bonfert, and C. Waldschmidt, "Uncoupled Digital Radars Creating a Coherent Sensor Network," *IEEE J. Microw.*, pp. 1–14, 2024.

Articles in Conference Proceedings with Peer-Review Process

[1] D. Werbunat, B. Meinecke, M. Steiner, and C. Waldschmidt, "Phase Recovery in Sensor Networks Based on Incoherent Repeater Elements," in *IEEE/MTT-S Int. Microw. Symp.*, ISSN: 2576-7216, August 2020, pp. 1149–1152.

[2] C. Knill, B. Schweizer, S. Stephany, D. Werbunat, and C. Waldschmidt, "FMCW-Interference of Frequency Agile OFDM Radars," in *17th Europ. Radar Conf.*, 2021, pp. 160–163.

[3] D. Werbunat, F. Sgroi, C. Knill, *et al.*, "Multiplexing of OFDM-Based Radar Networks," in *IEEE Radar Conf.*, IEEE, 2021, pp. 1–6.

[4] D. Werbunat, B. Schweizer, B. Meinecke, R. Michev, J. Hasch, and C. Waldschmidt, "Ghost-Target Suppression in Coherent Radar Networks," in *18th Europ. Radar Conf.*, April 2022, pp. 54–57.

[5] B. Meinecke, D. Werbunat, P. Schoeder, and C. Waldschmidt, "Matching Bistatic Target Responses in Radar Networks to Enable Vectorial Velocity Estimation," in *18th Europ. Radar Conf.*, April 2022, pp. 42–45.

[6] R. Michev, D. Werbunat, J. Hasch, and C. Waldschmidt, "IQ-Transmitter Digital Predistortion for an OFDM Radar," in *18th Europ. Radar Conf.*, April 2022, pp. 325–328.

[7] P. Schoeder, A. Martin, B. Meinecke, D. Werbunat, and C. Waldschmidt, "A Modulation-Based Radar Target Simulator and Its Hardware Nonidealities," in *19th Europ. Radar Conf.*, Sep. 2022, pp. 1–4.

[8] D. Werbunat, B. Schweizer, M. Maier, *et al.*, "An All-Digital Carrier Synthesis for Stepped OFDM Radars," in *IEEE/MTT-S Int. Microw. Symp.*, ISSN: 2576-7216, Jun. 2023, pp. 220–223.

[9] T. Köhler, D. Werbunat, A. Di Serio, D. Schwarz, and C. Waldschmidt, "2D-Array Optimization for Coherent Radar Networks," *21st Europ. Radar Conf.*, 2024.

[10] R. Michev, J. Hasch, C. Naber, D. Werbunat, N. Hepp, and C. Waldschmidt, "A Compact 77 GHz 4x4 MIMO Stepped Frequency OFDM Radar Demonstrator," *21st Europ. Radar Conf.*, 2024.

The two lead authors of [8] and of [9], respectively, have contributed equally.

Awards

VDE ITG-Preis 2021

[1] D. Werbunat, B. Meinecke, B. Schweizer, J. Hasch, and C. Waldschmidt, "OFDM-Based Radar Network Providing Phase Coherent DOA Estimation," *IEEE Trans. Microw. Theory Techn.*, vol. 69, no. 1, pp. 325–336, January 2021.

EuRAD Young Engineer Prize, 2022

[1] P. Schoeder, A. Martin, B. Meinecke, D. Werbunat, and C. Waldschmidt, "A Modulation-Based Radar Target Simulator and Its Hardware Nonidealities," in *19th Europ. Radar Conf.*, Sep. 2022, pp. 1–4.

IMS Advanced Practice Paper Award, 2023

[1] D. Werbunat, B. Schweizer, M. Maier, *et al.*, "An All-Digital Carrier Synthesis for Stepped OFDM Radars," in *IEEE/MTT-S Int. Microw. Symp.*, ISSN: 2576-7216, Jun. 2023, pp. 220–223.

EuRAD Conference Prize, 2024

[1] R. Michev, J. Hasch, C. Naber, D. Werbunat, N. Hepp, and C. Waldschmidt, "A Compact 77 GHz 4x4 MIMO Stepped Frequency OFDM Radar Demonstrator," *21st Europ. Radar Conf.*, 2024.

Herausgeber:
Prof. Dr.-Ing. Christian Waldschmidt

universität ulm

ISBN: 978-3-948303-52-5 ISBN: 978-3-948303-53-2 (E-Book)